PEDESTAL-FREE PULSE COMPRESSION IN NONLINEAR FIBERS AND NONLINEAR FIBER BRAGG GRATINGS

LI QIAN

Ph. D

The Hong Kong Polytechnic University

2009

The Hong Kong Polytechnic University

Department of Electronic and Information Engineering

PEDESTAL-FREE PULSE COMPRESSION IN NONLINEAR FIBERS AND NONLINEAR FIBER BRAGG GRATINGS

LI QIAN

Advisor: Prof. Ping-kong Alexander Wai

A thesis submitted in partial fulfillment of the requirements

for

The Degree of Doctor of Philosophy

June 2008

Certificate of Originality

I hereby declare that this thesis is my own work and that, to the best of my knowledge and belief, it reproduces no material previously published or written nor material which has been accepted for the award of any other degree or diploma, except where due acknowledgement has been made in the text.

───────────── (Signed)

───────────── (Name of student)

Dedication

To my supervisor, my parents and all my friends

Motto

"I hear and I forget, I see and I remember, I do and I understand."

Abstract

Recently, a technique known as self-similar analysis has been utilized to study linearly chirped pulses in optical fibers and fiber amplifiers. The self-similar pulses have attracted much attention since the linear chirp facilitates efficient pulse compression. In addition, these pulses can propagate without pulse break-up at high powers. However, because of the relatively small dispersion of optical fibers, this scheme requires long fiber lengths, and only a few dispersion profiles are practically feasible. A more attractive solution consists of pulse compression in a highly dispersive nonlinear medium such as a fiber Bragg grating (FBG). Grating dispersion just outside the stop band is up to six orders of magnitude larger than that of silica fiber and can be tailored simply by changing the grating profile. This potential suggests utilizing this huge dispersion to construct a short compressor.

Through the self-similar analysis, we have theoretically investigated the linearly chirped Bragg soliton near the photonic bandgap (PBG) structure of FBG. Efficient Bragg soliton compression can be achieved with the exponentially decreasing dispersion. The stepwise approximation of exponentially decreasing dispersion is carried out by concatenation of grating segments with constant dispersion. For the proposed compression scheme, the input pulse must be pre-chirped in a prescribed manner, and a simple pre-chirper, such as a linear fiber or grating, is used to add the required chirp profile to initial chirp-free hyperbolic secant or Gaussian pulse. The comparisons between nonlinear Schrödinger (NLS) equation, pulse parameter evolution equations, and nonlinear coupled-mode equations are given.

Higher order nonlinearities must be considered if the optical pulse intensity is

high or the nonlinear coefficients of the materials are large, for instance, in semiconductor doped glasses. Therefore, we have investigated the existence of chirped solitary wave solutions in the cubic-quintic nonlinear media with exponentially decreasing dispersion. We numerically show that competing cubic and quintic nonlinearities stabilize the chirped solitary wave propagation against perturbations of initial pulse parameters. In addition, we studied the possibility of rapid compression of Townes solitons by the collapse phenomenon in the exponentially decreasing dispersion. We also found that the collapse could be postponed if the dispersion increases exponentially.

Awards and Grants Arising from the Thesis

Publications Arising from the Thesis

Journals:

1. K. Senthilnathan, **Qian Li**, K. Nakkeeran, and P. K. A. Wai, "Robust pedestal-free pulse compression in cubic-quintic nonlinear media," *Phys. Rev. A* **78,** 033835 (2008) --- selected for the October 2008 issue of Virtual Journal of Ultrafast Science.

2. **Qian Li**, K. Senthilnathan, K. Nakkeeran, and P. K. A. Wai, "Nearly chirp- and pedestal-free pulse compression in nonlinear fiber Bragg gratings," *J. Opt. Soc. Am. B* **26**, 432-443 (2009).

3. **Qian Li**, P. K. A. Wai, K. Senthilnathan, and K. Nakkeeran, "Pedestal free pulse compression in non-uniform Fiber Bragg gratings," in preparation.

4. K. Senthilnathan, **Qian Li**, K. Nakkeeran, and P. K. A. Wai, "Chirped higher order solitons," in preparation.

Book Chapter:

K. Senthilnathan, K. Nakkeeran, K. W. Chow, **Qian Li**, and P. K. A. Wai, "Chirped optical solitons," in Advances in Nonlinear Waves and Symbolic Computation (Nova, 2009).

Conference papers:

1. K. Senthilnathan, **Qian Li**, P. K. A. Wai, and K. Nakkeeran, "Chirped self-similar pulse propagation in cubic-quintic media," in *Proc. of the Progress in Electromagnetic Research Symposium(PIERS)*, Beijing, China, 26-30 Mar. 2007, Paper 3, 531.

2. **Qian Li**, P. K. A. Wai, K. Nakkeeran, and K. Senthilnathan, "Nearly chirp-free and pedestal-free pulse compression", in *Proc. of OptoElectronics and Communications Conference(OECC)*, Yokohama, Japan, 9-13 Jul. 2007,

Paper 13P-21.

3. K. Senthilnathan, **Qian Li**, P. K. A. Wai, and K. Nakkeeran*, *"Bragg soliton pulse compression in non-uniform fiber Bragg gratings", in *Proc. of OptoElectronics and Communications Conference(OECC)***, Yokohama, Japan, 9-13 Jul. 2007, Paper 13C1-4.

4. **Qian Li**, K. Senthilnathan, K. Nakkeeran, and P. K. A. Wai, "Pedestal-free pulse compression in nonlinear fiber Bragg gratings with exponentially varying dispersion," in *Proc. of OptoElectronics and Communications Conference(OECC)*, Sydney, Australia, 7-10 Jul. 2008, Paper P18.

5. K. Senthilnathan, K. Nakkeeran, **Qian Li**, and P. K. A. Wai, "Chirped Optical Solitons: High Degree Pulse Compression," in *Proc. of OptoElectronics and Communications Conference(OECC)*, Hong Kong, 13-17 Jul. 2009, Paper FG2.

6. **Qian Li**, K. Senthilnathan, K. Nakkeeran, and P. K. A. Wai, "Effects of higher order dispersion on self-similar pulse compression in nonlinear fiber Bragg gratings," in *Proc. Pacific Rim Conference Lasers and Electro-Optics (CLEO®/Pacific Rim 2009)*, Shanghai, China, 30 Aug.-3 Sep. 2009, paper ThB1-3.

7. Feng Li, **Qian Li**, Xinhuan Feng, and P. K. A. Wai, "Noinear dynamics in lasers with nonlinear loss," in *Proc. Pacific Rim Conference Lasers and Electro-Optics (CLEO®/Pacific Rim 2009)*, Shanghai, China, 30 Aug. -3 Sep. 2009, paper TuD3-4.

Acknowledgments

First of all, I want to thank my supervisor Prof. Ping-kong Alexander Wai for his scientific guidance and continuous support over all the duration of my studies.

Special thanks go to Dr. K. Senthilnathan, Dr. Y. H. Canny Kwan, Dr. K. Nakkeeran, Dr. Feng Li, Dr. C. Y. Li, and Prof. Chao Lu. I'm mostly grateful for the many fruitful discussions which allowed me to gain a deep understanding and a broader view of the topics involved in this research.

Also thanks to all the members of Photonics Research Centre and the staff of the Department of Electronic and Information Engineering.

I would like to express my gratitude to my parents in China. They are always at the other end of the phone, ready to help, to suggest, to push and fortunately to criticize me.

A PhD does not end within offices and laboratories. It is a life experience, and it has been the most significant one in my life so far.

Statement of Originality

The following contributions reported in this thesis are claimed to be original.

1 I demonstrate the existence of self-similar soliton in FBGs with exponentially decreasing dispersion.

2 I demonstrate the physical mechanisms that determine the evolution of self-similar soliton as the grating and pulse parameters vary.

3 I demonstrate the stepwise approximation of the dispersion exponentially decreasing FBG, and the number of segments is associated with the compression factor and initial chirp value.

4 I suggest the use of linear grating or fiber to get the required chirp for the initial pulse.

5 I determine the chirped solitary wave solutions in the anomalous and normal dispersion regimes of the cubic-quintic nonlinear media.

6 I numerically demonstrate the competing cubic and quintic nonlinearities stabilize the chirped soliton pulse propagation against the perturbations in the initial soliton pulse parameters.

Contents

Chapter 1

Introduction

Optical phenomena have been attracting increasing attention in view of their potential capability to handle a large volume of information, for acquisition, transmission, processing, storage and display of data [1]. The explosive developments which have been taking place in information technology would not be possible without optics. The naming of "photonics", is similar to the naming of "electronics". However, "photonics" straddles the border between optics and electronics to provide technology and infrastructure for global Internet and for mobile communications.

There is a general trend in modern society to generate and consume as much information as possible. Having more information, one has better chance to create new activities, which in turn demands more information. This positive feedback mechanism may be an underlying driver of information society. The high bit-rate transmission systems for the intercontinental submarine network reached nearly 1 Tbit/s throughput [1]. Also new services for Internet and users create a strong demand for a high bit-rate metropolitan network supporting more than 100 Gbit/s throughput [1].

Consequently, among the variety of optical phenomena, the generation and

1

control of ultrashort optical pulses have attracted much attention. Besides the need of ultrashort pulse in telecommunication applications, ultrashort optical pulses are valuable tools when experimentalists require femtosecond and picosecond time resolution, high peak powers, or large optical bandwidths [2]. As a result, short pulse optical sources are becoming a key technology. Because of the high time resolution (femtosecond), short pulse has been used in ultrafast spectroscopy, physical and biological processes, femto-chemistry, high speed electric circuit testing and sampling of electrical signals. Because of the high spatial resolution (sub-micrometer), short pulse has been used in optical imaging, e.g. optical coherence tomography. Because of the high bandwidth (terahertz), short pulse has been used in communications. Because of the high intensity (terawatt to petawatt), short pulse has been used in nonlinear frequency conversion, laser material processing, surgery and high intensity physics.

1.1   Pulse Compression Techniques

Short pulses can be generated from many laser sources directly. Picosecond laser pulses were first produced in a passively mode-locked ruby laser [3] and a Nd: glass laser [4], respectively. However, pulses emitted from practical laser sources are often chirped. As an alternative, we can use pulse compression to reduce the pulse duration. There is variety of methods for temporally compressing optical pulses, i.e. to reduce the pulse duration. These methods can be grouped into two categories: linear pulse compression and nonlinear pulse compression.

1.1.1   Linear Pulse Compression

In linear pulse compression, the duration of chirped pulse can be reduced by removing (or at least reducing) the chirp, i.e. by flattening the spectral phase. De-chirping can be accomplished by sending the pulse through an optical element

with a suitable amount of chromatic dispersion for the purpose of dispersion compensation, e.g. a grating compressor, a prism pair, an optical fiber, or a chirped mirror. The smallest possible pulse duration is then set by the optical bandwidth of the pulses, which is not modified by linear compression. In the ideal case, transform-limited pulses are obtained.

To see how such dispersion compensation can produce shorter pulses, we consider the propagation of chirped Gaussian pulse inside an optical fiber. In the case of chirped Gaussian pulses, the incident field can be written as

$$E(0,t) = \exp\left(-\frac{1+iC}{2}\frac{t^2}{T_0^2}\right),$$

(1.1)

where C is the chirp parameter, T_0 is the half-width (at 1/e intensity point) of input pulse. $E(z,t)$ satisfies the following linear partial differential equation:

$$i\frac{\partial E}{\partial z} = \frac{\beta_2}{2}\frac{\partial^2 E}{\partial t^2},$$

(1.2)

where z is the distance, t is the time, and β_2 is the group velocity dispersion (GVD) coefficient.

Then we have

$$E(z,t) = \frac{T_0}{\sqrt{T_0^2 - i\beta_2 z + C\beta_2 z}}\exp\left[-\frac{(1+iC)t^2}{2(T_0^2 - i\beta_2 z + C\beta_2 z)}\right],$$

(1.3)

Eq. (1.3) can be used to find the compression factor $F_C = T_0/T_p$ as a function of propagation distance, where T_p is the pulse width parameter of the compressed Gaussian pulse. F_C can be given by

$$F_C(\xi) = \left\{\left[1 + \text{sgn}(\beta_2)C\xi\right]^2 + \xi^2\right\}^{-1/2}.$$

(1.4)

The propagation distance $\xi = z/L_D$ is normalized to dispersion length

$L_D = T_0^{\ 2}/|\beta_2|$ [5]. Eq. (1.4) shows that a pulse can be compressed only if

$\text{sgn}(\beta_2)C < 0$. This means that chirp cancellation occurs only if the initial chirp

and group velocity dispersion (GVD) induced chirp are opposite. Positively

chirped pulses ($C > 0$) require anomalous GVD for compression and vice versa

[6].

Eq. (1.4) also shows that the shortest pulse is obtained at a specific distance

given by $\xi = |C|/(1+C^2)$. The maximum compression factor at the distance is

fixed by the input chirp as $F_C = \sqrt{1+C^2}$. This limit is easily understood by noting

that spectrum of a chirped input pulse is broadened by a factor of $\sqrt{1+C^2}$

compared with that of an unchirped pulse [5]. In the time domain, the

compression process can be visualized as follows [6]. Different frequency

components of the pulse travel at different speeds in the presence of GVD. If the

leading edge of the pulse is delayed by just the right amount to arrive nearly with

the trailing edge, the output pulse is compressed. Positively chirped pulses

(frequency increasing toward the trailing side) require anomalous GVD in order

to slow down the red-shifted leading edge. By contrast, negatively chirped pulses

require normal GVD to slow down the blue-shifted leading edge.

Early pulse-compression studies made use of both normal and anomalous GVD,

depending on the technique through which frequency chirp was initially imposed

on the pulse [6]. In the case of negatively chirped pulses, pulses were transmitted

through liquids or gases such that they experienced normal GVD [7]. In the case

of positively chirped pulses, a grating pair was found to be most suitable for

providing anomalous GVD [8]. In these early experiments, pulse compression did

not make use of any nonlinear optical effects, although the use of the nonlinear

process of self-phase modulation (SPM) for pulse compression was suggested as early as 1969 [9]. The experimental work on SPM-based pulse compression took off only during the 1980s when the use of single-mode silica fibers as a nonlinear medium became widespread [6].

1.1.2 Nonlinear Pulse Compression

Nonlinear pulse compression relies on the interaction of Kerr nonlinearity and quadratic dispersion. These techniques are inherently nonlinear and can generate an increased bandwidth, which is an effect that purely linear devices are incapable of doing [2]. This important property, in turn, allows for the compression of transform-limited pulses into shorter transformation-limited pulses [2]. Pulse compressors based on nonlinear fiber optics can be classified into two broad categories: grating fiber compressors and soliton-effect compressors. Grating fiber compressors are useful for compressing pulses in the visible and near-infrared regions while soliton-effect compressors work typically in the range from 1.3 to 1.6 μm [6]. The wavelength region near 1.3 μm offers special opportunities since both kinds of compressors can be combined to yield large compression factors by using dispersion-shifted fibers [6].

Grating fiber compressor, first proposed by Tomlinson et al. [10], a fiber with positive dispersion, imposes a nearly linear, positive chirp on a pulse through the combined effect of SPM and positive GVD. SPM occurring in the optical fiber generates new frequencies in the pulse spectrum, and simultaneously the GVD linearizes the chirp and squares the pulse. The linear chirp on the pulse can be compensated by another dispersive element with negative GVD, such as a grating pair or a prism pair, producing a nearly transform limited compressed pulse. This technique has been applied successfully in Ref. [11]. A severe limitation on the

performance of grating fiber compressors for ultrashort pulses ($T_0 < 50$ fs) is imposed by the grating pair that no longer acts as a quadratic compressor. For such short pulses, the third order dispersion effect becomes comparable to the second order dispersion effect. An ultimate limitation on the performance of grating fiber compressors is imposed by stimulated Raman scattering [12−15]. Even though the compression factor can be in theory increased by increasing the peak power of the incident pulse, it is limited in practice since the peak power must be kept below the Raman threshold to avoid the transfer of pulse energy to the Raman pulse. Furthermore, even if some energy loss is acceptable, the Raman pulse can interact with the pump pulse through cross-phase modulation and deform the linear nature of the frequency chirp. It is still possible to achieve large compression even in the Raman regime, but a significant part of the pulse remains uncompressed because of mutual interaction between the pump and Raman pulses. For highly energetic pulses, parametric processes such as four-wave mixing can suppress the Raman process to some extent, but they eventually limit the extent of pulse compression [16].

Several pulse compression schemes based on soliton effect have been proposed. These schemes rely on the robust nature of optical solitons. Mollenauer et al. [17] reported the first experimental observation of higher-order soliton compressor, which consists simply of a single piece of fiber with negative dispersion, whose length is suitably chosen. A transform limited pulse with appropriate peak intensity, propagating in this fiber, is compressed through the interplay between SPM and GVD [17]. The compression is due to an initial narrowing phase that occurs during the evolution of a higher-order soliton, before the initial soliton shape is restored after one soliton period [18]. The degree of compression is quite

large but the compressed pulse is accompanied by a serious pedestal, leading to nonlinear interactions between neighboring solitons. Some techniques, such as residual pedestal nonlinear intensity discrimination technique [19, 20] can help to reduce the pedestals, but energy is wasted.

By varying the GVD along the direction of propagation in an optical fiber, Chernikov and Mamyshev have demonstrated the manipulation of a fundamental soliton resulting in adiabatic pulse compression [21]. Adiabatic pulse compressors typically use a dispersion profile with monotonically decreasing GVD along the propagation direction, and is formally equivalent to distributed amplification [21, 22]. If the dispersion varies slowly enough, the soliton self-adjusts to maintain balance between GVD and nonlinearity, reducing its pulse width—hence the term adiabatic compression [2]. This compression scheme is attractive because it inherently maintains the transform-limited characteristics of the pulse as it compresses, resulting in a clean pulse and avoiding any requirement for bulk optics [2]. However, adiabatic condition must be satisfied, i.e. change must be gradual. Such compression has been demonstrated experimentally by a variety of schemes to achieve the effect of decreasing dispersion [23].

As Moores pointed out in Ref. [24], exact chirped-soliton solutions to the NLS equation exist when we have distributed gain $g(z) = g_0 / (1 - g_0 z)$ or exponentially varying dispersion. One of the advantages of this compression scheme is that adiabatic condition does not need to be satisfied and rapid compression is possible. More recently, a technique known as self-similar analysis has been utilized to study linearly chirped pulses in optical fibers and fiber amplifiers [25−28]. The self-similar pulses have attracted much attention since the linear chirp facilitates efficient pulse compression. In addition, these

pulses can propagate without pulse break-up, called optical wave-breaking, even at high powers [29]. Krugolv et al. investigated the linearly chirped self-similar solitary waves in optical fiber amplifiers [26, 27]. Billet et al. generated the linearly chirped parabolic pulses experimentally and achieved efficient pulse compression by using a hollow-core photonic bandgap fiber [28]. Experimental demonstration of similariton pulse compression in a comblike dispersion-decreasing fiber amplifier has been shown in Ref. [30]. However, because of the relatively small GVD of optical fibers, this scheme requires long fiber lengths, and only a few dispersion profiles are practically feasible. Moreover, fabrication of fibers with complex dispersion profiles usually involves splicing of several different fibers or drawing the fiber with an axially varying core diameter.

1.2 Fiber Bragg Gratings as Pulse Compressor

A more attractive solution consists of pulse compression in a highly dispersive nonlinear medium such as a fiber Bragg grating (FBG). Grating dispersion just outside the stop band is up to six orders of magnitude larger than that of silica fiber and can be tailored simply by changing the grating profile. Almost any grating profile can be manufactured using the state-of-the-art grating-writing techniques. This potential suggests utilizing the large dispersion to construct a compact compressor.

We study the linearly chirped self-similar Bragg solitary pulses near the photonic bandgap (PBG) structure theoretically. Efficient pulse compression can be achieved with the appropriate grating induced dispersions.

1.2.1 Background

Silica fibers can change their optical properties permanently when exposed to intense radiation from a laser operating in the blue or ultraviolet spectral region.

This photosensitive effect can be used to induce periodic changes in the refractive index along the fiber length, resulting in the formation of an intracore Bragg grating [6]. The changes in the refractive index of the fiber at a wavelength λ may be calculated from the observed changes in the absorption spectrum in the ultraviolet using the Kramers-Kronig relationship [31, 32],

$$\Delta n(\lambda) = \frac{1}{(2\pi)^2} \Sigma \int_{\lambda_2}^{\lambda_1} \frac{\left(\Delta \alpha_i(\lambda') \cdot \lambda^2\right)}{\left(\lambda^2 - \lambda'^2\right)} d\lambda', \tag{1.5}$$

where the summation is over discrete wavelength intervals around each of the i changes in measured absorption, α_i.

Typically, index change Δn is $\sim 10^{-4}$ in the 1.3- to 1.6-µm wavelength range, but can exceed 0.001 in fibers with high Ge concentration [33, 34]. However, standard telecommunication fibers rarely have more than 3% of Ge atoms in their core, resulting in relatively small index changes. The use of other dopants such as phosphorus, boron, and aluminum can enhance the photosensitivy (and the amount of index change) to some extent, but these dopants also tend to increase fiber losses [6]. It was discovered in the early 1990s that the amount of index change induced by ultraviolet absorption can be enhanced by two orders of magnitude $(\Delta n > 0.01)$ by soaking the fiber in hydrogen gas at high pressures (200 atm) and room temperature [35].

A one-dimensional photonic crystal is considered, such as a Bragg grating, located in the core of a fiber, whose axis is in the z-direction. The linear refractive index is given by

$$n(z) = n_0 + \delta n(z) + \Delta n(z) \cos\left[\frac{2\pi}{\Lambda} z + \Phi(z)\right], \tag{1.6}$$

where n_0 is the refractive index of the fiber core, $\delta n(z)$ is the change in the

average refractive index, $\Delta n(z)$ is refractive index modulation depth, Λ is the grating period, and $\Phi(z)$ is the phase that allows for grating period variations. For typical gratings in optical fiber, $n_0 \sim 1.5$, both $\Delta n(z)$ and $\delta n(z)$ can be as large as 0.01 in H_2 loaded fibers [36], and the period is usually of the order of $\Lambda \sim 0.5\,\mu\mathrm{m}$ [36].

Uniform Bragg gratings are well understood. If the wavelength of the incident light is close to the resonant Bragg wavelength of the periodic grating structure then light will be strongly reflected. For a grating with a period Λ, the Bragg wavelength is $\lambda_B = 2\bar{n}\Lambda$, where $\bar{n} = n_0 + \delta n$. The width $\Delta\lambda$ of the band of wavelengths that are strongly reflected by the grating, referred to as the photonic bandgap, is

$$\frac{\Delta\lambda}{\lambda_B} \cong \frac{\Delta n}{\bar{n}}. \tag{1.7}$$

If the wavelength of the incident light lies within the PBG, the field envelopes in the grating are evanescent and light is mostly reflected, while outside the PBG, the fields are propagating waves and light is mostly transmitted.

In the grating with a uniform index modulation, spectral side lobes are present in the transmission spectrum for wavelengths outside the photonic band gap (i.e. in the passband). These side lobes are accompanied by distortion, in the form of ripple in the GVD of the grating [37]. They result from a mismatch in the effective index of the grating and the surrounding medium (i.e. bare fiber), and can be removed by allowing the index modulation to vanish smoothly at each end, a process known as apodization [38]. This technique is widely exploited in designing photonic components for wavelength division multiplexing applications

in which the out-of-band reflections are highly undesirable [39, 40]. Apodization is critical in the design and implementation of fiber grating-based pulse compressors.

Apodized gratings are just one example of nonuniform Bragg gratings in which one or more of the quantities, $\delta n(z)$, $\Delta n(z)$ and $\Phi(z)$ are slowly varying functions along the length of the grating. Figure 1.1 shows three examples of nonuniform gratings: Figure 1.1(a) represents a uniform grating with constant index modulation; Fig 1.1(b) represents a linearly tapered fiber grating with an index modulation that varies linearly along the length of the grating (constant average refractive index); and Fig 1.1(c) represents an apodized grating with the index modulation vanishing smoothly at each of the grating (constant average refractive index). Each point on the horizontal axis of the diagram corresponds to a particular point along the grating with a specific detuning. The shaded region corresponds to those frequencies that are strongly reflected, whereas the frequencies in the clear region are transmitted.

Gratings are often fabricated in photosensitive fiber using the phase mask scanning technique [39, 41, 42], in which an ultraviolet beam (with a wavelength of typically 242-248 nm) is scanned along the length of the phase mask. Gratings as long as 1 meter have been fabricated using this method [43]. Fabrication of apodized gratings, in which the grating amplitude varies along the length of grating, involves a two-step procedure [39]. First, an ultraviolet beam is varied as the beam is scanned along the length of phase mask. The intensity of the ultraviolet beam is varied as the beam is scanned along the axis of the fiber creating the modulated component of the grating. Second, the un-modulated component of the grating is then imprinted in the same manner without the phase
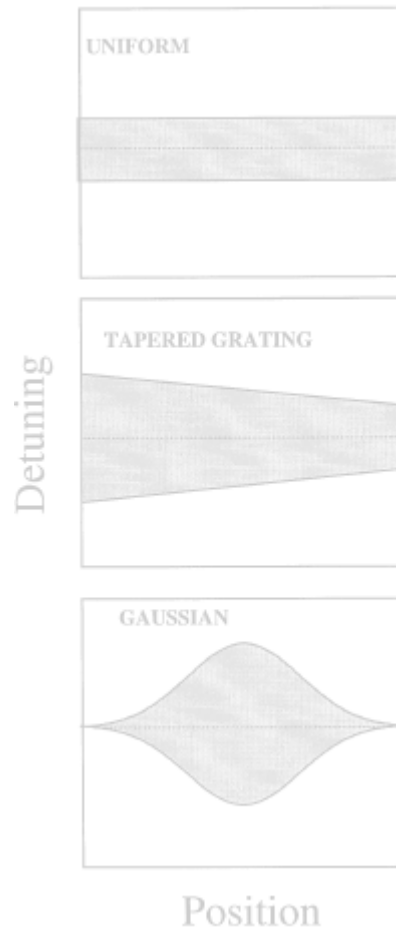
Figure 1.1: Schematic reflection band diagrams illustrating light propagation through Bragg gratings: (a) uniform Bragg gratings with constant index modulation, (b) linearly tapered fiber Bragg gratings with an index modulation that varies linearly along the length of the grating (constant average refractive index), and (c) apodized fiber Bragg gratings with the index modulation vanishing smoothly at each of the grating (constant average refractive index). The horizontal axis is positioned along the length of the grating and the vertical axis is detuning. The shaded region corresponds to those frequencies that are strongly reflected, whereas the frequencies in the clear region are transmitted. (After Ref. [2], © 2000 Taylor & Francis)

mask present. This two-step technique ensures that the average refractive index of the grating remains approximately constant along the length of the grating even though its strength changes, minimizing side lobes [2].

The frequency-domain coupled-mode equations are [6]

$$\frac{\partial \tilde{u}}{\partial z} = i\delta \tilde{u} + i\kappa \tilde{v},$$
$$-\frac{\partial \tilde{v}}{\partial z} = i\delta \tilde{v} + i\kappa \tilde{u},$$

(1.8)

where $\tilde{u}/\tilde{v}$ is the fourier transform of the forward/backward propagating wave, z is the distance, t is the time, δ is the frequency detuning, and κ is the coupling coefficient. One needs to consider the dispersion relation $\omega(k)$, which is also the relationship between the frequency detuning parameter $\delta = \beta_1(\omega - \omega_B)$ with β_1 is the group delay per unit length, and the propagation constant $\beta = k - k_B$, where ω and k are the optical frequency and the propagation wavenumber, respectively. A general solution of Eq. (1.8) takes the form

$$\tilde{u}(z) = A_1 \exp(i\beta z) + A_2 \exp(-i\beta z),$$
$$\tilde{v}(z) = B_1 \exp(i\beta z) + B_2 \exp(-i\beta z),$$

(1.9)

where β is to be determined. The constants A_1, A_2, B_1, and B_2 are interdependent and satisfy the following four relations:

$$(\beta - \delta) A_1 = \kappa B_1, \qquad (\beta + \delta) B_1 = -\kappa A_1,$$
$$(\beta - \delta) B_2 = \kappa A_2, \qquad (\beta + \delta) A_2 = -\kappa B_2.$$

(1.10)

These equations are satisfied for nonzero values of A_1, A_2, B_1, and B_2 if the possible values of β obey the dispersion relation

$$\beta = \pm\sqrt{\delta^2 - \kappa^2},$$

(1.11)

which is illustrated in Fig. 1.2, for both a uniform medium (dashed curve) and a

13

periodic medium (solid curve). Figure 1.2 shows that for frequencies in the range $-\kappa \leq \delta \leq \kappa$, defining the PBG, no propagating solutions are allowed; this corresponds to the regions of high reflectivity. Light can propagate outside the region, which corresponds to the passband.

The effective propagation constant of the forward- and backward-propagating waves is $\beta_e = \beta_B \pm \beta$. The frequency dependence of β_e indicates that a grating will exhibit dispersive effects even if it was fabricated in a nondispersive medium [6]. In optical fibers, grating induced dispersion adds to the material and waveguide dispersion, and the contribution of grating dominates among all sources responsible for dispersion. We expand β_e in a Taylor series around the carrier frequency ω_0 [6]:

$$\beta_e(\omega) = \beta_0 + (\omega - \omega_0)\beta_1 + \frac{1}{2}(\omega - \omega_0)^2 \beta_2 + \frac{1}{6}(\omega - \omega_0)^3 \beta_3 + ..., \qquad (1.12)$$

where β_m with $m = 1, 2, ...$ is defined as

$$\beta_m = \frac{\partial^m \beta}{\partial \omega^m}\bigg|_{\omega = \omega_0} \approx \left(\frac{1}{v_g}\right)^m \frac{d^m \beta}{d\delta^m}\bigg|_{\omega = \omega_0}. \qquad (1.13)$$

The group velocity of the pulse inside the grating is

$$V_G = 1/\beta_1 = \pm v_g \sqrt{1 - \kappa^2/\delta^2}, \qquad (1.14)$$

where the choice of $\pm$ signs depends on whether the pulse is moving forward or backward.

Second- and third-order dispersive properties of the grating are

$$\beta_2 = \frac{-\text{sgn}(\delta)\kappa^2 \beta_1^2}{(\delta^2 - \kappa^2)^{3/2}}, \quad \beta_3 = \frac{3|\delta|\kappa^2 \beta_1^3}{(\delta^2 - \kappa^2)^{5/2}}. \qquad (1.15)$$

In the absence of the grating, light ropagates at the speed of light in the medium. In the presence of the grating, the group velocity vanishes at the band edge and

asymptotically approaches the speed of light in the medium far from the Bragg resonance. The reduction in the group velocity can be explained in terms of the multiple Fresnel reflections that occur at each of the individual grating rulings, resulting in additional path length [2]. The extreme variation in the group velocity over such a relatively small range of wavelengths (roughly equal to the bandwidth of the grating) leads to strong GVD [2].
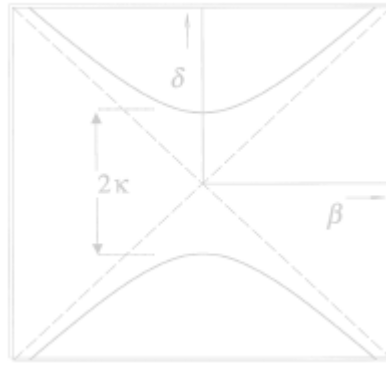
Figure 1.2: Dispersion relation of a uniform Bragg grating. The vertical axis is the detuning parameter and the horizontal axis is the propagation constants. (After Ref. [2], © 2000 Taylor & Francis)

On the long-wavelength side of the band gap ($\delta < -\kappa$), the grating GVD is positive, and can be used to compensate for the negative dispersion effects which are caused by propagation in optical fiber at communication wavelength. [44]. On the short-wavelength side of the photonic band gap ($\delta > \kappa$), the grating GVD is negative and solitons are supported [45, 46].

1.2.2 Dispersion of Fiber Bragg Gratings

It is well known that Bragg gratings can exhibit strong dispersion when they are used in reflection [36, 37]. Typically, in such experiments the Bragg grating is linearly chirped, so different frequencies reflect at different positions in the grating. Because the grating acts essentially as a mirror that is located at a frequency-dependent positions in the grating, strong dispersion results, which is

roughly six orders of magnitude larger than that of bare fiber. Indeed, in reflection, chirped fiber gratings have been shown to be able to compensate for the chromatic dispersion in long fiber links [47, 48].

In 1991 Russell [49] pointed out that gratings also exhibit strong dispersion in transmission for frequencies close to the Bragg resonance. This dispersion, which does not rely on any chirp or other grating nonuniformity, is due to the strong frequency dependence of group velocity of light propagating through a grating. The strong dispersion happens close to the Bragg resonance, but not so close so as to be inside the PBG where the reflectivity is high. The resulting dispersion was recently used for the compensation of dispersion in a 72-km fiber link, leading to error-free transmission of a 10-Gbit signal [44].

The first experimental observation of nonlinear propagation effects in FBGs, resulting in nonlinear optical pulse compression and soliton propagation, is reported in Ref. [45]. These solitons occur at frequencies near the PBG structure of the grating, and propagate at velocities well below the speed of light in the uniform medium. Adiabatic soliton compression in nonuniform grating structures has been proposed in Ref. [50]. The Adiabatic Bragg soliton compressor scheme is based on adiabatic soliton compression using a nonuniform grating in which the dispersion decreases along the grating. This technique has the advantage that it only requires one component (i.e. one grating) and produces a clean nearly transform limited pulse.

The scheme that we consider in this study, relies on self-similar pulse compression in nonlinear fiber Bragg gratings operating in transmission. The dispersion profile required to support self-similar solution is the exponentially decreasing dispersion profile.

To vary the dispersion along the propagation direction *z*, we can vary the period of the grating Λ, the average effective index *n*, or the grating modulation depth Δn. The Bragg frequency is directly related to the period and the average index through $\frac{n}{c}\omega_B = \frac{\pi}{\Lambda}$, so that varying the period or the average index will mainly vary δ (and, more weakly, κ) [50]. By contrast, varying Δn will vary only κ [50]. The detuning has to be positive ($\delta > \kappa$) to yield anomalous dispersion and soliton effects.

In summary, we use Table 1.1 to give a comparison between different nonlinear pulse compression schemes.

1.3 Modelling

Light propagation in optical fibers is governed by the nonlinear schrödinger (NLS) equation which is derived from the Maxwell's equation [5] using the slowing varying envelope approximation.

The basic form of the NLS equation contains chromatic dispersion and Kerr effect. We can include higher-order dispersion and nonlinear effects by adding the appropriate terms in the NLS equation. Normally, for pulse width larger than 1ps, we can neglect higher-order dispersions, self-steepening, and intrapulse Raman scattering [15]. Split-step Fourier method [Appendix B] is used to solve NLS equation and cubic-quintic NLS equation,

Nonlinear pulse propagation in FBGs is governed by the nonlinear coupled mode equations (NLCMEs) which describe the coupling between the forward and backward traveling modes in the FBGs [6]. When the center frequency of the pulse is being tuned outside but close to the PBG structure, one can apply the multiple scale analysis [6, 51, 52] to reduce the NLCMEs into the NLS equation.

We use implicit fourth-order Runge-Kutta method described in Ref. [53] to solve NLCMEs, and compare the results with that of the NLS approximation. A brief introduction on the implicit fourth-order Runge-Kutta method is offered in Appendix G.

Besides numerical methods, an effective way to describe the pulse dynamics is the pulse parameter equations. With a suitable ansatz, one can derive a set of ordinary differential equations (ODEs) governing the evolution of the pulse parameters. Typically, a set of coupled ODEs has to be solved numerically by the Runge-Kutta method. Results can be obtained much faster by this semi-analytic method than full simulations. However, the pulse dynamics depend on the chosen ansatz. As we do not know the exact solution form, the results obtained from the pulse parameter equations are only approximations.

1.4 Outline

In this thesis, we study the compression of linearly chirped self-similar pulses. Efficient pulse compression can be achieved with appropriate induced dispersions, such as the exponentially decreasing dispersion.

Split-step Fourier method and implicit fourth-order Runge-Kutta method will be introduced in the Appendix B and G, respectively. In Chapter 2, we study the linearly chirped self-similar pulse compression in nonlinear fiber Bragg gratings (NFBGs) with exponentially decreasing dispersion in the NLS limit. We discuss the physical mechanisms that determine the evolution of the self-similar soliton. We demonstrate the stepwise approximation of the exponentially decreasing dispersion profile, and numerical simulation results confirm that the compressed pulse is nearly chirp-free and almost pedestal-free. We show that the number of concatenated sections is associated with the compression factor and initial chirp

value. A simple pre-chirper is used to add the required chirp profile to initial chirp-free hyperbolic secant pulse or Gaussian pulse. We have found that the initial Gaussian profile evolves into a hyperbolic secant profile after the compression in the NFBG. A comparison between NLS equation and pulse parameter evolution equations will be given. The NLS equation in Chapter 2 only considers the second order dispersion, while the generalized NLCMEs, which include all orders of dispersions, are more accurate in describing the pulse propagation in nonlinear gratings. Chapter 3 presents the simulation results of the NLCMEs. Chapter 4 considers the evolution of nonlinear optical pulses in the cubic-quintic nonlinear media wherein the pulse propagation is governed by the generalized NLS equation with exponentially varying dispersion, cubic and quintic nonlinearities, and gain/loss. From the stability analysis, we show that the solitary wave solution in the anomalous dispersion regime is stable whereas the solitary wave solution in the normal dispersion regime is unstable. Numerical simulations results show that competing cubic-quintic nonlinearities stabilize the chirped soliton pulse propagation against perturbations in the initial soliton pulse parameters. Finally we conclude the thesis and discuss the future work in Chapter 5.

Table 1.1: Comparison between different nonlinear pulse compression schemes.

	Large compression ratio	Pedestal-free	Chirp-free / Almost chirp-free	Avoid wave breaking at high powers	Short length
Higher order soliton compression	✓				
Adiabatic pulse compression in fibers			✓		
Adiabatic pulse compression in NFBGs			✓		✓
Self-similar pulse compression in fibers	✓	✓	✓	✓	
Self-similar pulse compression in NFBGs	✓	✓	✓	✓	✓

Chapter 2

Pulse Compression in Nonlinear Fiber Bragg Gratings in the NLS Limit

We demonstrate almost chirp-free and pedestal-free optical pulse compression in NFBGs with exponentially decreasing dispersion. The exponential dispersion profile can be well approximated by a few gratings with different constant dispersions. In Section 2.1.1, we investigate pedestal-free Bragg soliton pulse compression near the photonic bandgap structure using self-similar analysis. We discuss the physical mechanisms that determine the evolution of the self-similar soliton in Section 2.1.2 and pulse parameter evolution equations in Section 2.1.3. To check the possibility of soliton pulse propagation of the variable coefficient NLS equation, we apply the well known Painlevé analysis in Section 2.1.4. We present the essential steps for deriving the exact soliton solution of the variable coefficient NLS equation using the Bäcklund transformation method in Section 2.1.5. Section 2.2 demonstrates the stepwise approximation of the exponentially decreasing dispersion profile, and numerical simulation results confirm that the

compressed pulse is nearly chirp-free and almost pedestal-free. We show that the required number of sections is proportional to the compression ratio, but inversely proportional to the initial chirp value. Section 2.3 proposes a compact pulse compression scheme, which consists of a linear grating and a nonlinear grating, to effectively compress both hyperbolic secant and Gaussian shaped pulses. We have found that the initial Gaussian profile evolves into a hyperbolic secant profile after the compression in the NFBG. The comparison between simulation of the NLS equation and pulse parameter evolution equations will be given.

2.1 Compression of Chirped Optical Pulses

2.1.1 Self-Similar Analysis

Nonlinear pulse propagation in FBGs is governed by the nonlinear coupled mode equations which describe the coupling between the forward and backward traveling modes in the FBGs [6]. When the center frequency of the pulse is being tuned outside but close to the PBG structure, one can apply the multiple scale analysis [6, 51, 52] to reduce the NLCMEs into a NLS-type equation as

$$i\frac{\partial E}{\partial z} - \frac{\beta_2(z)}{2}\frac{\partial^2 E}{\partial t^2} + \gamma_g |E|^2 E = 0, \tag{2.1}$$

where $E(z,t)$ is the envelope of the Bloch wave associated with the grating, z is the distance variable, t is the time variable, $\beta_2(z)$ represents the dispersion of the grating, and γ_g is the effective nonlinear coefficient. For Eq. (2.1), adiabatic Bragg soliton pulse compression has been discussed wherein the maximum compression factor of 4 was achieved [50, 52] and the pedestal generated is very small [50]. Later, using perturbation theory, Tsoy and Sterke [54, 55] have investigated the pulse compression based on the perturbed NLS equation in NFBG. Contrary to the above pulse compression studies, recently, Rosenthal et al.

have proposed the pulse compression based on the reflected pulse in NFBG [56] and Bragg soliton pulse compression based on in-gap soliton [57].

More recently, the self-similar analysis has been utilized to investigate linearly chirped pulses in optical fibers and fiber amplifiers [25−28]. Self-similarity is a common phenomenon in nature. Common objects such as tree branches, snowflakes, clouds, rivers, or shorelines look similar at a wide range of magnification scales. An object is said to be self-similar if it looks roughly the same on any scale. Thus, self-similarity is defined as the property whereby an object or a mathematical function preserves its structure when multiplied by a certain scale factor [58]. Self-similarity however is more than a curiosity of nature. Theoretical studies based on the self-similarity analysis of the NLS equation with constant gain, have revealed that the interplay of normal dispersion, nonlinearity, and gain produces a linearly chirped pulse with a parabolic intensity profile which resists the deleterious effects of optical wave-breaking [25]. Asymptotic self-similar solitary pulses have been investigated using NLS-type equations in the presence of gain [26]. Chirped solitary pulse compression has been demonstrated in these optical amplifiers. In the following, we use self-similar analysis to show that it is possible to achieve pedestal-free compression with maximum compression factor beyond the limit obtained by the adiabatic compression process. Eq. (2.1) has the well known soliton solutions when the dispersion and nonlinearity are constant. We are concerned here, however, with solutions characterized by a linear chirp. The complex function $E(z,t)$ can be written as

$$E(z,t) = U(z,t)\exp\left[i\Phi(z,t)\right], \tag{2.2}$$

where U and Φ are real functions of z and t. In general case when the coefficients of the NLS equation are functions of the distance z, the amplitude

$U(z,t)$ of the self-similar solutions has the form:

$$U(z,t) = \frac{1}{\sqrt{\Gamma(z)}} R(\theta),$$ (2.3)

where the scaling variable θ is

$$\theta = \frac{t - T_c}{\Gamma(z)}.$$ (2.4)

Energy is conserved by the definition of the amplitude shown in Eq. (2.3) and Eq. (2.4). Here $\Gamma(z)$ and $R(\theta)$ are some functions which we seek, where without loss of generality we can assume that $\Gamma(0) = 1$.

Below we look for self-similar solutions of Eq. (2.1) assuming that the phase has a quadratic form:

$$\Phi(z,t) = \alpha_1(z) + \frac{\alpha_2(z)}{2}(t - T_c)^2.$$ (2.5)

Equations (2.1) – (2.5) yield the function $\alpha_2(z)$ and $\Gamma(z)$ as:

$$\alpha_2(z) = \frac{\alpha_{20}}{1 - \alpha_{20}D(z)}, \quad \Gamma(z) = 1 - \alpha_{20}D(z),$$ (2.6)

where the function $D(z)$ is:

$$D(z) = \int_0^z \beta_2(z')dz'.$$ (2.7)

The self-similar solution is possible if and only if the dispersion varies exponentially, i.e.

$$\beta_2(z) = \beta_{20} \exp(-\sigma z), \sigma = \alpha_{20}\beta_{20}.$$ (2.8)

The function $R(\theta)$ obeys the nonlinear differential equation

$$\frac{d^2R}{d\theta^2} + \frac{2\Gamma^2(z)}{\beta_2(z)} \frac{d\alpha_1}{dz} R - \frac{2\Gamma(z)\gamma(z)}{\beta_2(z)} R^3 = 0.$$ (2.9)

24

In the general case the coefficient in Eq. (2.9) is a function of the variable z but the function $R(\theta)$ depends only on the scaling variable θ. Therefore, Eq. (2.9) has nontrivial solution if and only if the coefficients of Eq. (2.9) are constants.

$$\lambda_1 = -\frac{2\Gamma^2(z)}{\beta_2(z)}\frac{d\alpha_1}{dz},$$ (2.10)

$$\lambda_2 = -\frac{\Gamma(z)\gamma(z)}{\beta_2(z)}.$$ (2.11)

Equation (2.11) yields

$$\alpha_1(z) = \alpha_{10} - \frac{\lambda_1}{2}\int_0^z \frac{\beta_2(z')}{\left[1-\alpha_{20}D(z')\right]^2}dz',$$ (2.12)

where λ_1 is the integration constant. The coefficient λ_2 is given by

$$\lambda_2 = -\gamma_g / \beta_{20}.$$

Integrating Eq. (2.9) for the case $\beta_2\gamma_g < 0$ and using Eq. (2.3), we find the amplitude of the solitary wave solution:

$$U(z,t) = \sqrt{\frac{|\beta_2(z)|}{\gamma_g}}\frac{1}{T_0\left[1-\alpha_{20}D(z)\right]}\mathrm{sech}\left\{\frac{t-T_c}{T_0\left[1-\alpha_{20}D(z)\right]}\right\},$$ (2.13)

where the integration constant λ_1 is equal to $1/T_0^2$, and T_0 is the initial pulse width parameter.

Finally, the chirped bright solitary wave is given by

$$E(z,t) = \sqrt{\frac{|\beta_2(z)|}{\gamma_g}}\frac{1}{T_0\left[1-\alpha_{20}D(z)\right]}\mathrm{sech}\left\{\frac{t-T_c}{T_0\left[1-\alpha_{20}D(z)\right]}\right\}\exp\left[i\alpha_1(z)+i\frac{\alpha_2(z)}{2}(t-T_c)^2\right],$$

(2.14)

Note that the FWHM of the pulse is given by $1.76T_0$. Equations (2.8) and (2.14) are the key results of this work which state that efficient pedestal-free Bragg soliton pulse compression is possible using NFBG with an exponentially decreasing dispersion profile. Since the pulse width parameter is given by $T(z) = T_0 \exp(-\sigma z)$, the pulse compression ratio is $T_0 / T(z) = \exp(\sigma z)$ which is the same as the ratio of the initial dispersion to the final dispersion. We note that while the chirp parameter increases exponentially $\alpha_2(z) = \alpha_{20} \exp(\sigma z)$, the normalized chirp value decreases exponentially $C(z) = \alpha_2(z) T^2(z) = \alpha_{20} T_0^2 \exp(-\sigma z)$. Thus as the self-similar soliton compresses, the normalized chirp decreases. Consequently, the time-bandwidth product approaches 0.315, which is the value for transform-limited hyperbolic secant pulses. Figure 2.1(a), (b) and (c) show the evolution of pulse shapes, optical spectra, and time-bandwidth product of the compression of a self-similar soliton in which the initial pulse parameters are $T_0 = 10$ ps and $\alpha_{20} = -0.01$ THz^2, respectively. The nonlinear grating has an exponentially decreasing profile with $\beta_2(z) = \beta_{20} \exp(-\sigma z)$ where initial dispersion value $\beta_{20} = -33$ ps^2/cm [2] and the dispersion decay rate $\sigma = 0.33$ /cm. The nonlinear coefficient of the grating $\gamma_g = 15 / W / km$. The time-bandwidth product decreases from 0.761 to 0.316 after the soliton travels 12 cm of the nonlinear grating.

2.1.2 Evolution of the Self-Similar Soliton

In this section, we will study how the physical mechanisms determine the evolution of the self-similar soliton of Eq. (2.14) as the grating and pulse

26
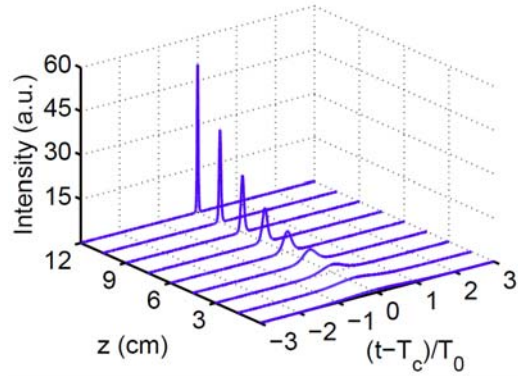
(a)
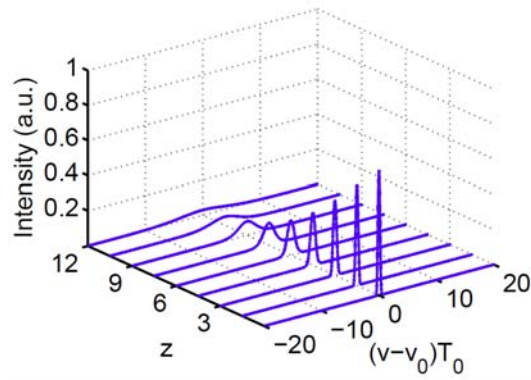
(b)
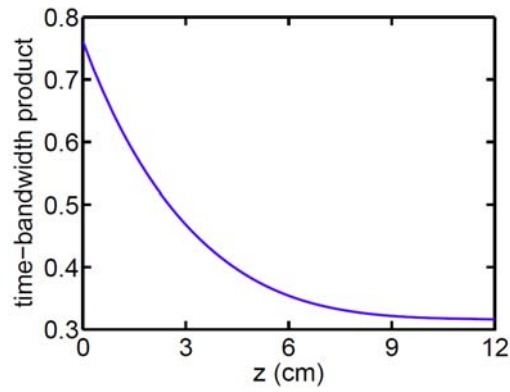
(c)

Figure 2.1: Evolution of (a) pulse shapes, (b) spectra and (c) time-bandwidth product of a chirped self-similar soliton. The initial pulse parameters are $T_0 = 10$ ps and $\alpha_{20} = -0.01$ THz^2. The grating parameters are $\beta_{20} = -33$ ps^2/cm, $\sigma = 0.33$ /cm, $\gamma_g = 15$ /W/km, and $L = 12$ cm.

parameters vary. Since the soliton is chirped, the soliton evolution depends on the interaction between the pulse chirp and the grating dispersion and also between the grating dispersion and the nonlinearity. The effect of dispersion and nonlinearity can be measured by the distance-dependent dispersion length and nonlinear length which are defined respectively as $L_D(z) = T^2(z)/|\beta_2(z)|$ and $L_N(z) = 1/\gamma_g(z)/P(z)$ where $P(z)$ is the peak intensity of the optical pulse. The dispersion length is defined for a chirp-free pulse. To account for the effect of the pulse chirp, we define a chirp length in analogy to the dispersion length as $L_C(z) = T^2(z)/|C(z)|/|\beta_2(z)|$. For a linear medium governed by GVD only, the dispersion length and the chirp length completely characterize the evolution of a chirped pulse. For the self-similar soliton in Eq. (2.14), we have $L_D(z) = L_N(z)$. We also find that the chirp length $L_C = 1/\sigma$ which is the characteristic length of the exponentially varying dispersion. Thus the self-similar soliton evolves in such a way that the dispersion length always equals the nonlinear length while the chirp length remains constant.

The evolution of the self-similar soliton depends on the relative strength of the chirp length and the dispersion length. For the ease of discussion, we assume in the following that the dispersion is exponentially decreasing, i.e. $\sigma > 0$. Since the nonlinear length or dispersion length is exponentially decreasing, even if the effect of chirp dominates initially, i.e. $L_N \gg L_C$ at $z = 0$, the nonlinear effect will eventually become dominant as the distance becomes very large, i.e. $L_N \ll L_C$ as $z \to \infty$. When the effect of chirp is large, the self-similar soliton evolves quasi-linearly. The compression of the soliton is mainly due to the unwinding of the pulse chirp by the grating dispersion. When the effect of chirp is small, the soliton

evolves nonlinearly. The soliton compression is mainly due to the interplay between the dispersion effect and the self-phase modulation. Thus the physical mechanism governing the compression of the self-similar soliton depends on the initial grating parameters. Note that the initial soliton chirp coefficient $\alpha_{20} = \sigma / \beta_{20}$, where β_{20} / σ is the total dispersion of the FBG with infinite length. The total dispersion of FBG with length L is $S(L) = (\beta_{20} / \sigma)[1 - \exp(-\sigma L)]$. Thus if $L_N \gg L_C$ at $z = 0$, the soliton will evolve quasi-linearly in the beginning of the grating, then evolve according to a combination of linear and nonlinear effects around intermediate distance, and finally, nonlinearly for large value of z. If $L_N \sim L_C$ or $L_N \ll L_C$ at $z = 0$, we will only observe part of the transition from quasi-linear evolution to nonlinear evolution. To demonstrate that the soliton evolves quasi-linearly when $L_N \gg L_C$, we consider a distance z_0 such that $\varepsilon = L_C / L_D(z_0) \ll 1$. We then normalize Eq. (2.1) as

$$i\frac{\partial U}{\partial \zeta} - \frac{\operatorname{sgn}(\beta_{20}) f(\zeta)}{2} \frac{\partial^2 U}{\partial \tau^2} + |U|^2 U = 0, \tag{2.15}$$

where $\zeta = z / L_{D_0}$, $\tau = (t - T_c) / T_0$ and $U = E \sqrt{\gamma_g L_{N_0}}$ are the normalized space, time and electric field, respectively. The parameters L_{D_0} and L_{N_0} are the dispersion length and nonlinear length at $z = z_0$. The function $f(\zeta) = \beta_2(z) / \beta_{20} = \exp(-\zeta / \varepsilon)$ is a rapidly varying function of ζ. We also note that the quadratic phase in Eq. (2.14) in the normalized variable is given by $\phi = \eta(\zeta) + \exp(\zeta / \varepsilon) \tau^2 / 2 / \varepsilon$ where $\eta(\zeta) = \alpha_1(L_{D0}\zeta)$. Thus the quadratic phase of the soliton is a large and rapidly varying function of ζ. We use the multiple length scale expansion to determine the evolution of the soliton under a rapidly

varying dispersion and large and rapidly varying chirp. We introduce the fast and slow space and time variables

$$\zeta_1 = \zeta/\varepsilon, \ \tau_1 = \tau/\varepsilon,$$
$$\zeta_2 = \zeta, \qquad \tau_2 = \tau,$$
(2.16)

where the subscript '1' and '2' represent the fast and slow variables, respectively. The normalized pulse is now a function of both the fast and slow variables, i.e. $U(\zeta_1,\zeta_2,\tau_1,\tau_2)$. We then expand the normalized electric field $U(\zeta_1,\zeta_2,\tau_1,\tau_2)$ in terms of the small parameter ε as

$$U(\zeta_1,\zeta_2,\tau_1,\tau_2) = U^{(0)}(\zeta_1,\zeta_2,\tau_1,\tau_2) + \varepsilon U^{(1)}(\zeta_1,\zeta_2,\tau_1,\tau_2) + \varepsilon^2 U^{(2)}(\zeta_1,\zeta_2,\tau_1,\tau_2) + \dots$$
(2.17)

where $U^{(j)}(\zeta_1,\zeta_2,\tau_1,\tau_2)$, $j = 0,1,2,\cdots\infty$ is the j-th order expansion of $U(\zeta_1,\zeta_2,\tau_1,\tau_2)$.

Finally, substitution of Eqs. (2.16) and (2.17) into Eq. (2.15) and at order $1/\varepsilon$, we obtain

$$i\frac{\partial V^{(0)}}{\partial \zeta_1} - \frac{1}{2}\mathrm{sgn}(\beta_{20})\exp(-\zeta_1)\frac{\partial^2 V^{(0)}}{\partial \tau_1^2} = 0,$$
(2.18)

where we further assume a separation of variables $U^{(0)}(\zeta_1,\zeta_2,\tau_1,\tau_2) = V^{(0)}(\zeta_1,\tau_1)W^{(0)}(\zeta_2,\tau_2)$ because the coefficient in Eq. (2.18) depends on the fast variables only. Thus from Eq. (2.18), when $\varepsilon = L_C / L_N(z_0) \ll 1$, the fast behavior of the soliton is governed by the grating dispersion only. The nonlinear effect affects the soliton evolution at slow space and time scales. The above analysis demonstrate that the self-similar chirped soliton evolves quasi-linearly when $L_N \gg L_C$. As an example, Fig. 2.2(a) shows the evolution of the FWHM of the chirped hyperbolic secant pulse in which $T_0 = 80$ ps and $\alpha_{20} = -0.01$ THz^2. The grating parameters are $\beta_{20} = -33$ ps^2/cm,

$L = 6$ cm and $\sigma = 0.33$/cm. The dots and solid curve represent the evolution of FWHM with and without the nonlinearity respectively. Initially at $z = 0$, $L_D \sim 194$ cm, $L_C \sim 3$ cm, $\varepsilon \sim 0.0156$. At grating length of 6 cm, $L_D \sim 26.8$ cm, $L_C \sim 3$ cm, $\varepsilon \sim 0.11$. We observe that the evolution of the FWHM of the soliton shown in Fig. 2.2(a) is well approximated by the linear evolution. Figure 2.2(b) plots the evolution of FWHM of an initial chirp free hyperbolic secant pulse with the same parameters as the chirped soliton in Fig. 2.2(a) except that $\alpha_{20} = 0$. The dots and solid curve represent the evolution of FWHM with and without the nonlinearity respectively. We observe that the pulse width does not vary significantly and the linear evolution does not agree the nonlinear evolution at all. Thus demonstrating the importance of the chirp in the self-similar soliton evolution.

Finally if $L_N \ll L_C$ at $z = 0$, then grating dispersion $\beta_2(z) = \beta_{20} \exp(-\sigma z)$ varies slowly and the normalized chirp $C(z) = C_0 \exp(-\sigma z)$ is very small. Hence in the distance on the order of L_N, the pulse evolution is governed mainly by the interaction between the dispersion and the nonlinearity. The chirp affects the pulse evolution only at distance on the order of L_C.

2.1.3 Pulse Parameter Evolution Equations

Equation (2.14) is the exact soliton solution to Eq. (2.1). To determine the pulse compression when the grating dispersion profile is not exponential varying or the initial pulse deviates from the self-similar soliton solution, we can either numerically simulate Eq. (2.1) or use semi-analytical techniques such as the Lagrangian variational method (LVM) [59] or the projection operator method (POM) [60, 61] to derive the equations governing the evolution of the pulse
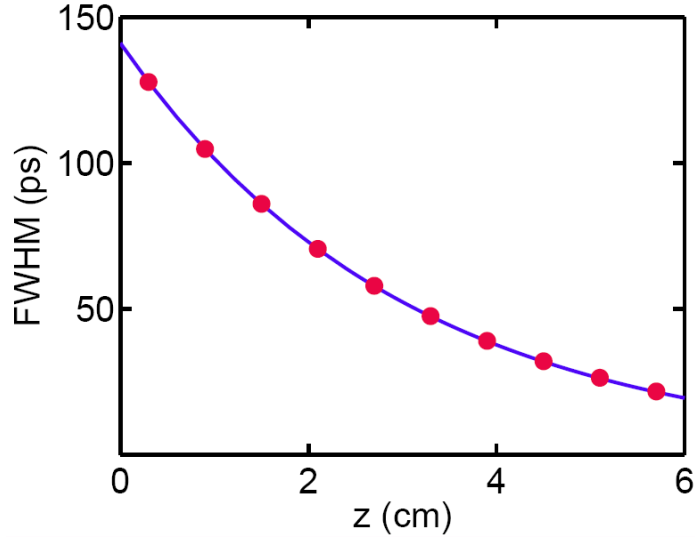
(a)
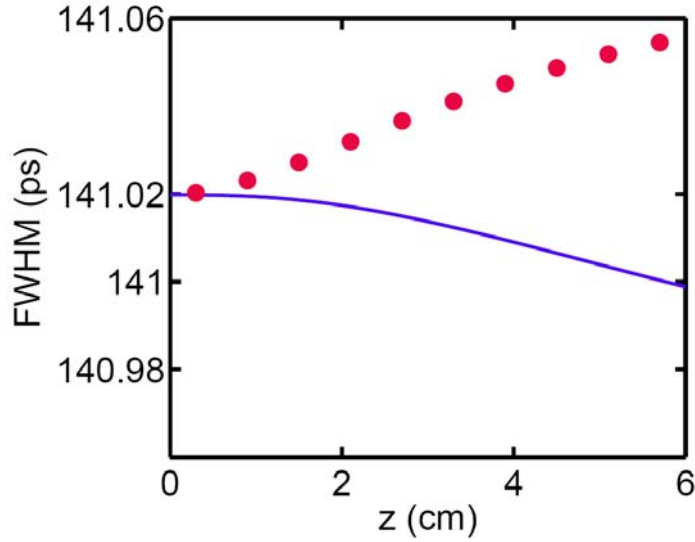
(b)

Figure 2.2: Evolution of the FWHM of (a) chirped hyperbolic secant pulse ($T_0 = 80$ ps, $\alpha_{20} = -0.01$ THz^2) and (b) unchirped hyperbolic secant pulse ($T_0 = 80$ ps , $\alpha_{20} = 0$) in exponentially decreasing dispersion ($\beta_{20} = -33$ ps^2/cm, $\sigma = 0.33$ /cm). The dots and solid curve represent the evolution with nonlinearity ($\gamma_g = 15$ / W/ km) and without nonlinearity, respectively.

parameters. In both the LVM and the POM, the success of the approximation depends on the ansatz chosen. For the NLS-type equation like Eq. (2.1), both hyperbolic secant pulse shape [Eq. (2.19)] and Gaussian pulse shape [Eq. (2.20)] with a quadratic phase variation are common ansatz, i.e.

$$E = x_1 \text{sech}\left(\frac{t}{x_2}\right)\exp\left(\frac{ix_3 t^2}{2} + ix_4\right), \tag{2.19}$$

$$E = x_1 \exp\left(-\frac{t^2}{x_2^{\,2}} + \frac{ix_3 t^2}{2} + ix_4\right), \tag{2.20}$$

where $x_i(z)$, $i = 1, 2, \ldots, 4$ are the amplitude, pulse width, chirp, and phase of the optical pulse. Equations (2.21) give the equations governing the evolution of the pulse parameters generated by the LVM and the POM using the hyperbolic secant pulse and Gaussian pulse ansatz. The coefficients c_i, $i = 1,2,3,4$ are constants indepent of the distance z but depend on the reduction method and the ansatz used. In other words, the pulse parameters equations resulting from the two reduction methods and two different pulse ansatz have the same function form. Only some of the coefficients in the equations are different.

$$\frac{dx_1}{dz} = \frac{1}{2}\beta_2(z) x_1 x_3,$$

$$\frac{dx_2}{dz} = -\beta_2(z) x_2 x_3,$$

$$\frac{dx_3}{dz} = \beta_2(z)\left(x_3^{\,2} - c_1 \frac{1}{x_2^{\,4}}\right) - c_2 \frac{\gamma_g x_1^{\,2}}{x_2^{\,2}}, \tag{2.21}$$

$$\frac{dx_4}{dz} = c_3 \frac{\beta_2(z)}{x_2^{\,2}} + c_4 \gamma_g x_1^{\,2}.$$

Table 2.1 lists the values of the constant c_i's for different combinations of the reduction methods and ansatz used.

Table 2.1: The values of the constants c_i in Eq. (2.21). LVM stands for Lagrangian variational

method and POM stands for the projection operator method.

Method	Ansatz	c_1	c_2	c_3	c_4
LVM	hyperbolic secant	$\dfrac{4}{\pi^2}$	$\dfrac{4}{\pi^2}$	$\dfrac{1}{3}$	$\dfrac{5}{6}$
POM	hyperbolic secant	$\dfrac{30}{\pi^4}$	$\dfrac{30}{\pi^4}$	$\left(\dfrac{1}{6}+\dfrac{5}{4\pi^2}\right)$	$\left(\dfrac{2}{3}+\dfrac{5}{4\pi^2}\right)$
LVM/POM	Gaussian	4	$\sqrt{2}$	1	$\dfrac{5}{4\sqrt{2}}$

For ansatz like Gaussian which has an inherent symmetric property between the pulse parameters will result the same set of ODEs derived either from the LVM or POM. But for ansatz like hyperbolic secant, which lacks this kind of symmetric property between the pulse parameters, one needs to derive both sets of ODEs to study their dynamics [62].

In general, the solutions to the pulse parameter equations are only the "best" approximation to the solution of the original equations under the assumption of the ansatz and the reduction method used. However, if the functional form of the ansatz coincides with that of the exact solution, as in the case of the ansatz Eq. (2.19) to Eq. (2.20), then the pulse parameter equations will yield the exact solution to the original equations. Using the LVM and the hyperbolic secant pulse as ansatz, the first three equations in Eq. (2.21) can be written as

$$\frac{dx_1}{dz}=\frac{x_1}{2L_C(z)},$$

$$\frac{dx_2}{dz}=-\frac{x_2}{L_C(z)}, \qquad\qquad (2.22)$$

$$\frac{dx_3}{dz}=\frac{x_3}{L_C(z)}+\frac{4}{\pi^2 x_2^2}\left[\frac{1}{L_D(z)}-\frac{1}{L_N(z)}\right],$$

where $L_C(z)=1/(x_3\beta_2)$, $L_D(z)=-x_2^2/\beta_2$ and $L_N(z)=1/\left(\gamma_g x_1^2\right)$ represent the

chirp, dispersion and nonlinear lengths, respectively. Equation (2.22) can be solved readily if we assume $L_D(z) = L_N(z)$, i.e. the well-known condition in which the dispersion length equals to the nonlinear length. The solutions are

$$x_1(z) = x_1(0)\exp\left(\frac{1}{2}\int_0^z 1/L_C(z')dz'\right), \quad x_2(z) = x_2(0)\exp\left(-\int_0^z 1/L_C(z')dz'\right), \quad \text{and}$$

$$x_3(z) = x_3(0)\exp\left(\int_0^z 1/L_C(z')dz'\right).$$ It is then necessary to substitute $x_1(z)$, $x_2(z)$ and $x_3(z)$ into the condition $L_D(z) = L_N(z)$ to check for consistency. There are two possibilities for the parameter L_C that needed to be treated separately. First, we consider $L_C \to \infty$, i.e. $x_3\beta_2 = 0$, which means $x_3(z) = 0$ since $\beta(z) \neq 0$. In this case, x_1, x_2 and x_3 are independent of z. The condition $L_D(z) = L_N(z)$ means that $\beta_2(z) = \beta_{20}$ is a constant and the parameters x_1 and x_2 satisfy the condition $-x_2^2/\beta_{20} = 1/(\gamma_g x_1^2)$. In other words, we obtain the conventional soliton solutions of the NLS equation with the constant dispersion. Next, we consider the case when L_C is finite. Thus

$$\beta_2(z) = \left[1/x_3(0)/L_C(z)\right]\exp\left(-\int_0^z 1/L_C(z')dz'\right).$$ The condition $L_D(z) = L_N(z)$, which becomes $-x_2(0)^2 x_3(0) L_C(z) = 1/\left[\gamma_g x_1(0)^2\right]$, can be satisfied if and only if L_C is a constant independent of z. As a result $x_1(z)$, $x_2(z)$, $x_3(z)$ and $\beta_2(z)$ vary exponentially with distance z which is the chirped soliton solution of NLS equation with exponentially varying dispersion. In summary, we observe that the soliton solutions to the NLS equation with the constant dispersion and exponentially varying dispersion share the same characteristics; both of them evolve such that the dispersion length equals to the nonlinear length and the chirp

length remains unchanged.

In the following, we will use the pulse parameter equations [Eq. (2.21)] as well as numerical simulation [Eq. (2.1)] to study the self-similar optical pulse compression.

2.1.4 Painlevé Analysis

To check the possibility of soliton pulse propagation of Eq. (2.1), we apply the well known Painlevé analysis. The Painlevé analysis implies that the dispersion must vary in an exponential manner (or the dispersion should be constant) for the system equation (2.1) to be completely integrable (for details refer Appendix H). That is, soliton solution is possible if the dispersion varies exponentially as

$$\beta_2(z) = \beta_{20} \exp(-\sigma z), \tag{2.23}$$

where β_{20} and σ are integration constants. It should be emphasized that the exponential scaling (for the dispersion profile), obtained here by Painlevé analysis, is the same as that obtained through self-similar analysis [26]. The integrable form of Eq. (2.1) can be written as (with $\sigma = \alpha_{20}\beta_{20}$)

$$iE_z - \frac{\beta_{20}\exp(-\alpha_{20}\beta_{20}z)}{2}E_{tt} + \gamma_g |E|^2 E = 0. \tag{2.24}$$

We would like to point out a conjecture regarding the resonance values derived in the Painlevé analysis. The resonances $r = -1,\ 0,\ 3,\ 4$ obtained here for the variable coefficient NLS equation [Eq. (2.1)] are the same as those for the constant coefficient NLS equation. Past experience has shown that such coincidences usually imply that the newly derived integrable nonlinear evolution equation could be connected to existing systems of equations [63]. This is in fact true and there is a connection between the variable coefficient NLS equation shown by Eq. (2.24) and the conventional NLS equation. We consider the gauge transformation

$$E = Q \exp(i\alpha_{20} T^2 / 4); \; t = T \exp(-\alpha_{20}\beta_{20} z / 2), \tag{2.25}$$

which maps the exponentially varying dispersion NLS equation [Eq. (2.24)] into the following variable coefficient NLS equation:

$$iQ_z - \frac{\beta_{20}}{2} Q_{TT} + \gamma_g |Q|^2 Q - \frac{\beta_{20}}{8} \alpha_{20}^2 T^2 Q - i\frac{\beta_{20}}{4} \alpha_{20} Q = 0. \tag{2.26}$$

Eq. (2.26) has been analyzed for its integrability through Painlevé analysis and possesses a transformation connecting it to constant coefficient NLS equation [64].

Thus the above mentioned conjecture about the resonance values of the Painlevé analysis holds good as there is a connection between the integrable dispersion varying NLS equation [Eq. (2.24)] and the conventional constant coefficient NLS equation. Equation (2.26) is also applicable in many physical contexts like averaged dispersion managed (DM) fiber system, nonlinear compression of chirped solitary waves, quasi-soliton propagation in DM optical fiber and other settings [24, 65−69]. More recently, 1−, 2− bright and dark solitons, as well as the periodic wave solutions were also calculated for the variable coefficient NLS equation by the Hirota bilinear method [70]. Here, it should be emphasized that even though the results on Painlevé analysis, for the NLS equation with the variable coefficient, have been reported in different contexts in the literature, it is fair to say that there is no clear physical understanding has emerged regarding the existence and the formation of chirped optical solitons in nonlinear optical media. Therefore, in what follows, we will address this issue.

2.1.5 Chirped Soliton: Bäcklund Transformation Method

Now we present the essential steps for deriving the exact soliton solution of the

variable coefficient NLS equation [Eq. (2.26)] using the Bäcklund transformation method. Before investigating the chirped soliton, it is the usual practice to construct the Lax pair associated with Eq. (2.26). The details of the Lax pair for the governing equation have been presented in the Appendix I [68]. To construct the chirped soliton of Eq. (2.26), we start with the zero-soliton solution $q = 0$. By using this trivial solution, the explicit form of $\Gamma(0)$ is obtained as

$$\Gamma(0) = \exp[\zeta(z,t) + i\theta(z,t)], \tag{2.27}$$

where $\zeta(z, t)$ and $\theta(z, t)$ are given by

$$\zeta(z,T) = 2\chi(z)T - 4\beta_{20}\int\sigma(z)\chi(z)dz, \tag{2.28}$$

$$\theta(z,T) = -2\sigma(z)T + 2\beta_{20}\int\left[\sigma^2(z) - \chi^2(z)\right]dz. \tag{2.29}$$

The explicit form of ζ and θ can be respectively derived from the above two equations using the variable spectral parameter (Appendix I). The one soliton solution for Eq. (2.26) can be written as

$$Q = \frac{2\chi(z)}{\mu}\operatorname{sech}(\zeta)\exp i\left[\left(\theta + \alpha_{20}T^2/4\right)\right], \tag{2.30}$$

where $\mu = \sqrt{-\gamma_g/\beta_{20}}$. Now using the 1–soliton solution [Eq. (2.30)] and the gauge transformation [Eq. (2.25)], the exact 1–soliton solution for the exponentially decreasing dispersion NLS equation [Eq. (2.24)] can be derived as (For simplicity, we assume $\lambda_{0I} = 1/(2T_0)$ and $\lambda_{0R} = 0$, where T_0 is real constant which represents the initial pulse width parameter):

$$E = \sqrt{\frac{-\beta_0}{\gamma_g}}\frac{e^{\alpha_{20}\beta_{20}z/2}}{T_0}\operatorname{sech}(\frac{te^{\alpha_{20}\beta_{20}z}}{T_0})\exp\left(i\frac{\alpha_{20}t^2e^{\alpha_{20}\beta_{20}z}}{2} - i\frac{e^{\alpha_{20}\beta_{20}z}}{2\alpha_{20}T_0^2}\right), \tag{2.31}$$

This soliton solution is similar to that reported earlier in the literature [24, 27, 71]. From the 1–soliton solution [Eq. (2.31)], it is clear that the soliton pulse intensity

and chirp are exponentially increasing and the width is exponentially decreasing at the same rate along the propagation direction. Our self-similar solution, in fact, chirped optical soliton, will have the same attractor property as shown by Fig. 2 in [72]. One of the properties of solitons is that initial pulses with different shapes will evolve into soliton pulses. In the terminology of nonlinear dynamics, solitons are attractors. For any initial pulse, we can numerically find out the asymptotical soliton solution, i.e. the soliton that it will evolve into. Then we can use the parameters of the soliton at this point as the normalization constant for the intermediate pulse.

In what follows, we discuss the implementation of chirped soliton as an effective pulse compression technique. We explain the physical process whereby we show how one could achieve the chirp free compressed pulse using the chirped soliton pulse compression technique through the phase plane diagram. We plot the the phase plane diagram in terms of the normalized chirp and intensity. Figure 2.3 explains the phase plane diagram in terms of normalized chirp and normalized intensity. The dot-dashed curve represents the pre-chirping of the initial chirp free hyperbolic secant pulse using the pulse parameter equations [Eq. (2.21), $\gamma_g = 0$]. Once the required chirp is achieved, then the pulse will be sent to nonlinear medium with exponentially decreasing dispersion. Hence the pulse will be compressed and the normalized chirp decreased in the compression process (solid curve). However, the residual chirp can be removed by the de-chirping process (dashed curve). In Fig. 2.3, pulse compression has been analyzed for two different initial chirp. In the first case, we consider the initial chirp to be $C(z) = -0.4012$. During the compression the chirp decreases and eventually the compressed pulse possess a tiny amount of chirp $C(z) =$
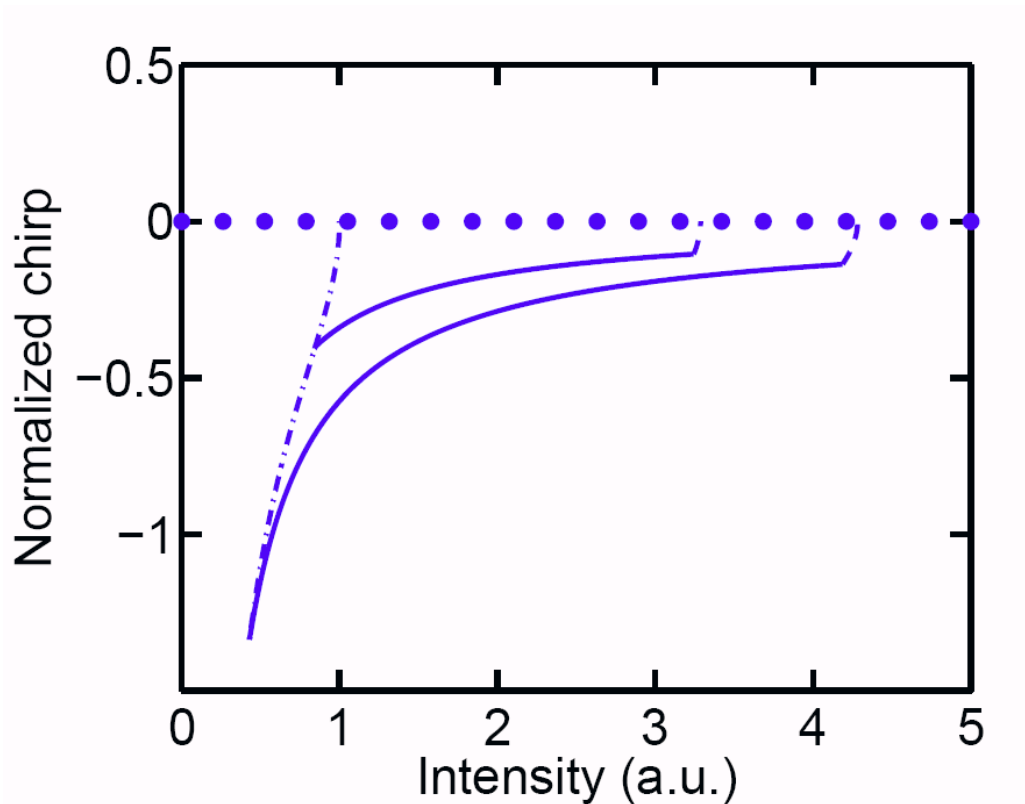
Figure 2.3: Phase plane diagram for the chirped soliton pulse compression in terms of normalized chirp and intensity: dot-dashed curve (pre-chirping); solid curve (compression); dashed curve (de-chirping).

–0.1046. If the initial chirp is relatively large, $C(z) = -1.3374$, the pulse undergoes relatively higher compression as shown in Fig. 2.3, and after compression chirp has been reduced to –0.1373. In both the cases, the compressed pulses possess a tiny amount of chirp. The chirp free pulses will be achieved by the de-chirping process (dashed curve).

2.2 Stepwise Approximation

Self-similar soliton requires the grating dispersion to vary exponentially. Although almost any grating profile can be manufactured using the state-of-the-art grating-writing techniques, fabrication of FBGs with an exact exponentially decreasing dispersion profile for an extended length is still challenging, especially when the grating length L is significantly larger than the characteristic length of the grating $L_C = 1/\sigma$. Similar problems have been encountered in utilizing dispersion decreasing fibers to reduce pulse broadening or the non-adiabatic effects caused by lumped amplifiers in fiber soliton transmission systems. Hasegawa et al. have shown that a stepwise dispersion-decreasing fiber can reduce the collision-induced jitters in soliton-based wavelength-division multiplexing systems [73] when the number of steps is sufficiently large (four or more). Therefore, in this section, we will study the feasibility of using the stepwise constant function to approximate the exponentially decreasing dispersion profile and determine the effects of the stepwise approximation (SWA) on the quality of the compressed pulse. SWA could be easily realized by concatenating FBGs with different uniform dispersions together. We assume that a non-uniform grating is divided into a number of sections with equal lengths. We then determine the total dispersion in each section of gratings and replace each section with a uniform grating with the same total dispersion value. If N sections are used,

the constant dispersion value b_i for the i-th section is given by

$$b_i = \int_{(i-1)\frac{L}{N}}^{i\frac{L}{N}} \beta_{20} \exp\left(-\alpha_{20}\beta_{20}z'\right)dz'. \qquad (2.32)$$

From Section 2.1.2, only one grating with constant dispersion will be sufficient to well approximate the pulse compression in the chirp dominated regime, i.e. $L_C \ll L_D$. In this case, the pulse evolves quasi-linearly as shown in Fig. 2.2. The pulse compression is determined by the total dispersion in the grating, and the detail of the dispersion profile is not important. This regime is obviously not of interest. Similarly, we are not interested in the nonlinear regime in which $L_C \gg L_D$, because the chirp is not playing an important role unless the grating length is of the order of L_C. We therefore will focus on pulse compression when $L_C \sim L_D$ and study both dispersion exponentially decreasing FBG (DDFBG) and the SWA to the dispersion profile.

As an example, we consider a grating length of $L_g = 6$ cm, the initial grating dispersion is $\beta_{20} = -33$ ps^2/cm and the decay rate $\sigma = 0.33$/cm. Thus the grating length is almost twice the characteristic length of grating. We assume an initial pulse width parameter $T_0 = 10$ ps, and the initial chirp coefficient $\alpha_{20} = -0.01$ THz^2. The initial dispersion length $L_{D_0} \sim 3$ cm. Hence initially $L_{D_0} = L_C$. At the end of the grating, the dispersion decreases to $\beta_2(L) \sim -4.56$ ps^2/cm and $L_D(L_g) \sim 0.14L_C$. Figure 2.4(a) shows the exponentially decreasing dispersion profile (dashed curve) and the 6-section SWA (solid curve). Figure 2.4(b) shows the initial pulse profile (dot-dashed curve) and compressed pulse using the DDFBG (solid curve) and the 6-section SWA (dashed curve). The compression ratio is ~7 in both cases. A small pedestal appears in the SWA

profile. The amount of pedestal generated is 1.12%. We calculate the pedestal using the method described in Ref. [74]. Figure 2.4(c) shows the evolutions of the dispersion length (L_D) and nonlinear length (L_N). In DDFBG, L_D always equals to L_N (dots). The nonlinear length of the SWA (dashed curve) agrees with that of exponentially decreasing dispersion profile while the dispersion length of the SWA (solid curve) shows discontinued jumps at the boundaries of each grating section. From Fig. 2.4(c), it is obvious that the dispersion length L_D of the SWA approximates the nonlinear length L_N very well, showing that the area under the solid curve is almost equal to the area under the dashed curve. Figure 2.4(d) and (e) give the evolutions of bandwidth and time-bandwidth product during pulse compression for both dispersion profiles, respectively. The solid curve and the dashed curve represent the results from the DDFBG, and the 6-section SWA, respectively. At the end of the grating the time-bandwidth product is 0.354 for the DDFBG and 0.359 for the 6-section SWA. Thus, the compressed pulse becomes almost transform-limited. We use the fourth order Runge-Kutta (RK) method to solve Eq. (2.21) using the hyperbolic secant pulse as ansatz. Figure 2.4(f) shows the evolution of the FWHM in the 6-section SWA, where the dots represent the self-similar soliton, the solid curve represents the simulation results of Eq. (2.1) using the SSFM, the dashed curve represents the results of the LVM using the hyperbolic secant pulse ansatz, and the dot-dashed curve represents the results of the POM using the hyperbolic secant pulse ansatz. The result from the LVM and the POM are similar and both approximate the exact solution very well. For pulse compression, it is important to determine the number of sections required to approximate the required exponentially decreasing dispersion. The number of sections required obviously depends on tolerance of the pedestal generated. The
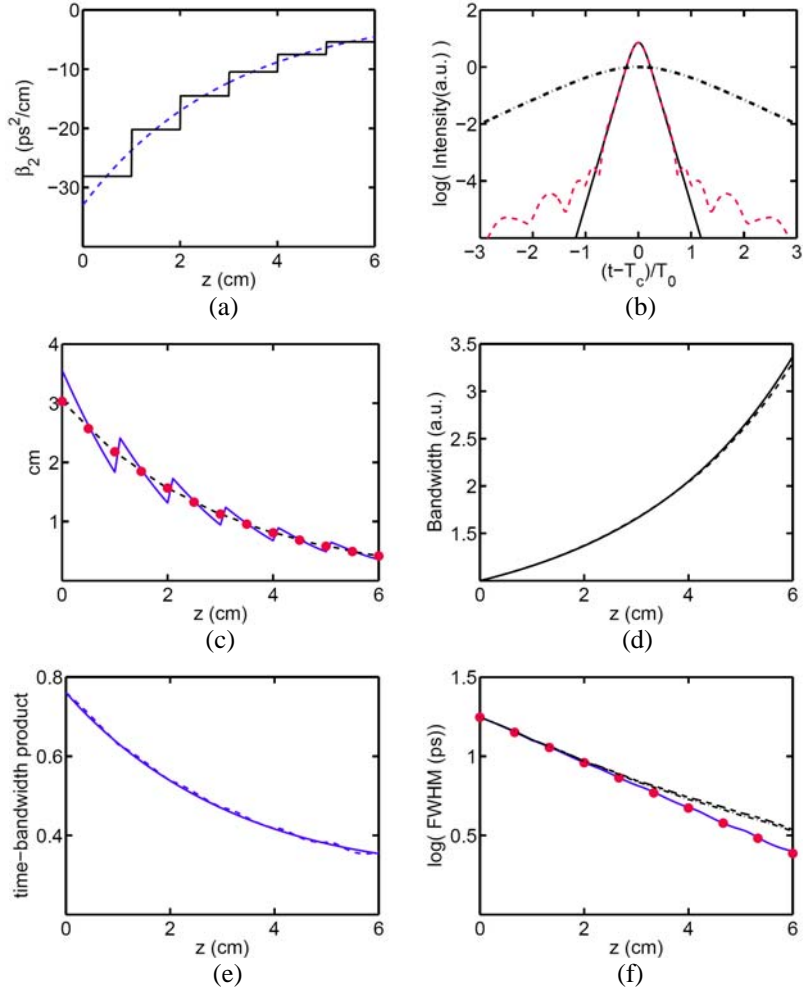
Figure 2.4: The exponentially decreasing dispersion profile (dashed curve) and the 6-section SWA (solid curve). (b) The pulse profile at $z = 0$ (dot-dashed curve) and at $z = 6$ cm in the DDFBG (solid curve) and the 6-section SWA (dashed curve). (c) Evolutions of the dispersion length L_D and nonlinear length L_N. The dots, dashed curve and solid curve represent L_D ($=L_N$) in DDFBG, L_N in SWA and L_D in SWA, respectively. (d) Bandwidth broadening in DDFBG (solid curve) and the 6-section SWA (dashed curve). (e) Time-bandwidth product for DDFBG (solid curve) and the 6-section SWA (dashed curve). (f) Evolution of FWHM in the 6-section SWA for the self-similar solutions (dots), the full numerical simulations (solid curve), the LVM with hyperbolic secant pulse ansatz (dashed curve), and the POM with hyperbolic secant pulse ansatz (dot-dashed curve).

tighter the tolerance, the more the number of sections required. By varying the initial dispersion coefficient (β_{20}), the decay rate of the exponentially decreasing dispersion (σ), the compression ratio (*CR*) and the initial pulse width, we have found that the number of sections required only depends on the compression factor [$CR = \exp(\sigma L_g)$] and the ratio of initial chirp length to initial dispersion length ($\varepsilon = L_C / L_{D_0} = 1/\alpha_{20}/T_0^2 = 1/C_0$, where C_0 is the initial normalized chirp value). If ε is the same for different pulses, it is obvious that the one with a larger *CR* requires more sections. If *CR* is fixed, the one with larger ε requires more sections. In Fig. 2.5(a), solid curve and dots represent $\varepsilon = 1/4$ and $\varepsilon = 1/8$ respectively. The tolerance of the pedestal energy is set to <0.5% when we implement the SWA. From Fig. 2.5(a), if the objective is to reduce the number of constant segments, then ε should be kept small but, of course, ε cannot be too small otherwise we will be in the chirp dominated regime. The chirp dominated regime is not of interest because there is no significant bandwidth broadening. Figure 2.5(b) shows the dependence of pulse bandwidth on the pulse chirp for a chirped Gaussian pulse of the form $\mathrm{A}_0 \exp\left[-(1-iC)t^2/T_0^2/2\right]$ (solid curve) and a chirped hyperbolic secant pulse of the form $\mathrm{A}_0 \operatorname{sech}(t/T_0)\exp\left(i\, Ct^2/T_0^2/2\right)$ (dashed curve). We observed that the ratio of the bandwidth of the chirped pulse to that of the unchirped pulse [$\Delta\omega(C)/\Delta\omega(0)$] increases linearly and quadratically with the chirp (C) for the hyperbolic secant pulse and Gaussian pulse, respectively. The bandwidth contributed by the chirp equals to that of an unchirped pulse occur at $|C|$ = 0.87 for the Gaussian pulse and 0.36 for the hyperbolic secant pulse. Beyond the respective chirp values, the chirp contributes more significantly to the pulse bandwidth.
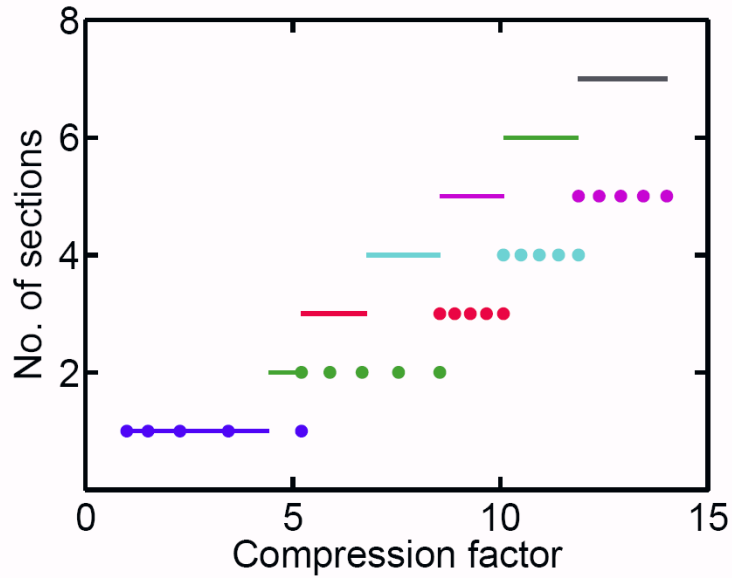
(a)
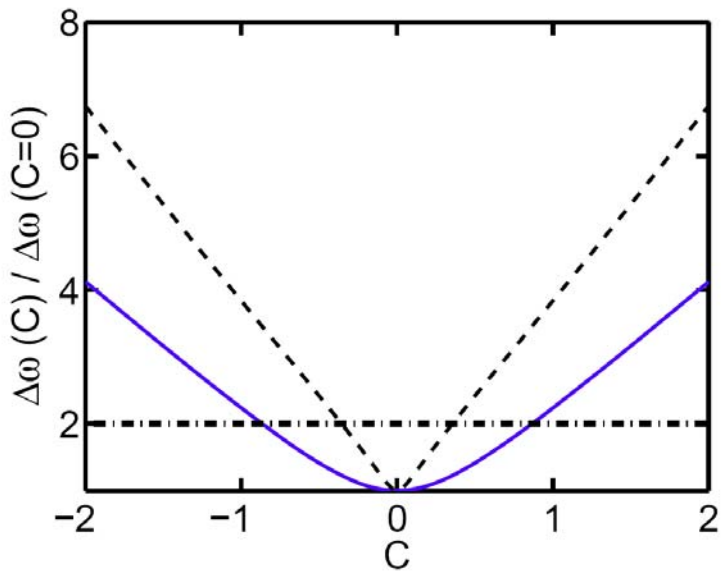
(b)

Figure 2.5: (a) Number of sections versus the compression ratio for $\varepsilon = 1/4$ (solid curve) and $\varepsilon = 1/8$ (dots). The tolerance of the pedestal energy is <0.5%. (b) Ratio of the bandwidth of chirped pulses versus that of unchirped pulses for Gaussian pulses (solid curve) and hyperbolic secant pulses (dashed curve). The dot-dashed curve represents the contribution of the chirp to the bandwidth equals to that of an unchirped pulse.

2.3 Compression of Unchirped Optical Pulses

Unlike conventional solitons of the NLS equation with constant dispersion, the solution to the NLS equation with exponential varying dispersion is chirped. The linear chirp of the solution is a key feature of the self-similar characteristics of the solution which allows pedestal-free pulse compression. However in pulse compression, typically the input pulse is unchirped although the pulse after compression is usually chirped. Thus for the proposed nonlinear pulse compression, the input pulse must be chirped in the prescribed manner before pulse compression in the nonlinear grating can take place. In general, it is not easy to produce the precise pulse shape and chirp [75]. Therefore in this section we study the compression of initially chirp-free pulse using a linear FBG to produce the required chirp profile for the compression in NFBG with exponentially decreasing dispersion. In particular, we assume that the input pulse is chirp-free hyperbolic secant pulse or Gaussian pulse. Our simulation results show that the pedestal generated from an input Gaussian pulse is much smaller than that of an input hyperbolic secant pulse showing that the compression by the NFBG is more sensitive to the chirp profile than the pulse shape. We also find that the initial Gaussian profile evolves into a hyperbolic secant profile after the compression in the NFBG.

2.3.1 Prechirping

Firstly, we study chirping of an initially chirp-free hyperbolic secant pulse of the form, $A_0 \mathrm{sech}(t/T_0)$, by using a linear FBG with normal dispersion, where A_0 is the pulse amplitude. Here a normal dispersive medium is used to introduce a negative α_{20} for the subsequent nonlinear pulse compression. Figures 2.6(a) shows the evolution of a generated pedestal with the length of the linear FBG. The pedestal energy increases with the length of the linear FBG. Figure 2.6(b)

shows the evolution of the normalized chirp $C_{\text{lin}}(z)$ in a linear FBG. The chirp value is determined by carrying out a polynomial fit of the pulse phase. We find that the higher order chirp terms are negligible. The normalized chirp $\left|C_{\text{lin}}(z)\right|$ initially increases and then decreases with the length of the linear FBG. We note that $C_{\text{lin}}(z) = \alpha_2(z)T_0^2$ and $\alpha_2(z)$ is associated with the decay rate of NFBG $\sigma = \alpha_{20}\beta_{20}$. Thus for a compact optical pulse compressor, we choose the length of the linear grating to maximize the value of $\left|\alpha_2(z)\right|$. From Fig. 2.6(b), the maximum point $\left|C_{\text{lin}}(z)\right|$ occurs at $z/L_D = 0.56$ with $C_{\text{lin}}(z) = -0.3992$.

For the chirping of an initially chirp-free Gaussian pulses of the form $A_0\exp\left(-t^2/T_0^2/2\right)$, it is well known that linear dispersive media only modify the quadratic chirp coefficient of a Gaussian shape but leave the pulse shape unchanged. The chirp coefficent α_{20} is given by $\alpha_{20} = -\beta_{2,\text{lin}}z/\left(T_0^4 + \beta_{2,\text{lin}}^2 z^2\right) < 0$ where $\beta_{2,\text{lin}}$ is the dispersion coefficient of the linear FBG [5]. Figure 2.6(c) shows the evolution of the normalized chirp $C_{\text{lin}}(z)$ in a linear grating for the Gaussian pulse. The maximum normalized chirp $\left|C_{\text{lin}}(z)\right| = 0.5$ occurs at $z = L_D = T_0^2/\beta_2$. Figure 2.6(d) shows the evolution of the broadening factor until the maximum chirp occurs. The solid curve and the dashed curve represent the broadening factor in the chirping of a hyperbolic secant and Gaussian pulse. The maximum broadening factors are 1.26 and 1.41 for hyperbolic secant and Gaussian pulse.

As an illustration, we consider the compression of a chirp-free hyperbolic secant pulse and a chirp-free Gaussian pulse with same FWHM 16.65 ps, corresponding to $T_0 = 9.45$ ps for hyperbolic secant pulse, and $T_0 = 10$ ps for Gaussian pulse. For the hyperbolic secant input pulse, the dispersion coefficient
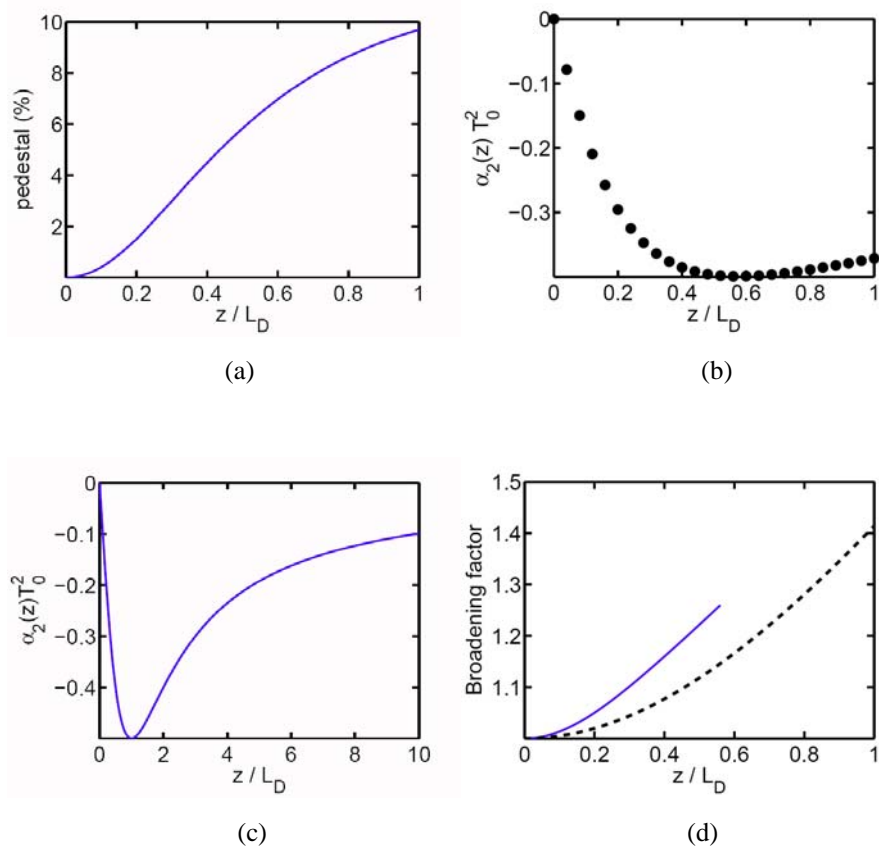
Figure 2.6: (a) Pedestal generated and (b) evolution of $\alpha_2(z)T_0^2$ in the chirping of a hyperbolic secant pulse using a linear FBG as a function of grating length. (c) The evolution of $\alpha_2(z)T_0^2$ in the chirping of a Gaussian pulse using a linear FBG versus grating length. (d) Evolution of the broadening factor until the maximum chirp occurs. The solid curve and dashed curve represent the broadening factor in the chirping of a hyperbolic secant and Gaussian pulse. The parameter L_D is the dispersion length of the linear grating.

and the length of the linear FBG are 25 ps^2/cm and 2 cm, respectively. For the Gaussian input pulse, the dispersion coefficient and the length of the linear FBG are 25 ps^2/cm and 4 cm, respectively. We use linear FBGs with same dispersion but vary the grating length to achieve maximum chirp value α_{20} in the chirping of the hyperbolic secant and Gaussian pulses. In our chosen examples, α_{20} is found to be $-0.0045\,\text{THz}^2$ for the pre-chirped quasi-hyperbolic secant pulse, and $-0.005\,\text{THz}^2$ for the pre-chirped Gaussian pulse.

2.3.2 Nonlinear Compression

Next, we launched the pre-chirped hyperbolic secant pulse, from Section 2.3.1, into the NFBG with exponentially decreasing dispersion. The power of the optical pulse input to the NFBG is chosen as $P_0 = |\beta_{20}| / \gamma_g / T_{\text{sech}}^2 (L_{LFBG})$, where $T_{\text{sech}} (L_{LFBG})$ is the pulse width parameter of the hyperbolic secant pulse used to fit the linear FBG output when the input is a hyperbolic secant pulse, and β_{20} is the initial dispersion value of the NFBG. The pulse width parameter of the pre-chirped pulse is $T_{\text{sech}} (L_{LFBG}) = 11.9\,\text{ps}$, the initial dispersion coefficient is $\beta_{20} = -25$ ps^2/cm, the decay rate of the exponentially decreasing dispersion is $\sigma = 0.1125$/cm, the nonlinear coefficient of NFBG is $\gamma_g = 15$/W/km, and the length of NFBG is 19.2 cm. Figure 2.7(a) and (b) show the initial pulse (solid curve) and pre-chirped pulse (dashed curve) in linear and logarithmic scales. We note that the chirped pulse deviates slightly from the hyperbolic secant profile. Figures 2.7(c) and (d) show the pulse profile after the NFBG (19.2 cm) in both linear and logarithmic scales. The fitted hyperbolic secant profile [dots in Fig. 2.7(c) and dashed curve in Fig. 2.7(d)] has the same peak power and FWHM as the final compressed pulse. Figure 2.7(e) shows the evolution of FWHM in the

linear FBG (the pre-chirper) and NFBG (the pulse compressor), where the dots represent self-similar soliton, the solid curve represents the simulation results of NLS equation, the dashed curve represents the results of the LVM using the hyperbolic secant pulse ansatz, and the dot-dashed curve represents the results of the POM using the hyperbolic secant ansatz. The deviation is slightly larger here because of the two reduction methods are not very accurate in determining the FWHM using the hyperbolic secant ansatz in the pre-chirping process. We note that the LVM performs slightly better than the POM. The total compression factor (compared to the initial chirp-free pulse) is 6.28, and the generated pedestal is 6.24% (Table 2.2).

Then we launched the chirped Gaussian pulse, from Section 2.3.1, into the NFBG with the exponentially decreasing dispersion. Following Ref. [62] we choose the parameters

$$T_{Gauss}^2 \left(L_{LFBG} \right) / \sqrt{2} / |\beta_{20}| = 1 / \gamma_g / P_0, \tag{2.33}$$

where $T_{Gauss} \left(L_{LFBG} \right)$ is the pulse width parameter of the pre-chirped Gaussian pulse which is achieved after the linear FBG, P_0 is the power of pulse input to the NFBG, and β_{20} is the initial dispersion value of the NFBG. In our example, $\beta_{20} = -25$ ps^2/cm, $T_{Gauss} \left(L_{LFBG} \right) = 10\sqrt{2}$ ps, $\sigma = 0.125$/cm, $\gamma_g = 15$/W/km, and the NFBG is 16 cm long. Figure 2.8(a) and (b) show the initial pulse (solid curve) and pre-chirped pulse (dashed curve) in linear and logarithmic scales. Figure 2.8(c) and (d) show the pulse profile after the NFBG (16 cm) in both linear and logarithmic scales. From Fig. 2.8(d), the main portion of the compressed pulse is almost the same as the fitted hyperbolic secant pulse, indicating the initial Gaussian profile has evolved into a hyperbolic secant profile after the

compression in the NFBG. For the compression of Gaussian pulse, we solve the pulse parameter equations using the LVM and the POM using the hyperbolic secant pulse ansatz [Eq. (2.19)] and Gaussian ansatz [Eq. (2.20)]. We assume that the pulse launched into the NFBG is chirped hyperbolic secant pulse or chirped Gaussian pulse with same FWHM. Figure 2.8(e) shows the compressed pulse. The solid curve, dashed curve, dots, and dot-dashed curve represent the results from the full simulation, the LVM with hyperbolic secant pulse ansatz, the POM with hyperbolic secant pulse ansatz, and the LVM (or POM) with Gaussian pulse ansatz, respectively. The LVM with hyperbolic secant pulse ansatz approximates the full simulations results better. Figure 2.8(f) shows the evolution of the FWHM in the linear FBG and NFBG. The solid curve, dashed curve, dot-dashed curve and dots represent the results from the full simulation, the LVM with hyperbolic secant pulse ansatz, the POM with hyperbolic secant pulse ansatz, and the LVM (or POM) with Gaussian pulse ansatz, respectively. Results from both the reduction methods using either ansatz are all very close. The total compression ratio when compared to the initial chirp-free pulse is 6.28 and the generated pedestal is 0.0935% (Table 2.2).

As shown in Table 2.2, the final compressed pulse of the initial hyperbolic secant and Gaussian pulse have the same FWHM (2.65 ps). The final compressed pulses are almost chirp-free. We observe that the pedestal generated from an input Gaussian pulse is much smaller than that of an input hyperbolic secant pulse. By varying β_{20}, α_{20}, and T_0, we find that the compression ratio mainly depends on the designed value of CR, and the generated pedestal is associated with both designed CR and ε discussed before.

In the compression of initial Gaussian pulses, we use Eq. (2.33) to determine
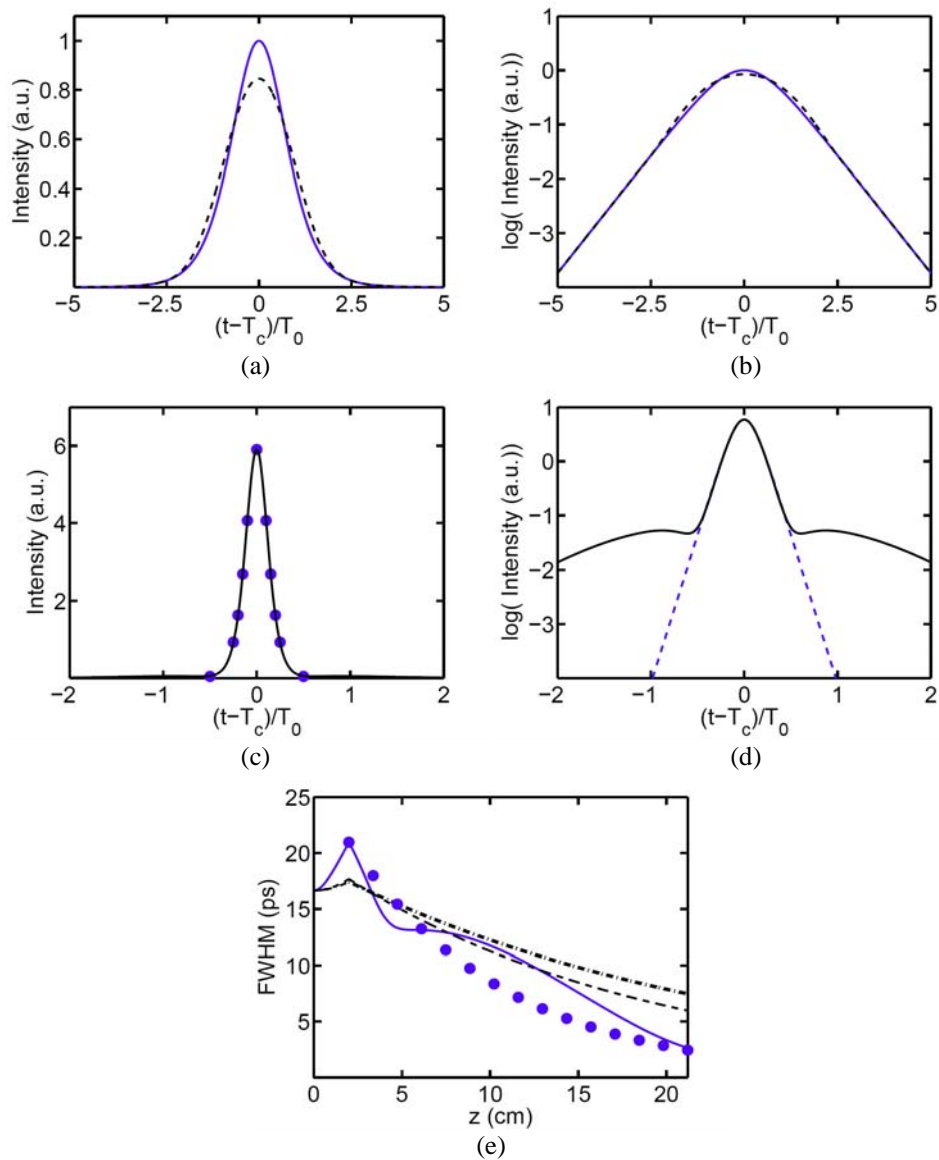
Figure 2.7: Hyperbolic secant input pulse. The pulse profiles before (solid curve) and after the linear FBG (dashed curve) in (a) linear and (b) logarithmic scales. The pulse profiles after the NFBG (solid curve) and a "fitted" hyperbolic secant pulse profiles in (c) linear (dots) and (d) logarithmic scales (dashed curve). (e) Evolution of the FWHM in the pre-chirper (the linear FBG) and the NFBG for the self-similar soliton (dots), the full numerical simulation (solid curve), the LVM using hyperbolic secant pulse ansatz (dashed curve), and the POM using hyperbolic secant pulse ansatz (dot-dashed curve).
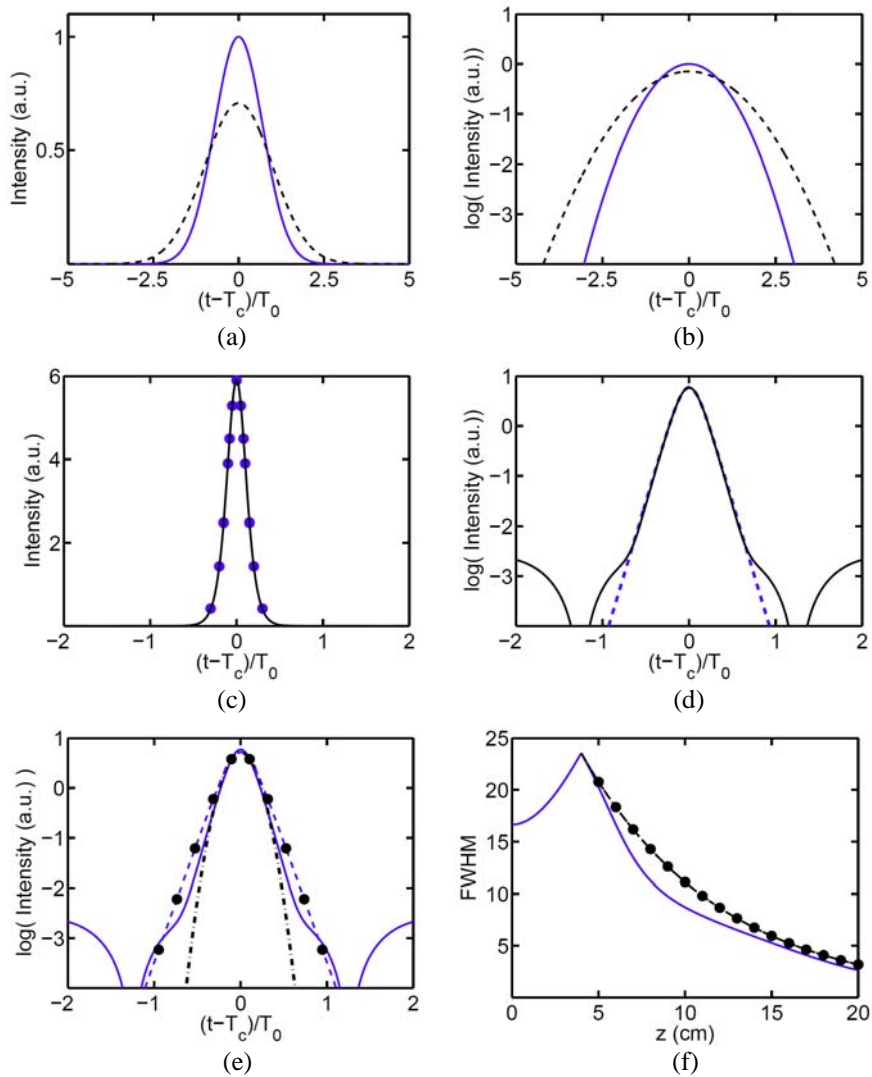
Figure 2.8: Gaussian input pulse. The pulse profiles before (solid curve) and after the linear FBG (dashed curve) in (a) linear and (b) logarithmic scales. The pulse profiles after the NFBG (solid curve) and a "fitted" hyperbolic secant pulse profiles in (c) linear (dots) and (d) logarithmic scales (dashed curve). (e) The compressed pulse in logarithmic scale. (f) Evolution of the FWHM in pre-chirper (linear FBG) and the NFBG. For (e) and (f), the solid curve, dashed curve, dots, and dot-dashed curve represent the full numerical simulation, the LVM with hyperbolic secant pulse ansatz, the POM with hyperbolic secant pulse ansatz, and the LVM or POM with Gaussian ansatz, respectively.

54
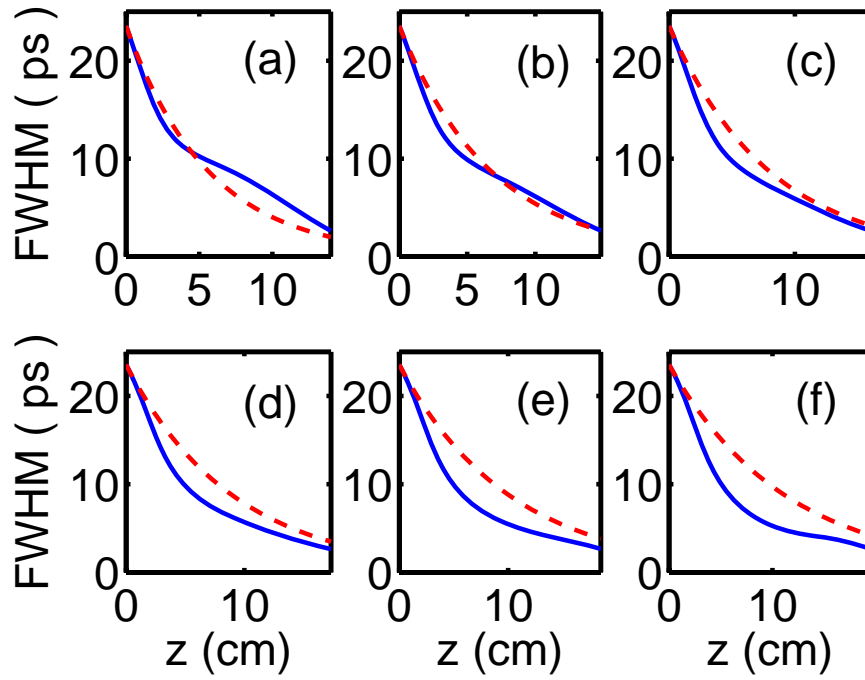
Figure 2.9: Evolution of the FWHM versus distance for different values of the ratio $L_{D0,\text{Gauss}}/$ $L_{N0,\text{Gauss}}$. The dashed curve represents self-similar solitons, and the solid curve represents simulation results. The values of ratio $L_{D0,\text{Gauss}}/L_{N0,\text{Gauss}}$ from (a) to (f) are 1, 1.2, $\sqrt{2}$, 1.6, 1.8 and 2, respectively.

the NFBG parameters. We find that the design gives good quality compressed pulses. We want to determine whether Eq. (2.33) gives the optimal design parameters for the NFBG. We define the ratio $= L_{D0,\text{Gauss}} / L_{N0,\text{Gauss}}$, where $L_{D0,\text{Gauss}} = T_{\text{Gauss}}^2 (L_{LFBG}) / |\beta_{20}|$ and $L_{N0,\text{Gauss}} = 1/\gamma_g / P_0$ are the initial dispersion length and initial nonlinear length of the Gaussian pulse input into the NFBG. We obtain different ratios of $L_{D0,\text{Gauss}} / L_{N0,\text{Gauss}}$ by either changing the initial dispersion value of the NFBG (β_{20}) or changing the peak power of the initial pulse. Different lengths of NFBG are used to achieve the same FWHM of the final compressed pulse. Table 2.3 gives the percentages of pedestals generated. We observe that the amount of pedestal generated mainly depends on the ratio $L_{D0,\text{Gauss}} / L_{N0,\text{Gauss}}$ and the optimal point is $L_{D0,\text{Gauss}} / L_{N0,\text{Gauss}} = \sqrt{2}$. Figure 2.9 shows the evolution of the pulse width (FWHM) with respect to the change in the ratio $L_{D0,\text{Gauss}} / L_{N0,\text{Gauss}}$. Thus Eq. (2.33) is a good and simple criterion to design the NFBG for compression of Gaussian pulses.

2.3.3 Stepwise Approximation

Finally, we consider the SWA of the NFBG used in the compression of an initial hyperbolic secant pulse discussed in Section 2.3.1. Figure 2.10(a) and (b) respectively show the change of FWHM and percentage of pedestal generated of the final compressed pulse with respect to number of sections used. The dots represent the FWHM or the pedestal generated versus the number of sections used, and the circle represents that by using DDFBG. When the number of section increases, the compressed pulse from the SWA becomes closer to that by using DDFBG. Figure 2.10(c) shows the evolution of the FWHM in the compression

Table 2.2: Comparison between the compression of hyperbolic secant input pulse and Gaussian input pulse. $C(0)$ is the normalized chirp coefficient of the chirped hyperbolic secant or Gaussian input pulse. The normalized chirp coefficient after the linear FBG, $C(0)$, is determined by fitting the phase of the pulse using $C(0)t^2/T^2(L_{LFBG})/2$, where $T(L_{LFBG})$ is the pulse width parameter of the hyperbolic secant or Gaussian pulse. Similarly, the chirp coefficient of compressed pulse, $C(z)$, is determined by fitting the phase of the pulse using $C(z)t^2/T^2(L_{NFBG})/2$, where $T(L_{NFBG})$ is the pulse width parameter of compressed pulse.

	Compression of "sech" input pulse (Figure 2.7)	Compression of Gaussian input pulse (Figure 2.8)
$C(0)$	− 0.63	− 1
$C(z)$	− 0.16	−0.097
FWHM of compressed pulse	2.65 ps	2.65 ps
Pedestal of compressed pulse	6.24%	0.0935%

Table 2.3: Comparison of the pedestal generated for different values of the ratio=$L_{D0,\text{Gauss}}$ / $L_{N0,\text{Gauss}}$, where $L_{D0,\text{Gauss}} = T^2_{\text{Gauss}} (L_{LFBG})/|\beta_{20}|$ and $L_{N0,\text{Gauss}} = 1 / \gamma_g / P_0$ and are the initial dispersion length and the nonlinear length, respectively. The different values of $L_{D0,\text{Gauss}}$ / $L_{N0,\text{Gauss}}$ are obtained by either changing the initial dispersion value of NFBG β_{20} or changing the peak power of the initial pulse. Different lengths of NFBG are used to achieve the same FWHM of the final compressed pulse.

Ratio	Change of β_{20}	Change of peak power
1	6.49%	6.49%
1.2	1.47%	1.47%
$2^{0.5}$	0.0935%	
1.6	1%	1%
1.8	2.42%	2.38%
2	3.69%	3.68%

process, where the solid curve represents the full simulation of DDFBG, the dots represent the full simulation using 8-section SWA, the dashed curve represents the results of the LVM using hyperbolic secant pulse ansatz and 8-section SWA, and the dot-dashed curve represents the results of the POM using hyperbolic secant pulse ansatz and 8-section SWA. We observe that results from the LVM and POM using the hyperbolic secant pulse ansatz are very close to each other.

Next, we consider the SWA of the NFBG used in the compression of an initial Gaussian pulse discussed in the Section 2.3.1. Figures 2.11(a) and (b) respectively show the change of the FWHM and the percentage of pedestal generated from the final compressed pulse versus the number of sections used. The dots represent the FWHM or the pedestal generated using different number of sections, and the circle represents that by using DDFBG. Again when the number of section increases, the compressed pulse from the SWA becomes closer to that achieved in the DDFBG. Figure 2.11(c) shows the evolution of the FWHM in the 8-section SWA and DDFBG. In this case, eight FBGs with constant dispersions can approximate the exponentially decreasing dispersion profile very well. Finally Fig. 2.11(d) compares the results from the full simulation, the LVM and POM with hyperbolic secant pulse ansatz and Gaussian pulse ansatz. The dots represent full simulation of the 8-section SWA, the dashed curve represents the results of the LVM with hyperbolic secant pulse ansatz and 8-section SWA, the dot-dashed curve represents the results of the POM with hyperbolic secant pulse ansatz and 8-section SWA, and the solid curve represents the result of the LVM or POM with Gaussian pulse ansatz and 8-section SWA. The results from the two reduction methods with different ansatz are similar and deviate slightly from that of full simulations.

2.4 Summary

We have shown that self-similar chirped Bragg soliton solutions for the NLS equation exist for exponentially varying dispersion. The evolution of the pulse width follows that of the exponentially varying dispersion. Thus, nonlinear fiber Bragg gratings with exponentially decreasing dispersion can be used to carry out pedestal free compression of optical pulses. Unlike the solitons of the NLS equation with constant dispersion, these self-similar solitons are chirped. The chirped soliton evolves such that the dispersion length equals to the nonlinear length. Both the dispersion length and the nonlinear length vary with distance, but the chirp length is constant. As a result, if the ratio of the initial chirp length to the dispersion length is small, the characteristics of the pulse evolution will change from initially quasi-linear in the beginning of the grating, to a combination of linear and nonlinear for intermediate portion of the grating, to finally fully nonlinear towards the end of the grating.

We have also shown that the exponentially varying dispersion of the nonlinear fiber Bragg gratings can be approximated by using a concatenation of nonlinear fiber Bragg gratings with different constant dispersions. For a given tolerance on the pedestal generated, we have found that the number of concatenated sections is proportional to the compression ratio, but inversely proportional to the initial chirp value. We have also studied the effect of pre-chirping using linear fiber Bragg grating to produce the required chirp profile for initially chirp-free hyperbolic secant and Gaussian pulse. We have found that the pedestal generated from an input Gaussian pulse is much smaller than that of a hyperbolic secant pulse showing that the compression by the nonlinear fiber Bragg grating is more sensitive to the chirp profile than the pulse shape. We have also found that the

initial Gaussian profile evolves into a hyperbolic secant profile after the compression in the nonlinear fiber Bragg grating. Finally, we study the use of stepwise approximation to the exponentially decreasing dispersion on initial hyperbolic secant and Gaussian pulses chirped by a linear fiber Bragg grating. We have found that high quality compressed pulses can be generated.

In this study, based on NLS-type equation, we consider the pulse propagation close to the PBG structure of FBG. We will include the results using full nonlinear coupled-mode equations which include all orders of dispersion in Chapter 3.

(a)

(b)

(c)
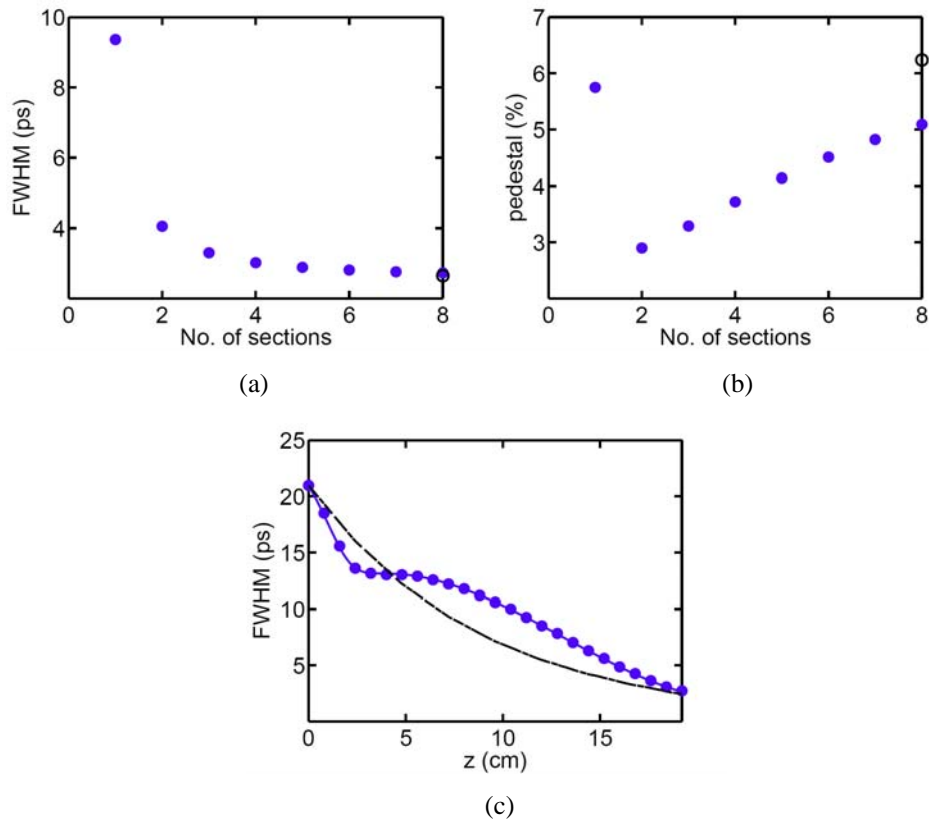
Figure 2.10: Hyperbolic secant input pulse and SWA to the exponentially decreasing dispersion. (a) The FWHM and (b) pedestal of final compressed pulse using 1 to 8 sections for SWA (dots) and DDFBG (circle). (c) Evolution of the FWHM in the DDFBG (solid curve), the 8-section SWA using the full simulation (dots), the LVM with hyperbolic secant pulse ansatz and 8-section SWA (dashed curve), and the POM with hyperbolic secant pulse ansatz and 8-section SWA (dot-dashed curve).
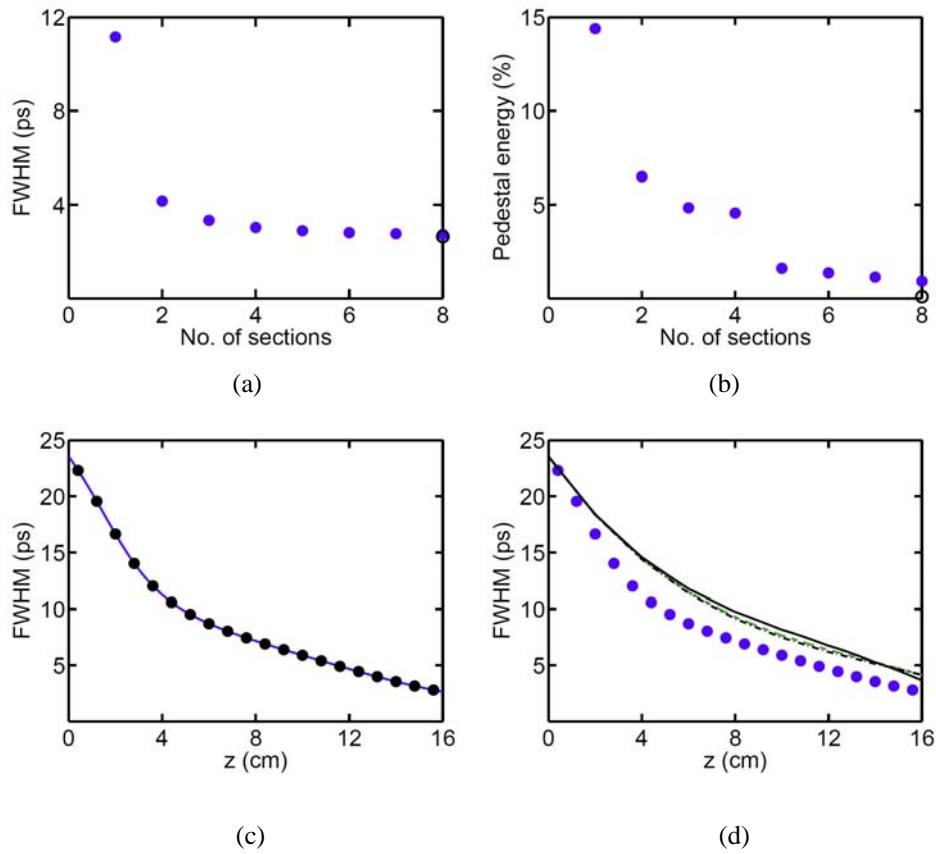
Figure 2.11: Gaussian input pulse and SWA to the exponentially decreasing dispersion. (a) Evolution of the (a) FWHM and (b) pedestal of the final compressed pulse using 1 to 8 sections for SWA (dots) and DDFBG (circle). (c) Evolution of the FWHM in DDFBG (solid curve) and 8-section SWA using full numerical simulation (dots). (d) Evolution of FWHM for the full numerical simulation on 8-section SWA (dots), the LVM with hyperbolic secant pulse ansatz and 8-section SWA (dashed curve), the POM with hyperbolic secant pulse ansatz and 8-section SWA (dot-dashed curve), and Gaussian pulse ansatz and 8-section SWA (solid curve).

Chapter 3

Pulse Compression in Nonlinear Fiber Bragg Gratings and Nonlinear Coupled Mode Equations

In Chapter 2, we have discussed nearly chirp-free and pedestal-free optical pulse compression in nonlinear fiber Bragg gratings with exponentially decreasing dispersion in the nonlinear Schrödinger limit. The nonlinear Schrödinger equation used in Chapter 2 only considers the second order dispersion effect. The generalized nonlinear coupled mode equations, which include all orders of dispersions, are more accurate in describing pulse propagation in nonlinear gratings. In this chapter, we present numerical simulation results of the generalized nonlinear coupled mode equations.

3.1 Introduction

The NLS model used in Chapter 2 only includes the second order dispersion (β_2).

While β_2 is exponentially decreasing, the profile of the third order dispersion (β_3)

has not been studied in Chapter 2. Normally the second order dispersion length

(L_D) and the third order dispersion length (L_D') are used to compare the relative

importance of the second order and third order dispersion. For the self-similar

pulse compression discussed in Chapter 2, both the pulse width parameter $T(z)$

and second order dispersion β_2 decrease exponentially at the same rate, therefore

the second dispersion length L_D ($= T^2(z)/|\beta_2|$) also decreases exponentially.

However, if the third order dispersion is present, the third order dispersion length

L_D' ($= T^3(z)/|\beta_3|$) will decrease much faster compared to L_D if β_3 is a constant.

In this Chapter, the nonlinear coupled mode equations (NLCMEs), which include

all orders of dispersions, are used here to have a full study of the grating based

compressor. We compare the results of the NLCMEs with the nonlinear

schrödinger equation (NLSE) approximation. We define a figure of merit for the

optimization of the grating parameters to generate compressed pulse with good

quality. The exponential dispersion profile of the grating is also well

approximated by a number of gratings with constant dispersions. The chapter is

arranged as follows. Section 3.2 introduces the theoretical models which describe

the pulse propagation in NFBGs. Section 3.3 discusses the compression of

chirped hyperbolic secant pulse and chirped Gaussian pulse in NFBGs with

exponentially decreasing dispersion and their stepwise approximation.   In

particular, we discuss the effect of initial chirp, dispersion and pulse width on

compression of chirped hyperbolic secant pulse in Section 3.4. Section 3.5

presents a compact compression scheme which consists of a pre-chirper and a NFBG, to effectively compress both the hyperbolic secant and Gaussian shaped pulses. Section 3.6 provides a study on the minimum pulse width that can be achieved by the proposed compressor. Some conclusions are offered in Section 3.7.

3.2 Theoretical Model

Nonlinear pulse propagation in FBGs can be described by the NLCMEs which describe the coupling between the forward-propagating wave (u) and backward-propagating wave (v) [6].

$$i\frac{\partial u}{\partial z} + i\beta_1\frac{\partial u}{\partial t} + \delta u + \kappa v + \gamma(|u|^2 + 2|v|^2)u = 0,$$
$$-i\frac{\partial v}{\partial z} + i\beta_1\frac{\partial v}{\partial t} + \delta v + \kappa u + \gamma(|v|^2 + 2|u|^2)v = 0,$$

(3.1)

where β_1 is the group delay per unit length, $\delta = n(\omega_c - \omega_B)/c$ (center wavelength is 1.55 μm in this work) is the frequency detuning from the Bragg frequency ω_B ($n\cdot\omega_B/c = \pi/\Lambda$), with c being the speed of light in vacuum, n being the average refractive index, Λ being the period of FBG. $\kappa = \eta\cdot\Delta n\cdot\pi/\Lambda/n/2$ is the coupling coefficient, with η ($\eta = 0.8$ is used in this work) being the fraction of the fiber mode that overlaps with the grating, and Δn being the refractive-index modulation. The parameter γ is the nonlinear coefficient, z is the distance, and t is the time. NLCMEs can be reduced to the well-known NLSE [Eq. (3.2)] provided two conditions are met [6]. The first condition requires $\gamma P_0 \ll \kappa$ or $\kappa L_N \gg 1$, where L_N is the nonlinear length. This requirement is easy to satisfy in practice even at peak power levels as high as 100 GW/cm^2. Second, the third-order dispersion induced by grating should be negligible.

$$i\frac{\partial E}{\partial z} - \frac{\beta_2(z)}{2}\frac{\partial^2 E}{\partial t^2} + \gamma_g |E|^2 E = 0. \tag{3.2}$$

A fiber grating operating in the passband but close to the stop band acts as a highly dispersive element with a second order dispersion (β_2) and third order dispersion (β_3) given by [6]

$$\beta_2 = \frac{-\text{sgn}(\delta)\kappa^2\beta_1^2}{(\delta^2 - \kappa^2)^{3/2}}, \tag{3.3}$$

$$\beta_3 = \frac{3|\delta|\kappa^2\beta_1^3}{(\delta^2 - \kappa^2)^{5/2}}. \tag{3.4}$$

The connection between γ in the NLCMEs [Eq. (3.1)] and γ_g in NLSE [Eq. (3.2)] is

$$\gamma_g = \frac{3 - f^2}{2f}\gamma, \tag{3.5}$$

$$f = \pm\sqrt{1 - \kappa^2/\delta^2}. \tag{3.6}$$

We consider that the second order dispersion decreases exponentially, i.e. $\beta_2(z) = \beta_{20}\exp(-\sigma z)$, where β_{20} is the initial second order dispersion of the NFBG. We also assume that nonlinear coefficient is constant and $\delta(z) = b\kappa(z)$. The detuning has to be positive ($\delta > \kappa$) to yield anomalous dispersion and soliton effects. Therefore,

$$\kappa(z) = -\beta_1^2\exp(\sigma z)/(b^2 - 1)^{3/2}/\beta_{20}. \tag{3.7}$$

Then different order dispersion is found to be

$$\beta_m \sim \exp\left[-(m-1)\sigma z\right], \qquad m \geq 3. \tag{3.8}$$

If the pulse width parameter decreases exponentially as $T(z) = T_0\exp(-\sigma z)$, the different order dispersion length is

$$L_{D_m} = T^m(z)/|\beta_m| \sim \exp(\sigma z).$$ (3.9)

Consequently, we have

$$L_{D_m}/L_{D_2} = C_m, \quad m \geq 3.$$ (3.10)

Eq. (3.10) is a very important result, which implies the relative importance of different order dispersions keeps unchanged in the whole compression process.

Similar to [76], we define a figure of merit (M) to quantify the relative importance of the second order and third order dispersions. M is defined to be the ratio of L_{D_2} to L_{D_3}. For optimum pulse compression, M should be as small as possible.

$$M = \frac{L_{D_2}}{L_{D_3}} = \frac{T(z)^2/|\beta_2(z)|}{T(z)^3/|\beta_3(z)|} = \frac{3|\beta_{20}|b\sqrt{b^2-1}}{T_0\beta_1}.$$ (3.11)

We note that the value of M is proportional to $|\beta_{20}|$ and b, but inversely proportional to the initial pulse width parameter T_0.

Our designed compressor works in the transmission region, therefore we need to make sure the pulse spectrum does not overlap the reflection spectrum of the grating. For a chirped Gaussian pulse of the form $\exp(-\frac{1+iC}{2}\frac{t^2}{T_0^2})$, the bandwidth (FWHM) is given by $\Delta\omega = 2\sqrt{(1+C^2)\ln 2}/T_0$. In order to avoid the pulse spectrum falling into the stop band, we have to ensure that half of the spectral bandwidth must be smaller than the spectral distance from the band edge $(|\delta| = \kappa)$ [77]:

$$|\delta(z)| - \kappa(z) > \frac{n}{c}\sqrt{[1+C^2(z)]\ln 2}/[T_0\exp(-\sigma z)].$$ (3.12)

For the self-similar pulse considered here, $C(z) = C_0\exp(-\sigma z)$, we have

$$\left(b+1\right)\sqrt{b^2-1} < \frac{\beta_1 T_0}{\left|\beta_{20}\right|\sqrt{\left(1+C_0^2\right)\ln 2}}. \tag{3.13}$$

Another constraint is imposed by the grating modulation depth Δn, which can be as large as 0.01 in H_2 loaded fibers [36], and Δn is associated with κ. Therefore,

$$\kappa\left(z\right) = \frac{\beta_1^2 \exp\left(\sigma z\right)}{\left(b^2-1\right)^{3/2}\left|\beta_{20}\right|} \leq \frac{\eta 0.01\pi}{2\Lambda n}. \tag{3.14}$$

Typically, $\eta \sim 0.8, \Lambda \sim 0.5\ \mu m, n \sim 1.5$ [36].

3.3 Compression of Chirped Optical Pulses

3.3.1 Numerical Examples

The NLCMEs are solved by the implicit 4th-order Runge-Kutta method [53]. For the finite length L considered here, $v\left(L,t\right) = 0$. In addition, we assume that the system initially contains no energy, i.e. $u(z,0) = 0$ and $v(z,0) = 0$. The initial pulse is chirped hyperbolic secant pulse of the form $u(0,t) = \sqrt{P_0}\,\mathrm{sec}\,h(t/T_0)\exp(i\alpha_{20}t^2/2)$, where the initial pulse width parameter $T_0 = 10$ ps (FWHM = 17.63 ps) and the initial chirp $\alpha_{20} = -0.005\ \mathrm{THz}^2$, or, chirped Gaussian pulse of the form $\sqrt{P_0}\exp(-t^2/T_0^2/2)\exp(i\alpha_{20}t^2/2)$, where $T_0 = 10.586$ ps (FWHM = 17.63 ps) and $\alpha_{20} = -0.005\ \mathrm{THz}^2$. For the launched hyperbolic secant pulse, $T_0^2/\left|\beta_{20}\right| = 1/\gamma_g/P_0$, where P_0 is the peak power of the launched pulse. For the launched Gaussian pulse, $T_0^2/\sqrt{2}/\left|\beta_{20}\right| = 1/\gamma_g/P_0$, where P_0 is the peak power of the launched pulse. The grating parameters are $\beta_{20} = -25\ \mathrm{ps}^2/\mathrm{cm},\ \sigma = 0.125\ /\mathrm{cm},\ b = 2,\ \gamma = 5\ /\mathrm{W/km},$ and $L = 16$ cm. Figure 3.1 discusses the compression of chirped hyperbolic secant pulse. Figure 3.1(a) depicts the launched pulse $u(z = 0,t)$, the transmitted pulse $u(L,t)$, and Fig. 3.1(b)

shows the reflected pulse $v(z=0,t)$. Most of the light is transmitted through while a small amount is reflected back. The transmitted pulse experiences effective compression, and the FWHM of the compressed pulse is 2.3 ps. Figure 3.1(c) shows the compressed pulse shapes in logarithmic scale. The solid curve, dashed curve, and dot-dashed curve represent the results using the NLCMEs, NLSE with β_3, and NLSE without β_3, respectively. The three results are relatively similar, and small amount of pedestal is due to the presence of higher order dispersions. The calculation of pedestal follows the method described in Ref. [73]. Table 3.1 gives the comparison (FWHM, compression factor, normalized chirp, pedestal) between the results from three models (NLCMEs, NLSE with β_3, NLSE without β_3). The normalized chirp $C(z=L)$ has been greatly reduced, when compared to the initial normalized chirp $C(z=0)$, indicating the compressed pulse is almost chirp-free. From the comparison shown in Table 3.1, the results of NLCMEs are closer to the results of NLSE without β_3. Figure 3.2 discusses the compression of chirped Gaussian pulse. Figure 3.2(a) depicts the launched pulse $u(z=0,t)$, the transmitted pulse $u(L,t)$, and Fig. 3.2(b) shows the reflected pulse $v(z=0,t)$. Similarly, most of the light is transmitted through while a small amount is reflected back. Figure 3.2(c) shows the compressed pulse shapes (solid curve: NLCMEs; dashed curve: NLSE with β_3; dot-dashed curve: NLSE without β_3) in logarithmic scale. It is obvious that the initial Gaussian pulse has evolved into a hyperbolic secant profile. Table 3.2 gives the comparison (FWHM, compression factor, normalized chirp, pedestal) between results from three models (NLCMEs, NLSE with β_3, NLSE without β_3). The results of NLCMEs are closer to the results of NLSE without β_3.

Until now, we have discussed the compression of chirped hyperbolic secant pulse and Gaussian shaped pulses in the same NFBG with exponentially decreasing dispersion. The initial chirped hyperbolic secant and Gaussian pulses are assumed to have same FWHM, and the compressed pulses have similar compression factor, residual chirp, and pedestal.

3.3.2 Design of Grating

In order to vary the dispersion along the propagation direction, we can vary the period of grating Λ, the average effective index n, or the grating modulation depth Δn [50]. Varying the period or the average index will mainly vary δ, and varying Δn will only vary κ. Figures 3.3 and 3.4 give two possible structures to achieve exponentially decreasing dispersion of the NFBG in Section 3.3.1. The design shown in Fig. 3.4 is relatively easier to fabricate, because of the difficulty in the precise control of Λ in Fig. 3.3. Figure 3.5 gives the corresponding profiles of coupling coefficient and frequency detuning under the design in either Fig. 3.3 or Fig. 3.4.

3.3.3 Stepwise Approximation

Similar to Section 2.2, in this section, we study the feasibility of using the stepwise constant function to approximate to the exponentially decreasing dispersion profile, but using the NLCMEs.

Figure 3.6 and Fig. 3.7 give 8-section approximation of Fig. 3.3 and Fig. 3.4, respectively. The designs in Fig. 3.6 and Fig. 3.7 are easier to be fabricated compared to those in Fig. 3.3 and Fig. 3.4. Figure 3.8 gives the profiles of coupling coefficient and frequency detuning which correspond to the designs in Fig. 3.6 and Fig. 3.7. For the compression of chirped hyperbolic secant pulse, Fig. 3.1(d) shows the 8-section SWA of Fig. 3.1(c), where the solid curve and dashed
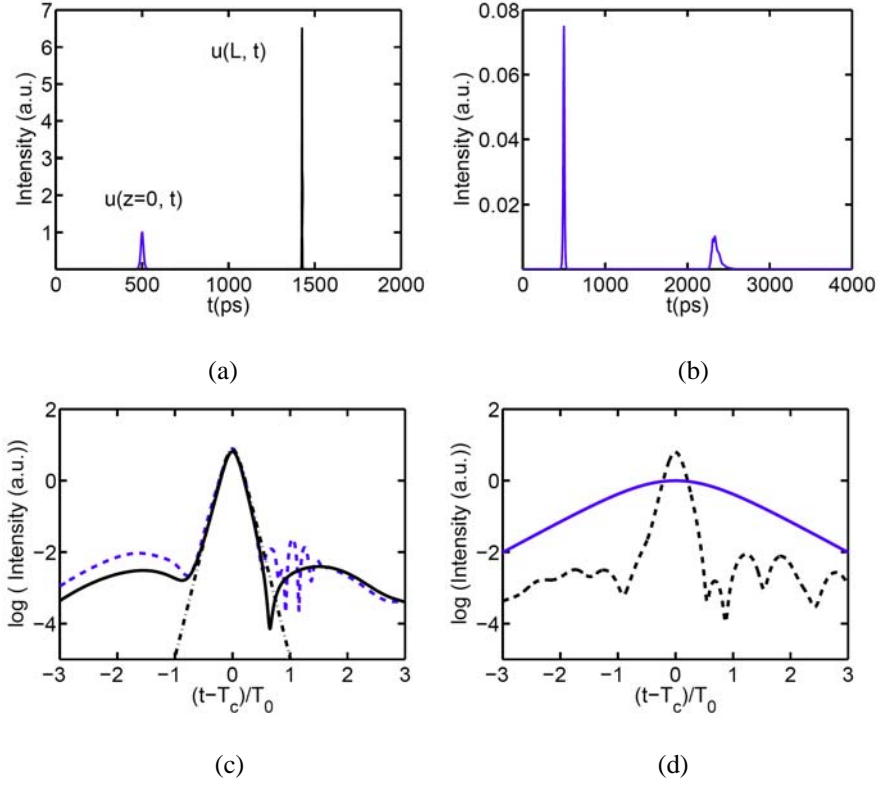
Figure 3.1: Chirped hyperbolic secant pulse is the initial pulse. (a) Launched pulse $u(z=0,t)$ and transmitted pulse $u(L,t)$. (b) Reflected pulse $v(z=0,t)$. (c) Transmitted pulse (solid curve: NLCMEs; dashed curve: NLSE with β_3; dot-dashed curve: NLSE without β_3) in logarithmic scale. (d) Initial (solid curve) and transmitted pulse (dashed curve) in 8-section SWA. Discussion on Fig. 3.1 (d) will be offered in Section 3.3.3. The grating parameters are $\beta_{20} = -25$ ps^2/cm, $\sigma = 0.125$ /cm, $b = 2$, $\gamma = 5$ /W/km, and $L = 16$ cm.
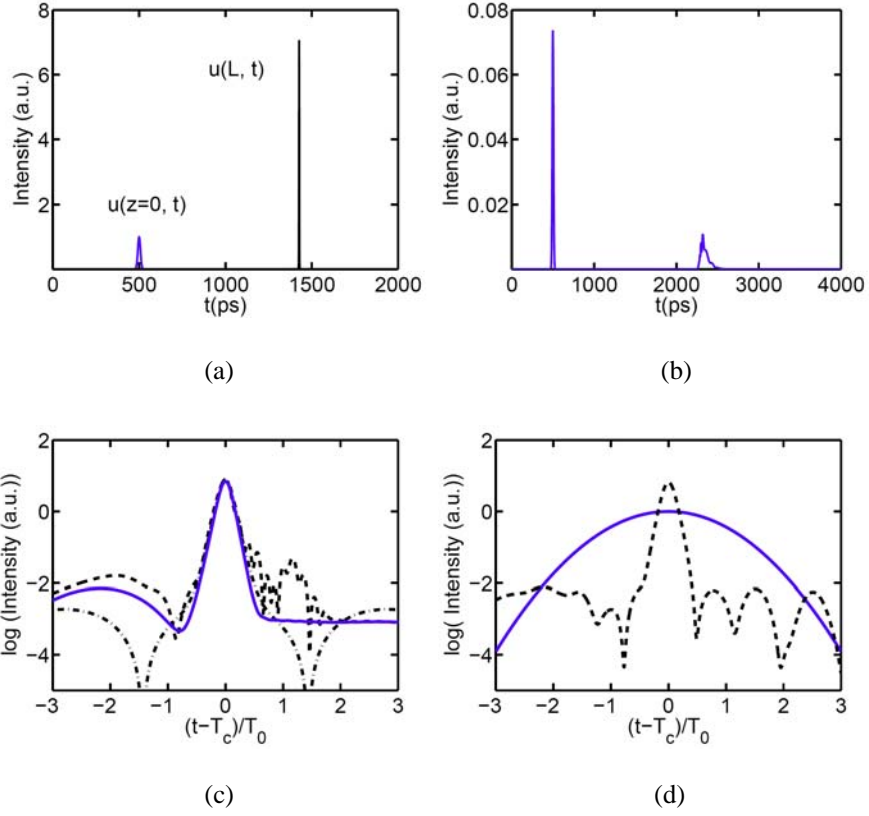
Figure 3.2: Chirped Gaussian pulse is the initial pulse. (a) Launched pulse $u(z=0,t)$ and transmitted pulse $u(L,t)$. (b) Reflected pulse $v(z=0,t)$. (c) Initial pulse (dots) and transmitted pulse (solid curve: NLCMEs; dashed curve: NLSE with β_3; dot-dashed curve: NLSE without β_3) in logarithmic scale. (d) Initial pulse (solid curve) and compressed pulse (dashed curve) in 8-section SWA. Discussion on Fig. 3.2(d) will be offered in Section 3.3.3. The grating parameters are $\beta_{20} = -25$ ps^2/cm, $\sigma = 0.125$ /cm, $b = 2$, $\gamma = 5$ /W/km, and $L = 16$ cm.
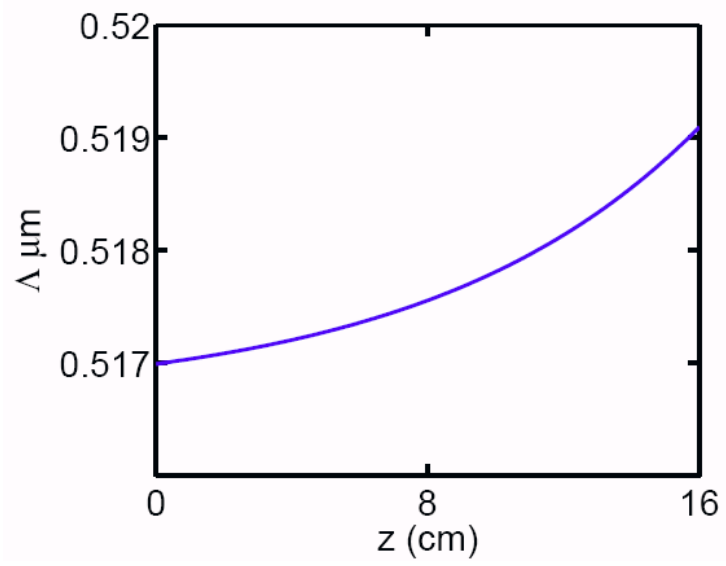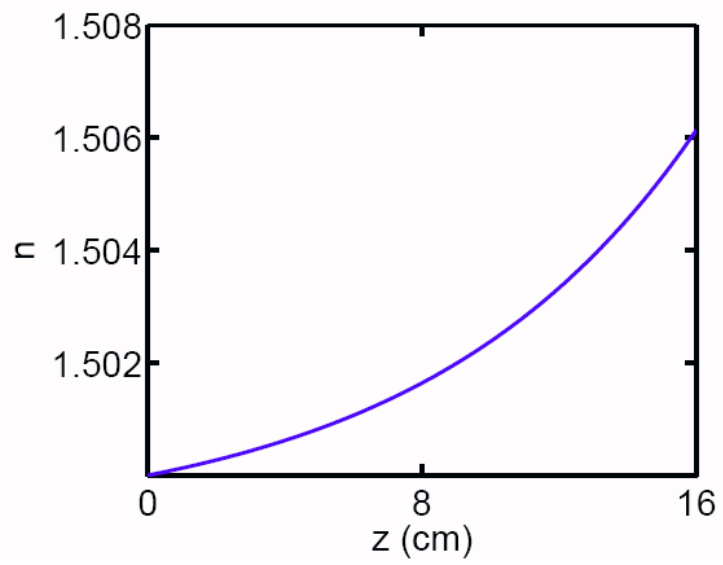
(a)
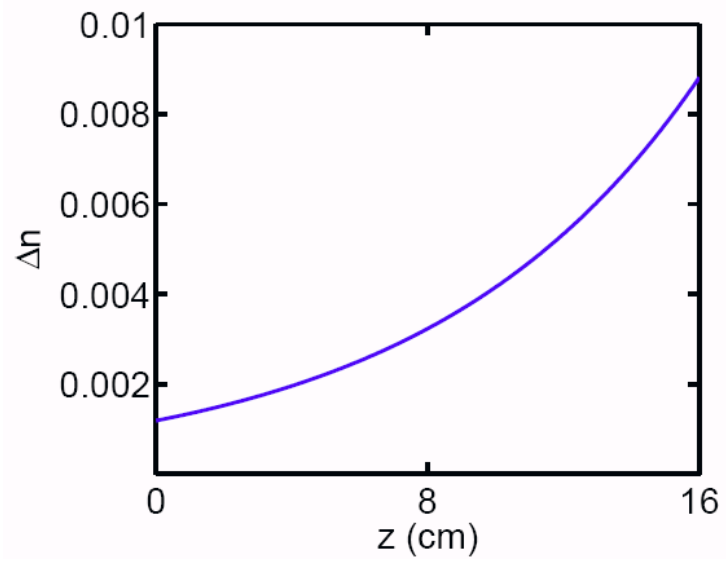
(b)

Figure 3.3: Grating design I.

(a)
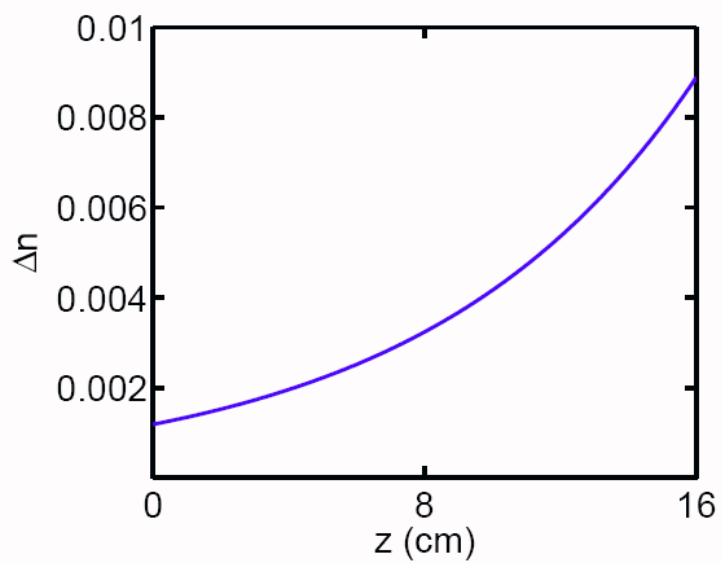
(b)

Figure 3.4: Grating design Π.
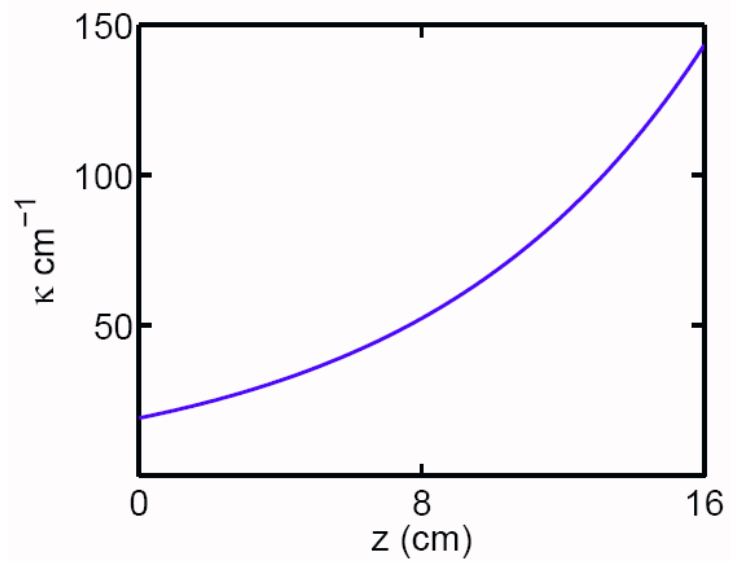
(a)
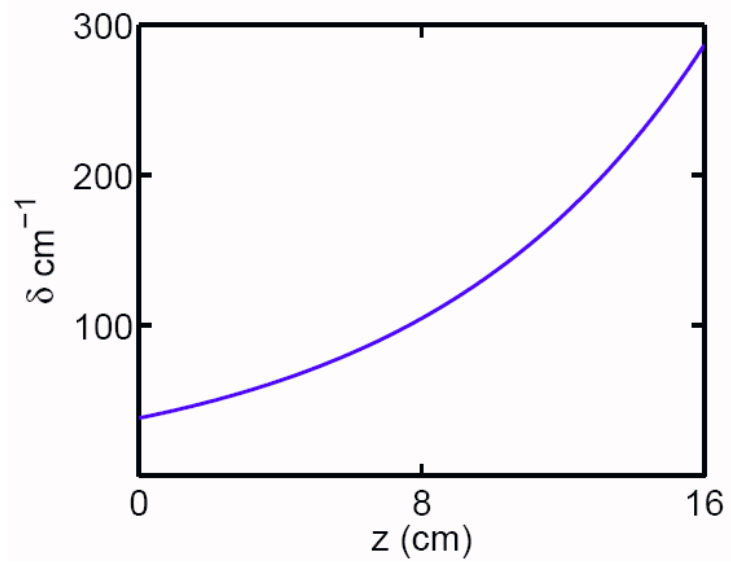
(b)

Figure 3.5: Profiles of (a) coupling coefficient and (b) frequency detuning.
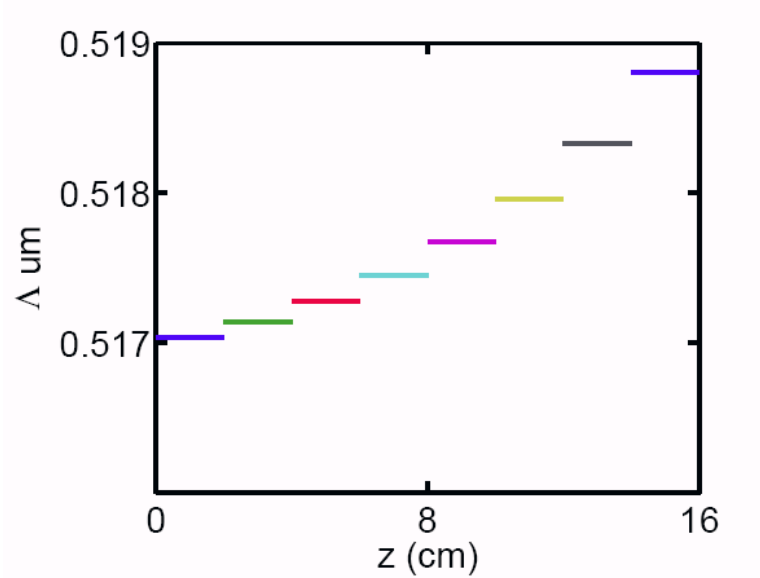
(a)
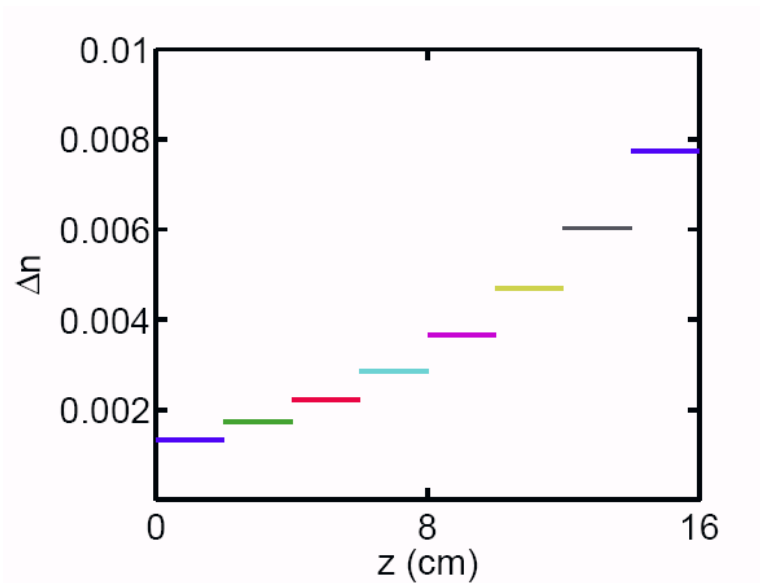
(b)

Figure 3.6: Grating design Π
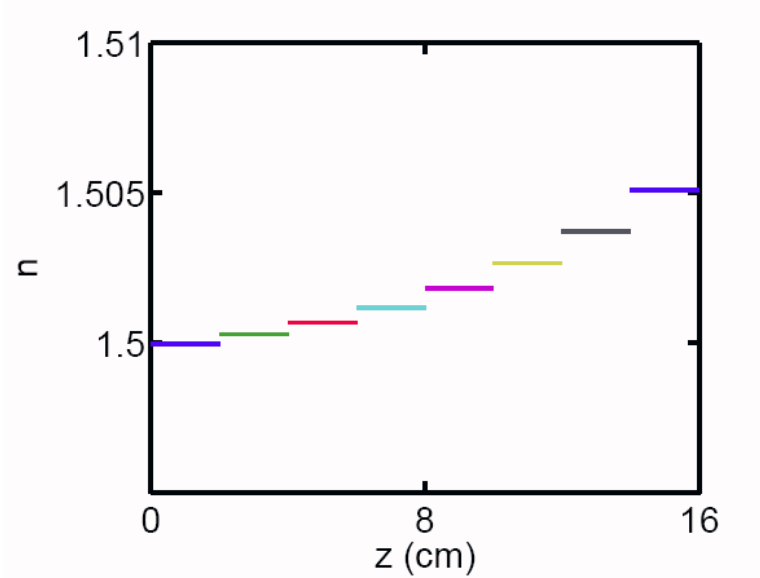
(a)
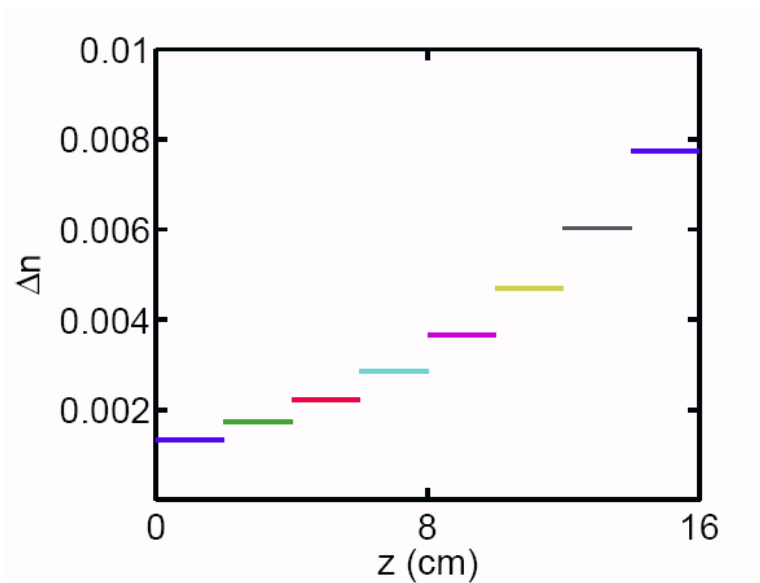
(b)

Figure 3.7: Grating design I
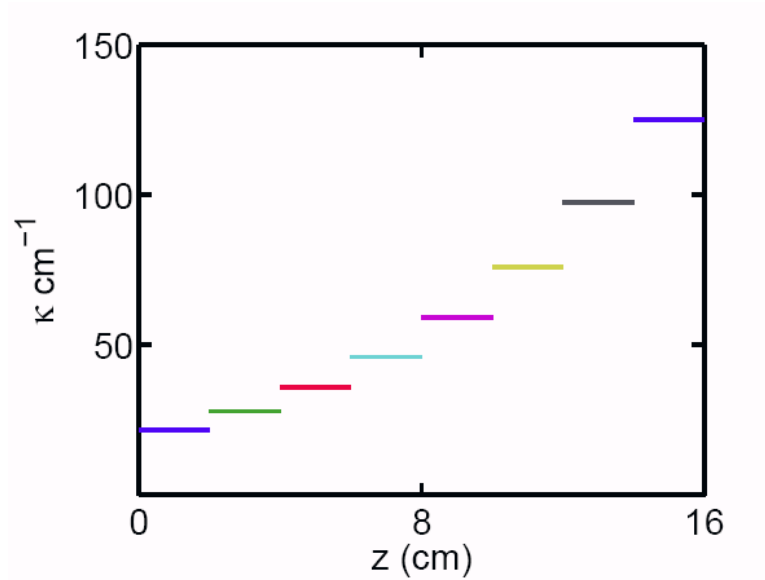
(a)
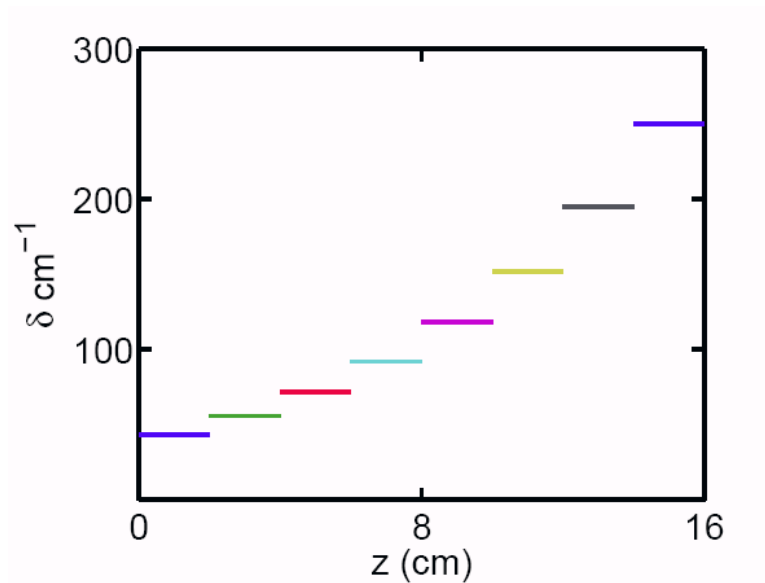
(b)

Figure 3.8: Profiles of coupling coefficient (a) and frequency detuning (b).

Table 3.1: Compression of chirped hyperbolic secant pulse in DDFBG and its 8-section SWA.

		FWHM (ps)	Comp. factor	$C(0)$	$C(z = L)$	Pedestal (%)
DDFBG	NLCMEs	2.3	7.6	-0.5	-0.0668	0.57
	NLSE	2.39	7.39		-0.0677	0
	NLSE+β_3	2.1	8.4		-0.2	6.87
8- section (NLCMEs)		2.4	7.3		-0.014	0.45

Table 3.2: Compression of chirped Gaussian pulse in DDFBG and its 8-section SWA.

		FWHM (ps)	Comp. factor	$C(0)$	$C(z = L)$	Pedestal (%)
DDFBG	NLCMEs	2	8.8	-0.56	-0.06	1
	NLSE	2.1	8.5		-0.05	1
	NLSE+β_3	1.97	8.9		-0.3	6.35
8-section (NLCMEs)		2.1	8.2		-0.003	0.43

curve represent the initial pulse and compressed pulse respectively. The compressed pulse shapes in Fig. 3.1(c) and Fig. 3.1(d) are quite similar, and the comparison in detail is given in Table 3.1. For the compression of chirped Gaussian pulse, Fig. 3.2(d) gives the 8-section SWA of Fig. 3.2(c), where the solid curve and dashed curve represent the initial pulse and compressed pulse respectively. Table 3.2 gives the comparison between the compression of chirped Gaussian pulse in DDFBG and its 8-section SWA, showing 8-section is a good approximation here.

3.3.4 Compression of Chirped Hyperbolic Secant Pulses at Different b

For the example in Section 3.3.1, according to the two constraints imposed by Eq. (3.13) and Eq. (3.14), b should be within 1.9 and 4.2. In Fig. 3.9, we extend Δn further to 0.03, corresponding to $b = 1.5$. We also investigate pulse compression for $b = 4.5, 5, 5.5$ and 6, in which the transmission is expected to be lowered. Figures 3.9(a), (b), (c) and (d) show the compression factor, pedestal (%), transmission (%) and value of M when $b = 1.5, 2, 2.5, \ldots 6$, respectively. The dots and crosses represent the results of hyperbolic secant pulse and Gaussian pulse, respectively. From Fig. 3.9(a), the compression factor drops with the increase of b. From Fig. 3.9(b) and (c), both the pedestal energy and transmission initially increase and then decrease with the increase of b. From Fig. 3.9(d), the value of M increases with the increase of b, meaning the effect of third order dispersion is becoming more and more important. For the hyperbolic secant pulse, the smallest value of M (0.25) occurs when $b = 1.5$, and the second smallest value of M (0.52) occurs when $b = 2$. For the Gaussian pulse, the smallest value of M (0.24) occurs when $b = 1.5$, and the second smallest value of M (0.5) occurs when $b = 2$. The third order dispersion is important because of the large M value. As shown in

Table 3.1, for the compression of hyperbolic secant pulse, the compression factor is 7.39 and the compressed pulse is pedestal free in the NLS approximation. As shown in Table 3.2, for the compression of Gaussian pulse, the compression factor is 8.5 and the pedestal is 1% in the NLS approximation. The results of NLCMEs are close to the NLS approximation at $b = 1.5, 2, 2.5$. Figure 3.10(a), (c) and (e) show the compressed pulse at different b when chirped hyperbolic secant pulse is the initial pulse. The dashed curve, solid curve and dot-dashed curve in Fig. 3.10(a) represent the pulse shape at $b = 1.5, 2$, and 2.5, respectively. The pulses (peak power from high to low) in Fig. 3.10(c) correspond to $b = 3, 3.5$ and 4. The pulses (peak power from high to low) in Fig. 3.10(e) correspond to $b = 4.5$, 5, 5.5 and 6. Figure 3.10(b), (d) and (f) show the compressed pulse when chirped Gaussian pulse is the initial pulse. The dashed curve, solid curve and dot-dashed curve in Fig. 3.10(b) represent the pulse shape at $b = 1.5, 2$, and 2.5, respectively. The pulses (peak power from high to low) in Fig. 3.10(d) correspond to $b = 3, 3.5$ and 4. The pulses (peak power from high to low) in Fig. 3.10(f) correspond to $b = 4.5, 5, 5.5$ and 6. For both the hyperbolic secant and Gaussian shaped pulses, the compressed pulses experience severe distortions at large b (4.5, 5, 5.5 and 6).

Figure 3.11 shows the (a) compression factor, (b) pedestal, (c) transmission, and (d) M versus b in NFBGs with different length. The initial pulse is chirped hyperbolic secant pulse, $\text{sech}(t/T_0)\exp(i\alpha_{20}t^2/2)$, where $T_0 = 10$ ps, and $\alpha_{20} = -0.005$ THz^2. The grating parameters are $\beta_{20} = -25$ ps^2/cm, $\sigma = 0.125$ /cm, $\gamma = 5$ /W/km, $L = 16$ cm (dots), 20 cm (circles), and 25 cm (crosses). The compression factors in the NLS limit are 7.39 (16 cm), 12.18 (20 cm), and 22.76 (25 cm). According to Eq. (3.13) and Eq. (3.14), $1.91<b<4.2$ for $L = 16$ cm, $2.18<b<4.2$ for $L = 20$ cm, and $2.59<b<4.2$ for $L = 25$ cm. For $L = 16$ cm, $b = 2$,

2.5, 3, 3.5, 4, 4.5, 5, 5.5, 6. For $L = 20$ cm, $b = 2.2, 2.5, 3, 3.5, 4, 4.5, 5, 5.5, 6$. For

$L = 25$ cm, $b = 2.6, 3, 3.5, 4, 4.5, 5, 5.5, 6$. As expected, at same b, the

compression factor is higher for a longer grating. When $b<=3.5$, the pedestals are

of similar levels in different lengths of NFBG, when $b>=4$, the levels of pedestals

in NFBGs with different lengths differ. Compressed pulses in different lengths of

NFBGs have similar transmission, and same value of M at same b. Figures 3.12,

3.13 and 3.14 show the evolution of (a) peak power (b) peak power difference (c)

FWHM and (d) FWHM difference along the grating length. Peak power

difference is defined as $(P - P_0)/P_0$, where P and P_0 stand for the peak power in

NLCM simulation and NLS limit, respectively. FWHM difference is defined as

$(F - F_0)/F_0$, where F and F_0 stand for the FWHM in NLCM simulation and

NLS limit, respectively. The physical parameters in Fig. 3.12 are same as that of

the dots in Fig. 3.11 when $b = 2$. The physical parameters in Fig. 3.13 are same as

that of the circles in Fig. 3.11 when $b = 2.2$. The physical parameters in Fig. 3.14

are same as that of the crosses in Fig. 3.11 when $b = 2.6$. The solid curve and dots

respresent the results in NLS limit and the NLCM simulation, respectively. We

note that the peak power and FWHM evolve almost exponentially, but the peak

power difference and FWHM difference show oscillations.

3.4 Effect of Initial Chirp, Dispersion and Pulse Width on the Compression of Chirped Hyperbolic Secant Pulse

3.4.1 Different Initial Chirp

Here we discuss the compression of hyperbolic secant pulses

($\mathrm{sech}(t/T_0)\exp(i\alpha_{20}t^2/2)$, $T_0 = 10$ ps) in NFBGs with exponentially decreasing

dispersion where the values of the initial chirp are different. These compressed
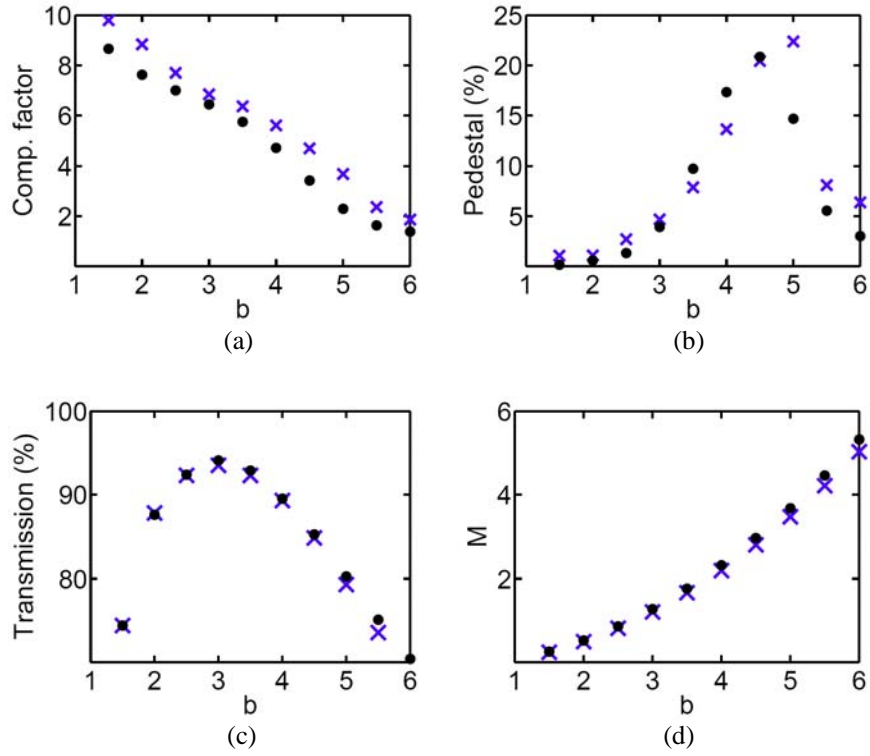
Figure 3.9: (a) Compression factor (b) pedestal (%) (c) transmission (%) (d) M versus b(= 1.5, 2, 2.5, 3, 3.5, 4, 4.5, 5, 5.5 and 6). Chirped hyperbolic secant pulse (dots, sech(t/T_0) exp(i$\alpha_{20}t^2$/2), FWHM = 17.63 ps, α_{20} = −0.005 THz^2) and chirped Gaussian pulse (crosses, exp(−t^2/2/T_0^2)exp(i$\alpha_{20}t^2$/2), FWHM = 17.63 ps, α_{20} = −0.005THz^2) are launched into the NFBGs with exponentially decreasing dispersion. The grating parameters are β_{20} = −25 ps^2/cm, σ = 0.125 /cm, γ = 5 /W/km and L = 16 cm.
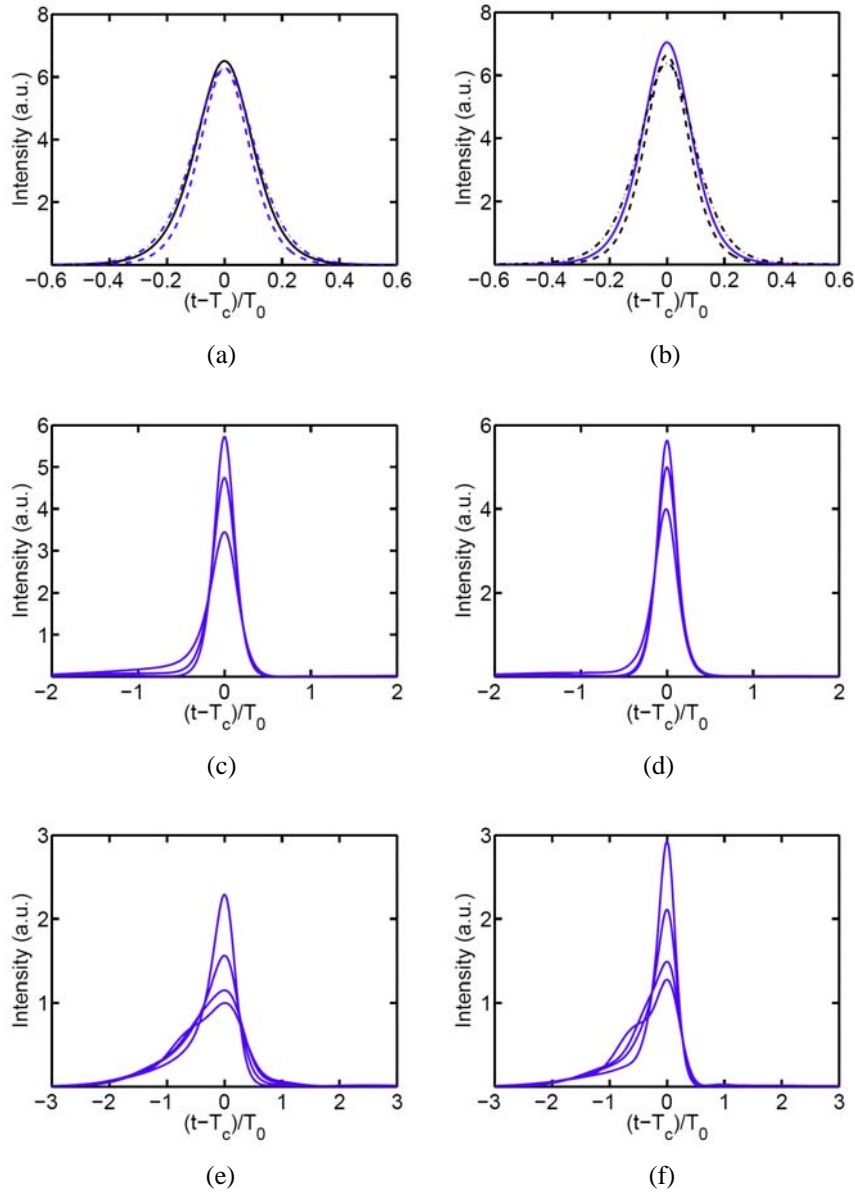
Figure 3.10: Compressed pulse when chirped hyperbolic secant pulse is the initial pulse with (a) $b = 1.5$ (dashed curve), $b = 2$ (solid curve), $b = 2.5$ (dot-dashed curve); (c) $b = 3, 3.5, 4$ (peak power from high to low); (e) $b = 4.5, 5, 5.5, 6$ (peak power from high to low). Compressed pulse when chirped Gaussian pulse is the initial pulse with (b) $b = 1.5$ (dashed curve), $b = 2$ (solid curve), $b = 2.5$ (dot-dashed curve); (d) $b = 3, 3.5, 4$ (peak power from high to low); (f) $b = 4.5, 5, 5.5, 6$ (peak power from high to low). The physical parameters are same as that in Fig. 3.9.
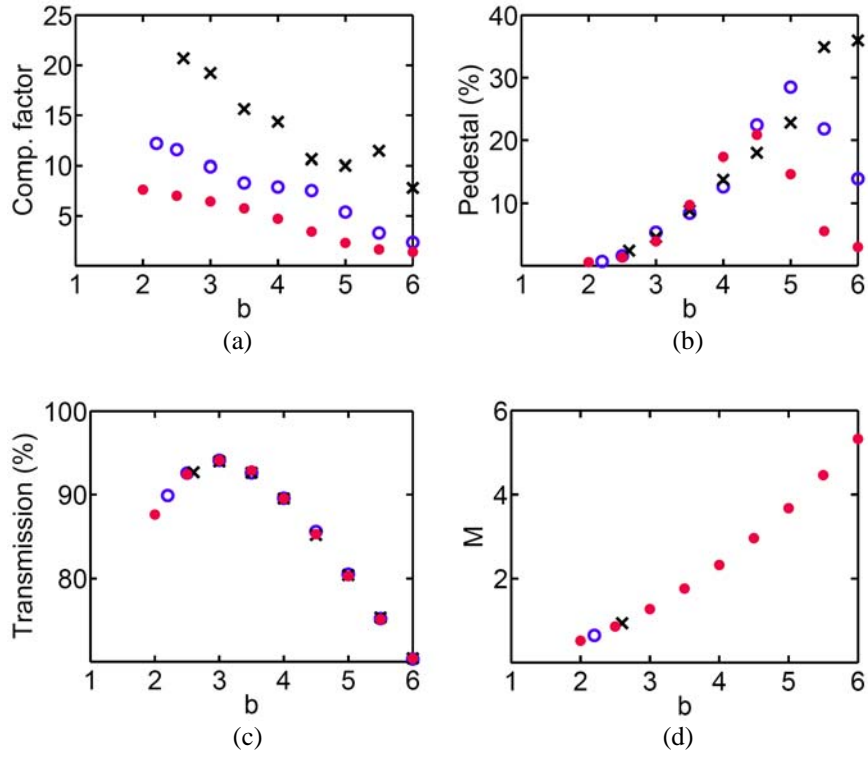
Figure 3.11: (a) Compression factor (b) pedestal (c) transmission (d) M versus b. The initial pulse is $\mathrm{sech}(t/T_0)\exp(i\alpha_{20}t^2/2)$, where $T_0 = 10$ ps, $\alpha_{20} = -0.005$ THz^2. The grating parameters are $\beta_{20} = -25$ ps^2/cm, $\sigma = 0.125$ /cm, $\gamma = 5$ /W/km, $L = 16$ cm (dots), 20 cm (circles), and 25 cm (crosses). For $L = 16$ cm, $b = 2, 2.5, 3, 3.5, 4, 4.5, 5, 5.5, 6$. For $L = 20$ cm, $b = 2.2, 2.5, 3, 3.5, 4, 4.5, 5, 5.5, 6$. For $L = 25$ cm, $b = 2.6, 3, 3.5, 4, 4.5, 5, 5.5, 6$.
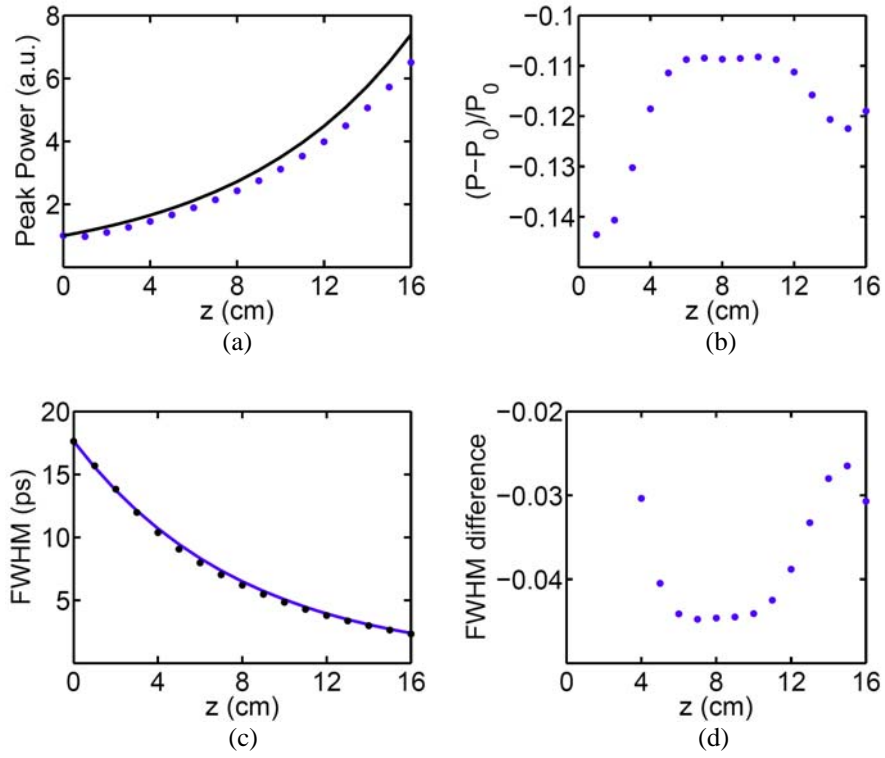
Figure 3.12: Evolution of (a) peak power (b) peak power difference (c) FWHM and (d) FWHM difference along grating length. The physical parameters are same as that of the dots in Fig. 3.11 when $b = 2$. The solid curve and dots represent the self-similar solution, and the results of NLCM simulation, respectively.
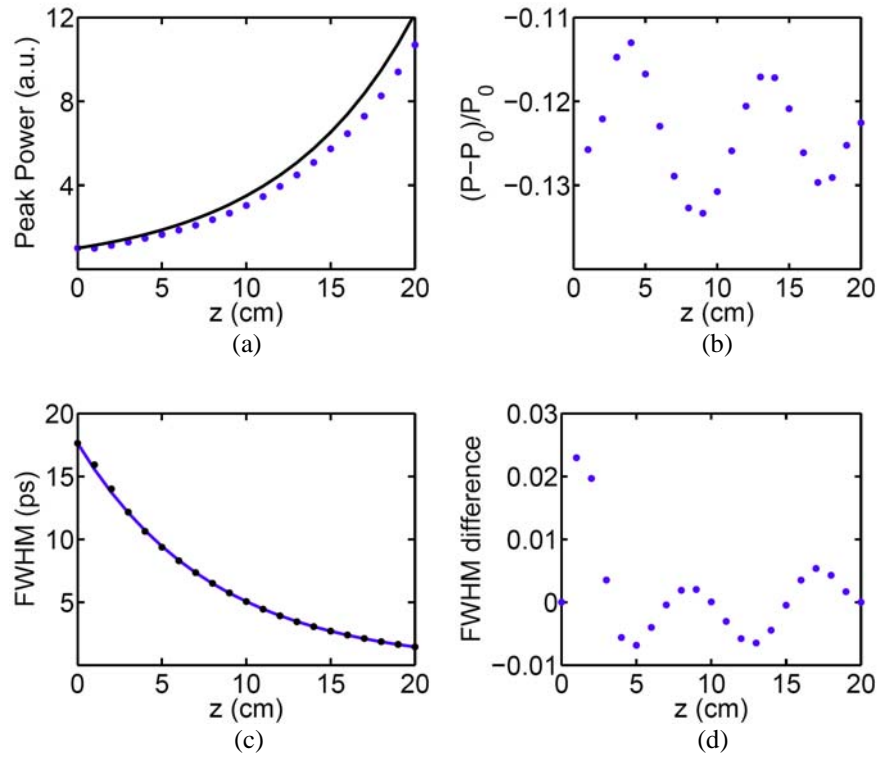
Figure 3.13: Evolution of (a) peak power (b) peak power difference (c) FWHM and (d) FWHM difference along grating length. The physical parameters are same as that of the circles in Fig. 3.11 when $b = 2.2$. The solid curve and dots represent the self-similar solution, and the results of NLCM simulation, respectively.
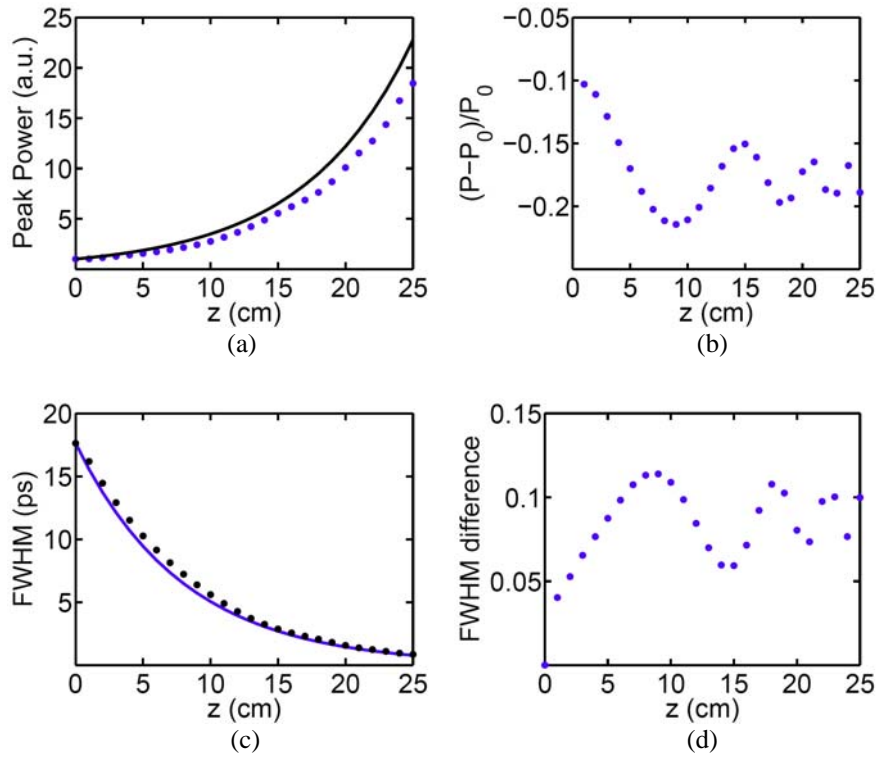
Figure 3.14: Evolution of (a) peak power (b) peak power difference (c) FWHM and (d) FWHM difference along grating length. The physical parameters are same as that of the crosses in Fig. 3.11 when $b = 2.6$. The solid curve and dots represent the self-similar solution, and the results of NLCM simulation, respectively.

pulses have same compression factor in the NLS limit. The solid curve in Fig. 3.15 (a), (b), (c) and (d) corresponds to the compressed pulse in Fig. 3.1. Figure 3.15(a) and (c) show the compressed pulse in linear and logarithmic scale respectively, where the physical parameters for the dashed curve are $\alpha_{20} = -0.0025$ THz^2, $\beta_{20} = -25$ ps^2/cm, $\sigma = \alpha_{20}\beta_{20}$, $b = 2$, $\gamma = 5$ /W/km, and $L = 32$ cm. The compressed pulse is 2.28 ps (FWHM) with 0.06% pedestal. Figure 3.15(b) and (d) show the compressed pulse in linear and logarithmic scale respectively, where the physical parameters for the dashed curve are $\alpha_{20} = -0.01$ THz^2, $\beta_{20} = -25$ ps^2/cm, $\sigma = \alpha_{20}\beta_{20}$, $b = 2$, $\gamma = 5$ /W/km, and $L = 8$ cm. The compressed pulse is 2.38 ps (FWHM) with 3.4% pedestal. The pulse with a larger initial chirp has a wider bandwidth, therefore the compression in the transmission region is not as effective as the one with a smaller initial chirp. Figure 3.15(e) and (f) show the spectra of initial pulse (solid curve) and compressed pulse (dashed curve) for Fig. 3.15(a) and (b), respectively. For both the cases, the compressed pulses experience obvious bandwidth broadening.

3.4.2 Different Initial Dispersion

Here we discuss the compression of hyperbolic secant pulses ($\operatorname{sech}(t/T_0)\exp(i\alpha_{20}t^2/2)$, $\alpha_{20} = -0.005$ THz^2, $T_0 = 10$ ps) in NFBGs with exponentially decreasing dispersion where the values of the initial dispersion are different. These compressed pulses have same compression factor in the NLS limit. The solid curve in Fig. 3.16 (a), (b), (c) and (d) corresponds to the compressed pulse in Fig. 3.1. Figure 3.16(a) and (c) show the compressed pulse in linear and logarithmic scale respectively, where the physical parameters for the dashed curve are $\beta_{20} = -12.5$ ps^2/cm, $\sigma = \alpha_{20}\beta_{20}$, $b = 2$, $\gamma = 5$ /W/km, and

$L = 32$ cm. The compressed pulse is 2.24 ps (FWHM) with 0.2% pedestal. Figure 3.16(b) and (d) show the compressed pulse in linear and logarithmic scale respectively, where the physical parameters for the dashed curve are $\beta_{20} = -50$ ps^2/cm, $\sigma = \alpha_{20}\beta_{20}$, $b = 2$, $\gamma = 5$ /W/km, and $L = 8$ cm. The compressed pulse is 2.55 ps (FWHM) with 2% pedestal. According to Eq. (3.11), the value of M is proportional to the initial dispersion. Thus, the one with a smaller initial dispersion has better pulse quality, showing shorter pulse and less pedestal. Figure 3.16(e) and (f) show the spectra of initial pulse (solid curve) and compressed pulse (dashed curve) for Fig. 3.16(a) and (b), respectively. For both the cases, the compressed pulses experience obvious bandwidth broadening.

3.4.3 Different Initial Pulse Width

Here we discuss the compression of hyperbolic secant pulses ($\operatorname{sech}(t/T_0)\exp(i\alpha_{20}t^2/2)$, $\alpha_{20} = -0.005$ THz^2) in NFBGs with exponentially decreasing dispersion where the initial pulse widths are different. The solid curve in Fig. 3.17 (a), (b), (c) and (d) corresponds to the compressed pulse in Fig. 3.1. Figure 3.17(a) and (c) show the compressed pulse in linear and logarithmic scale respectively, where the physical parameters for the dashed curve are $T_0 = 5$ ps, $\beta_{20} = -25$ ps^2/cm, $\sigma = \alpha_{20}\beta_{20}$, $b = 2$, $\gamma = 5$ /W/km, and $L = 16$ cm. Figure 3.17(b) and (d) show the compressed pulse in linear and logarithmic scale respectively, where the physical parameters for the dashed curve are $T_0 = 50$ ps, $\beta_{20} = -25$ ps^2/cm, $\sigma = \alpha_{20}\beta_{20}$, $b = 2$, $\gamma = 5$ /W/km, and $L = 16$ cm. Figure 3.17(e) and (f) show the spectra of initial pulse (solid curve) and compressed pulse (dashed curve) for Fig. 3.17(a) and (b), respectively. The pulse compression shown in Fig. 3.17 (b), (d) and (f) are quite different from the

cases we have discussed. The compressed pulse has serious distortions, and becomes asymmetric with an oscillatory structure near the trailing edge. Despite the compression in time domain, there is no obvious bandwidth broadening. This is the so called quasi-linear case discussed in Chapter 2. The ratio of chirp length to initial nonlinear length L_C / L_{N0} is found to be 0.08, which is much smaller than 1. Therefore, the fast behavior of the soliton is governed by the dispersion only. Because of the large and positive third order dispersion here, deep oscillations appear near the trailing edge.

3.5 Compression of Prechirped Hyperbolic Secant and Gaussian Pulses

Similar to Section 2.3, here, we study the compression of initially chirp-free pulse using a linear FBG or fiber to produce the required chirp profile for the compression in NFBGs with exponentially decreasing dispersion. Here, we assume that the input pulse is chirp-free hyperbolic secant pulse or Gaussian pulse. We study the pre-chirping process in the linear grating or linear fiber. Our simulation results show that the pedestal generated from an input Gaussian pulse is much smaller than that from an input hyperbolic secant pulse showing that the compression by the NFBG is more sensitive to the chirp profile than the pulse shape. The initial Gaussian profile evolves into a hyperbolic secant profile after the compression in the NFBG.

3.5.1 Prechirp by Grating or Fiber

We consider using either linear grating or linear fiber with normal dispersion as a pre-chirper. Grating and fiber have same total dispersion $\beta_{2,\text{lin}} L_0$, where $\beta_{2,\text{lin}}$ and L_0 are dispersion and length of the pre-chirper, respectively. The pre-chirping
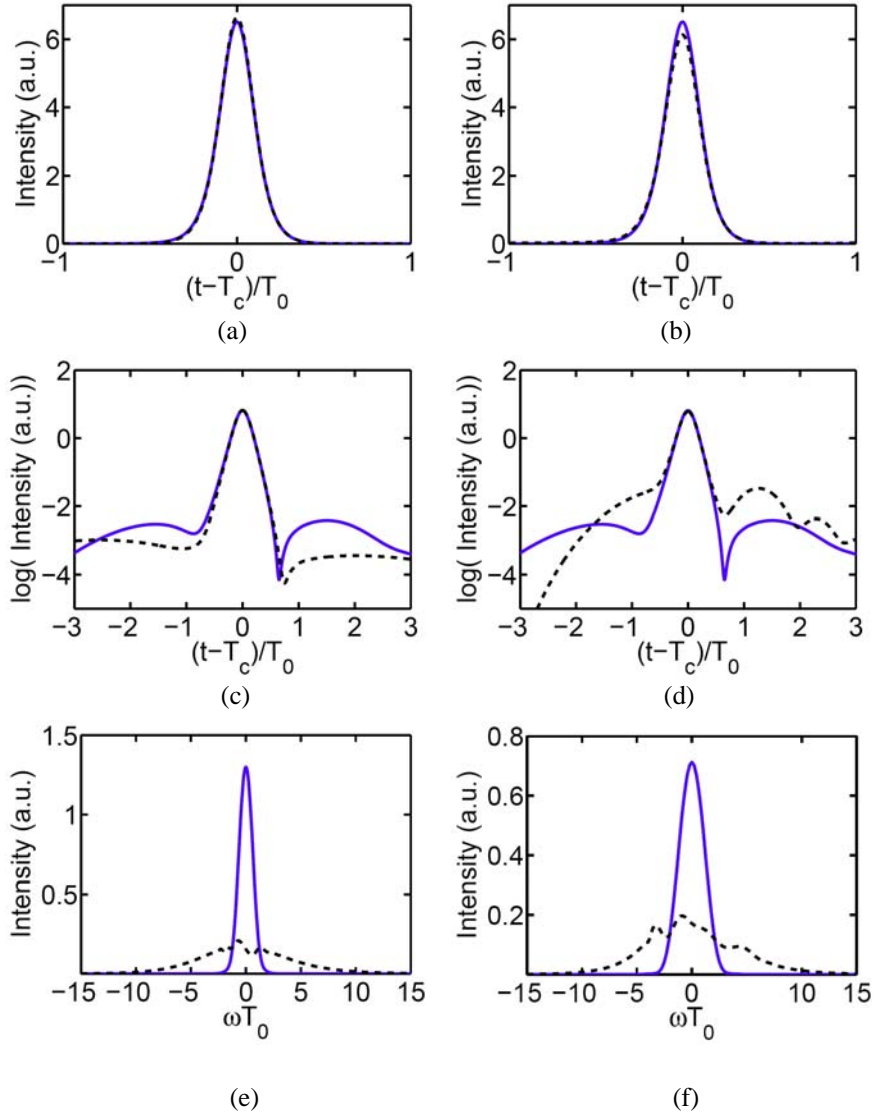
Figure 3.15: Chirped hyperbolic secant pulse ($\mathrm{sech}(t/T_0)\exp(\mathrm{i}\alpha_{20}t^2/2)$, T_0=10ps) is the initial pulse. Compressed pulse in (a) linear and (c) logarithmic scale where the physical parameters for the dashed curve are $\alpha_{20} = -0.0025$ THz^2, $\beta_{20} = -25$ ps^2/cm, $b = 2$, $\gamma = 5$ /W/km, $L = 32$ cm. Compressed pulse in (b) linear and (d) logarithmic scale where the physical parameters for the dashed curve are $\alpha_{20} = -0.01$ THz^2, $\beta_{20} = -25$ ps^2/cm, $b = 2$, $\gamma = 5$ /W/km, $L = 8$ cm. The solid curve in (a, b, c, d) corresponds to the compressed pulse in Fig. 3.1. (e) Spectra of initial pulse (solid curve) and compressed pulse (dashed curve) for Fig. 3.15 (a). (f) Spectra of initial pulse (solid curve) and compressed pulse (dashed curve) for Fig. 3.15 (b).

Table.3.3: FWHM(ps) and pedestal(%) of compressed pulse in the simulation of NLCMEs and NLSE. Chirp-free "sech" or Gaussian pulse with same FWHM is the initial pulse. #: DDFBG; *: 8-section SWA.

	FWHM(ps)	Pedestal(%)
"sech" (NLSE)	$2.65^{\#}$ 2.73^{*}	$6.24^{\#}$ 5.09^{*}
"sech" (grating prechirper)	$2.41^{\#}$ 2.52^{*}	$3.5^{\#}$ 2.5^{*}
"sech" (fiber prechirper)	$2.36^{\#}$ 2.47^{*}	$3.43^{\#}$ 2.39^{*}
Gaussian (NLSE)	$2.65^{\#}$ 2.74^{*}	$0.1^{\#}$ 0.92^{*}
Gaussian (grating prechirper)	$2.64^{\#}$ 2.74^{*}	$1^{\#}$ 0.1^{*}
Gaussian (fiber prechiper)	$2.56^{\#}$ 2.66^{*}	$0.76^{\#}$ 0.21^{*}
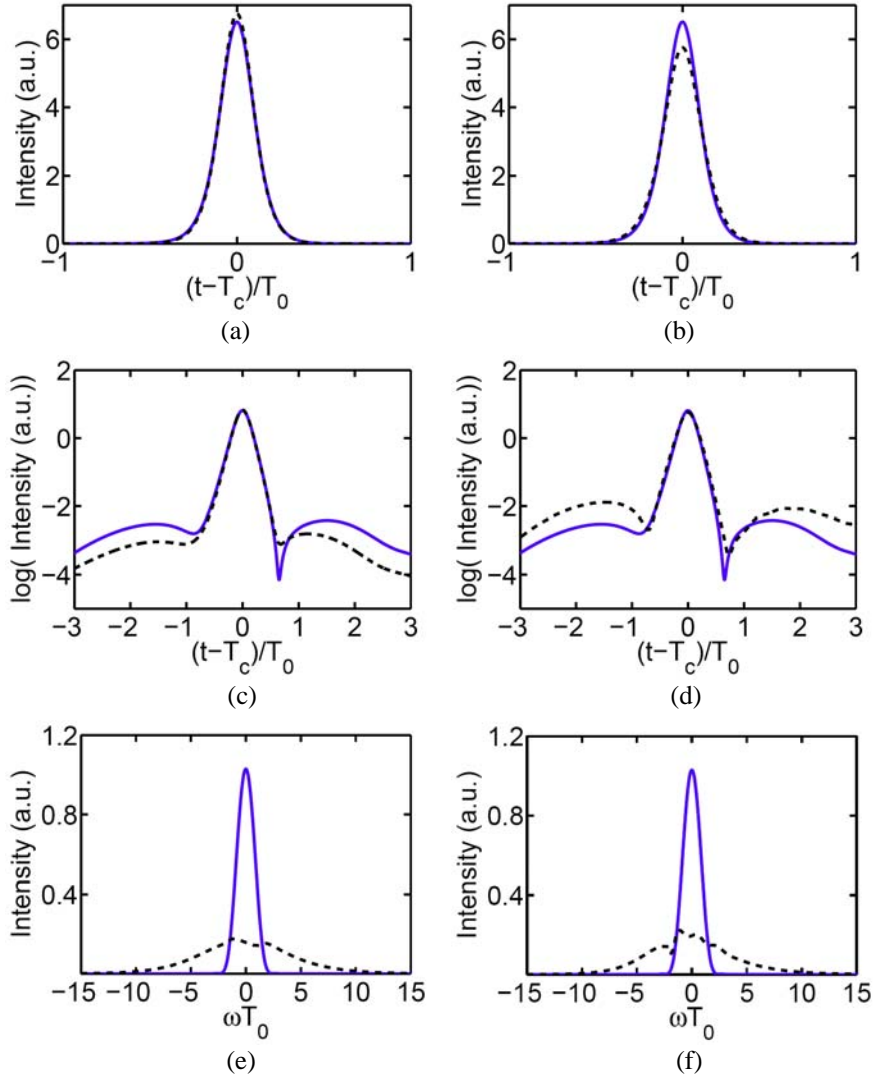
Figure 3.16: Chirped hyperbolic secant pulse (sech(t/T_0) exp(i$\alpha_{20}t^2/2$), $\alpha_{20} = -0.005$ THz^2, T_0 = 10 ps) is the initial pulse. Compressed pulse in (a) linear and (c) logarithmic scale where the physical parameters for the dashed curve are $\beta_{20} = -12.5$ ps^2/cm, $b = 2$, $\gamma = 5$ /W/km, $L = 32$ cm. Compressed pulse in (b) linear and (d) logarithmic scale where the physical parameters for the dashed curve are $\beta_{20} = -50$ ps^2/cm, $b = 2$, $\gamma = 5$ /W/km, $L = 8$ cm. The solid curve in (a, b, c, d) corresponds to the compressed pulse in Fig. 3.1. (e) Spectra of initial pulse (solid curve) and compressed pulse (dashed curve) for Fig. 3.16(a). (f) Spectra of initial pulse (solid curve) and compressed pulse (dashed curve) for Fig. 3.16(b).
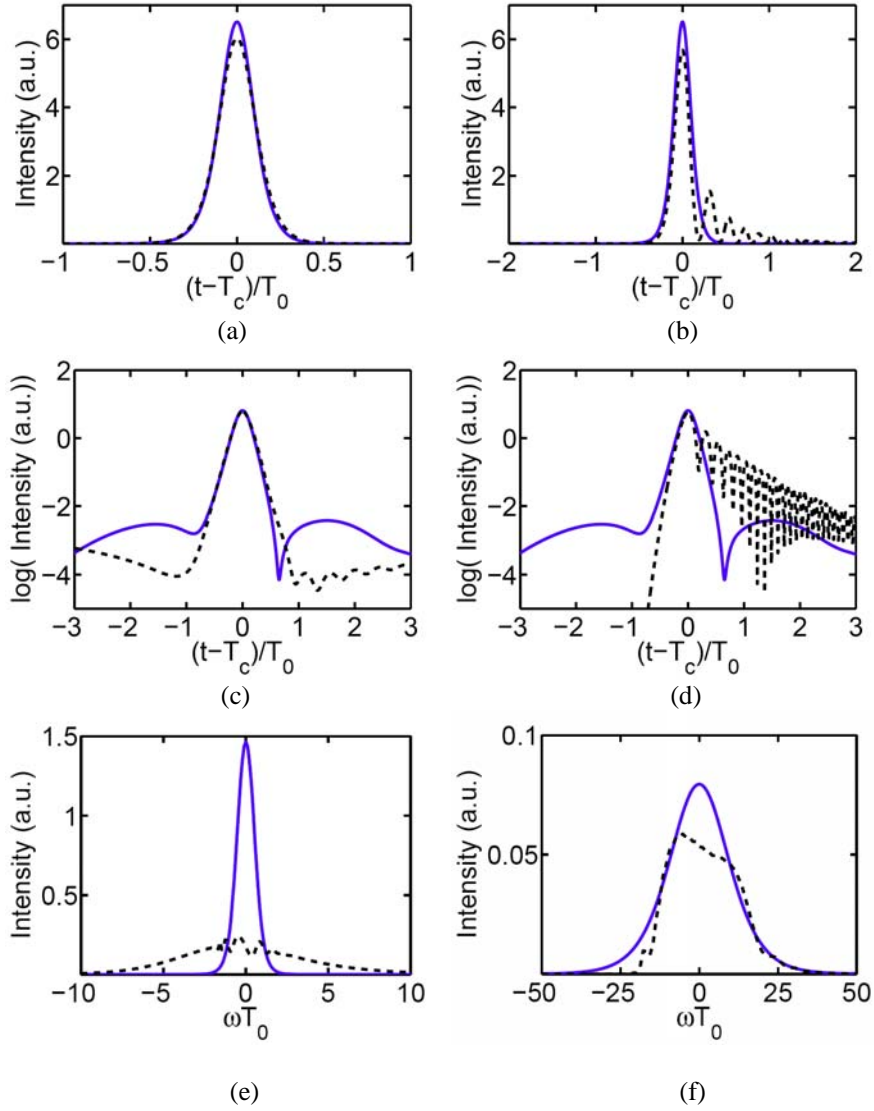
Figure 3.17: Chirped hyperbolic secant pulse ($\mathrm{sech}(t/T_0)\,\exp(i\alpha_{20}t^2/2)$, $\alpha_{20} = -0.005$ THz^2) is the initial pulse. Compressed pulse in (a) linear and (c) logarithmic scale where the physical parameters for the dashed curve are $T_0 = 5$ ps, $\beta_{20} = -25$ ps^2/cm, $b = 2$, $\gamma = 5$ /W/km, $L = 16$ cm. Compressed pulse in (b) linear and (d) logarithmic scale when the physical parameters for the dashed curve are $T_0 = 50$ps, $\beta_{20} = -25$ ps^2/cm, $b = 2$, $\gamma = 5$ /W/km, $L = 16$ cm. The solid curve in (a, b, c, d) corresponds to the compressed pulse in Fig. 3.1. (e) Spectra of initial pulse (solid curve) and compressed pulse (dashed curve) for Fig. 3.17 (a). (f) Spectra of initial pulse (solid curve) and compressed pulse (dashed curve) for Fig. 3.17 (b).

process in the linear grating and fiber are described by NLCMEs ($\gamma = 0$) and NLSE ($\gamma_g = 0$), respectively. If $\beta_{2,\text{lin}} = 25$ ps^2/cm, using Eq. (3.12) and Eq. (3.14) when $C = 0$, and $\sigma = 0$, we have $1.3 < |b| < 4.35$ and $1.3 < |b| < 4.49$ for the pre-chirping of hyperbolic secant and Gaussian pulse, respectively. Chirp free hyperbolic secant pulse ($\text{sech}(t/T_0)$, $T_0 = 9.45$ ps, FWHM = 16.65 ps) is launched into a linear grating ($\beta_{2,\text{lin}} = 25$ ps^2/cm, $\delta = -1.3\kappa$, $L_0 = 2$ cm) or a dispersion compensated fiber (DCF, $\beta_{2,\text{lin}} = 100$ ps^2/km, $\beta_{3,\text{lin}} = -0.5$ ps^3/km, loss = 0.5 dB/km, $L_0 = 0.5$ km). The pre-chirped "sech" like pulses are shown in Fig. 3.18(a), where the solid curve and dashed curve represent the pre-chirped pulse in grating pre-chirper and fiber pre-chirper, respectively. Similarly, chirp-free Gaussian pulse ($T_0 = 10$ ps, FWHM = 16.65 ps) is launched into a linear grating ($\beta_{2,\text{lin}} = 25$ ps^2/cm, $\delta = -1.3\kappa$, $L_0 = 4$ cm) or a dispersion compensated fiber (DCF, $\beta_{2,\text{lin}} = 100$ ps^2/km, $\beta_{3,\text{lin}} = -0.5$ ps^3/km, loss = 0.5dB/km, $L_0 = 1$ km). The pre-chirped Gaussian pulses are shown in Fig. 3.18(b), where the solid curve and dashed curve represent the pre-chirped pulse in grating pre-chirper and fiber pre-chirper, respectively. Grating pre-chirped "sech" like pulse is 21 ps (FWHM), with chirp $\alpha_{20} = -0.0044$ THz^2 and 6.4% pedestal, while fiber pre-chirped "sech" like pulse is 21 ps (FWHM), with $\alpha_{20} = -0.0045$ THz^2 and 6.5% pedestal. Grating pre-chirped Gaussian pulse is 23.5 ps (FWHM), with $\alpha_{20} = -0.0049$THz^2 and 0.2% pedestal, while fiber pre-chirped Gaussian pulse is 23.5 ps, with $\alpha_{20} = -0.005$ THz^2 and 0.007% pedestal. The value of α_{20} is determined by the polynomial fit of the phase of the pre-chirped pulse. The pedestal energy is calculated when fit the pre-chirped pulse with hyperbolic secant or Gaussian

shaped pulse.

3.5.2 Compression of Prechirped Pulses

Pre-chirped "sech" like pulse by grating or fiber is sent to the NFBG with exponentially decreasing dispersion. The grating parameters are $L = 19.2$ cm, $\beta_{20} = -25$ ps^2/cm, $\sigma = \alpha_{20}\beta_{20}$. According to Eq. (3.13) and (3.14), we have $1.97 < b < 4.32$, and we will use $b = 2$ for the following discussions. The grating pre-chirped "sech" like pulse can be compressed to 2.4 ps (FWHM) with small pedestal (3.5%), as shown by the solid curve in Fig. 3.18(c). The fiber pre-chirped "sech" like pulse can be compressed to 2.36 ps (FWHM) with small pedestal (3.4%), as shown by the dashed curve in Fig. 3.18(c). We implement 8-section stepwise approximation (SWA) of the nonlinear compression of the grating/fiber pre-chirped "sech" like pulse, and it can be compressed to 2.5 ps (FWHM) with 2.5% pedestal, and 2.5 ps (FWHM) with 2.4% pedestal, respectively, as shown by the solid curve and dashed curve in Fig. 3.18(e). The compressed pulse in 8-section SWA is very close to the one in DDFBG. Similarly, the pre-chirped Gaussian pulse by grating or fiber is sent to the NFBG with exponentially decreasing dispersion. The grating parameters are $L = 16$ cm, $\beta_{20} = -25$ ps^2/cm, $\sigma = \alpha_{20}\beta_{20}$. According to Eq. (3.13) and (3.14), we have $1.92 < b < 4.48$, and we will use $b = 2$ for the following discussions. The grating pre-chirped Gaussian pulse can be compressed to 2.6 ps (FWHM) with 1% pedestal, as shown by the solid curve in Fig. 3.18(d). The fiber pre-chirped Gaussian pulse can be compressed to 2.6 ps (FWHM) with 0.8% pedestal, as shown by the dashed curve in Fig. 3.18(d). We implement 8-section SWA of the nonlinear compression of the grating/fiber pre-chirped Gaussian pulse, and it can be compressed to 2.7 ps (FWHM) with 0.1% pedestal, 2.7 ps (FWHM) with 0.2%

pedestal, respectively, as shown by the solid curve and dashed curve in Fig. 3.18(f). The compressed pulse in 8-section SWA is very close to the one in the DDFBG.

Table 3.3 compares the FWHM and pedestal of the compressed pulse in the simulations of NLCMEs and NLSE, which shows that NLSE is a rather good approximation. Under the NLS approximation, chirp-free hyperbolic secant pulse and chirp-free Gaussian pulse, which have same FWHM, can be compressed to hyperbolic secant pulse with same FWHM. However, the pedestal generated from the initial Gaussian pulse is smaller. The compressed pulses from the linear grating pre-chirper and linear fiber pre-chirper are similar. The Gaussian compression scheme is more attractive, showing a larger chirp can be obtained from pre-chirping, which means a shorter NFBG can be used.

3.6 Minimum Pulse Width

Here we study the minimum pulse width that can be achieved by the proposed NFBG with exponentially decreasing dispersion. We calculate the minimum pulse width under the limit of Δn is 0.01. Eq. (3.14) can be rewritten as

$$\exp(\sigma z) \leq \frac{\eta 0.01\pi}{2\Lambda n} \frac{\left(b^2-1\right)^{3/2}|\beta_{20}|}{\beta_1^2}. \tag{3.15}$$

From Eq. (3.15), the ideal compression factor $\exp(\sigma z)$ is associated with the value of b, and the value of $|\beta_{20}|$. For large compression factor, large b and large $|\beta_{20}|$ are expected. Therefore, we study the compressed pulse width and pedestal versus different b or $|\beta_{20}|$. As discussed in Section 2.1.2, we are interested in the cases when $\varepsilon = L_C / L_D(0) \sim 1$. Figure 3.19 shows the FWHM and pedestal of the compressed pulse versus different initial dispersion. $b = 2$ is
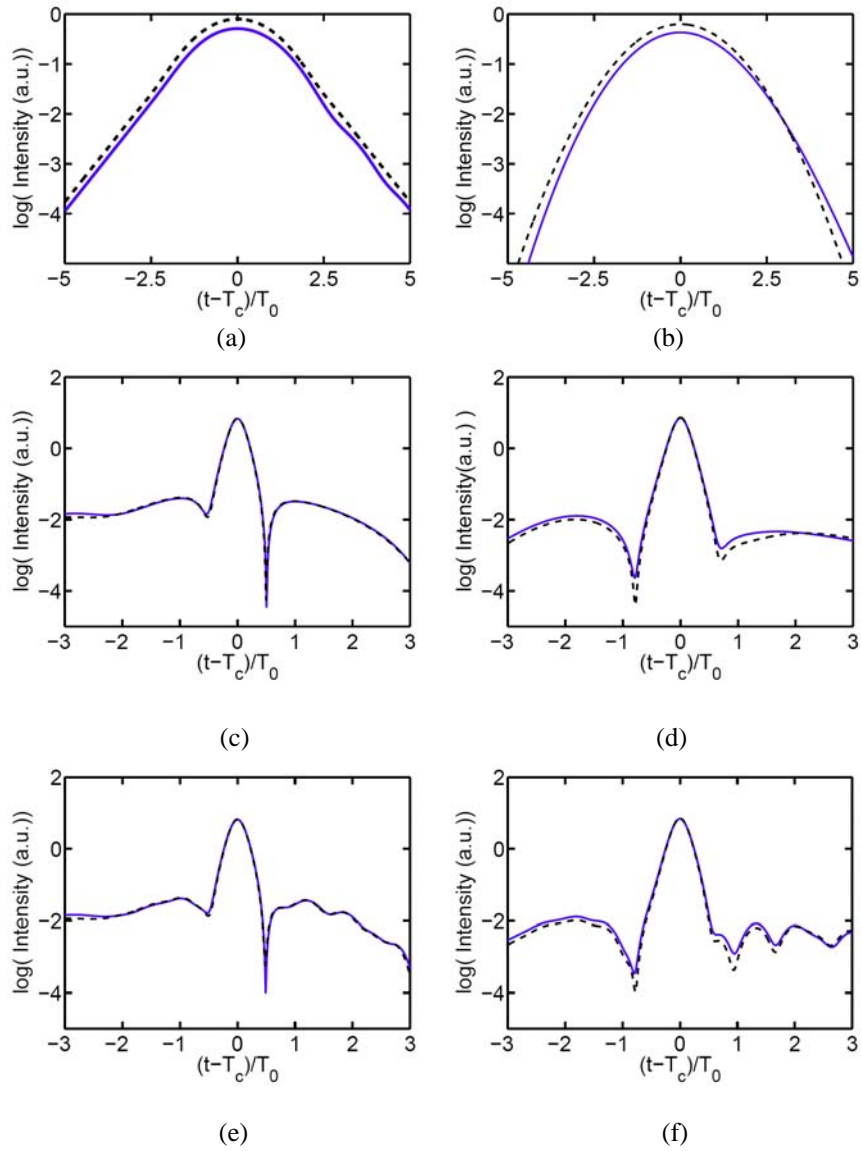
Figure 3.18: Pre-chirped pulse when (a) chirp-free hyperbolic secant pulse or (b) chirp-free Gaussian pulse is the initial pulse. Compressed pulses when (c) chirp-free hyperbolic secant pulse or (d) chirp-free Gaussian pulse is the initial pulse. (e) Compressed pulse in 8-section SWA of Fig. 3.18(c). (f) Compressed pulse in 8-section SWA of Fig. 3.18(d). Solid curve: linear grating is the prechirper. Dashed curve: linear fiber is the prechirper.

used in Fig. 3.19. For the given b, the upper limit of $|\beta_{20}|$ can be calculated by Eq. (3.13). And we have calculated the minimum pulse width when $|\beta_{20}| = 25$, 37.5, 50…100 ps^2/cm. Dots represent the results where $T_0 = 10$ ps, $\alpha_{20} = -0.005$ THz^2, $\varepsilon = 2$. Circles represent the results where $T_0 = 10$ ps, $\alpha_{20} = -0.01$ THz^2, $\varepsilon = 1$. Crosses represent the results where $T_0 = 20$ ps, $\alpha_{20} = -0.005$ THz^2, $\varepsilon = 0.5$. Plus signs represent the results where $T_0 = 5$ ps, $\alpha_{20} = -0.04$ THz^2, $\varepsilon = 1$. For each case, the FWHM of compressed pulse decreases with the increase of $|\beta_{20}|$, but the pedestal of compressed pulse increases with the increase of $|\beta_{20}|$. At same $|\beta_{20}|$, the one with a larger ε has a smaller pedestal, such as dots, circles and crosses. If same ε, such as circles and plus signs, the pedestal is determined by the value of M. A smaller M corresponds to a smaller pedestal. Figures 3.20 and 3.21 show the FWHM and pedestal of the compressed pulse versus different b. $|\beta_{20}| = 25$ ps^2/cm is used in Fig. 3.20, and $|\beta_{20}| = 100$ ps^2/cm is used in Fig. 3.21. For a given $|\beta_{20}|$, the upper limit of b can be calculated by Eq. (3.13). In both Fig. 3.20 and Fig. 3.21, dots represent the results where $T_0 = 10$ ps, $\alpha_{20} = -0.005$ THz^2, circles represent the results where $T_0 = 10$ ps, $\alpha_{20} = -0.01$ THz^2, crosses represent the results where $T_0 = 20$ ps, $\alpha_{20} = -0.005$ THz^2, and plus signs represent the results where $T_0 = 5$ ps, $\alpha_{20} = -0.04$ THz^2. Similarly, the FWHM of compressed pulse decreases with the increase of b, but the pedestal of compressed pulse increases with the increase of b. At same b, the one with a larger ε has a smaller pedestal,
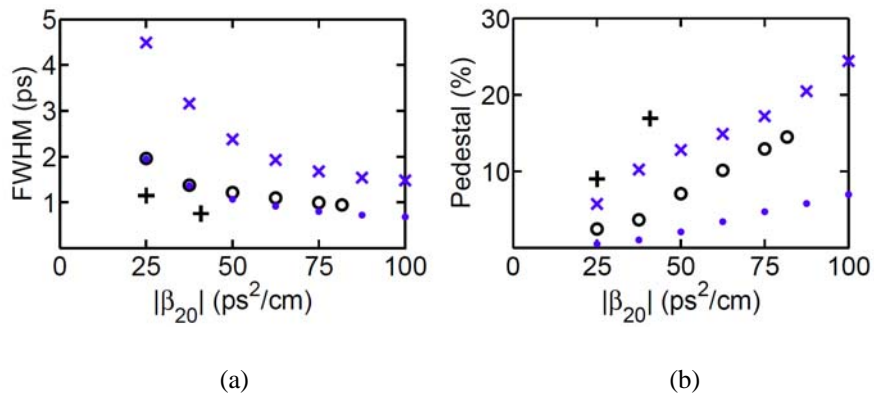
Figure 3.19: (a) FWHM (ps) and (b) pedestal (%) of the compressed pulse versus different initial dispersion. Dots: $b = 2$, $T_0 = 10$ ps, $\alpha_{20} = -0.005$ THz^2, $\varepsilon = 2$; circles: $b = 2$, $T_0 = 10$ ps, $\alpha_{20} = -0.01$ THz^2, $\varepsilon = 1$; crosses: $b = 2$, $T_0 = 20$ ps, $\alpha_{20} = -0.005$ THz^2, $\varepsilon = 0.5$; plus signs: $b = 2$, $T_0 = 5$ ps, $\alpha_{20} = -0.04$ THz^2, $\varepsilon = 1$.

(a)　　　　　　　　　　　　(b)
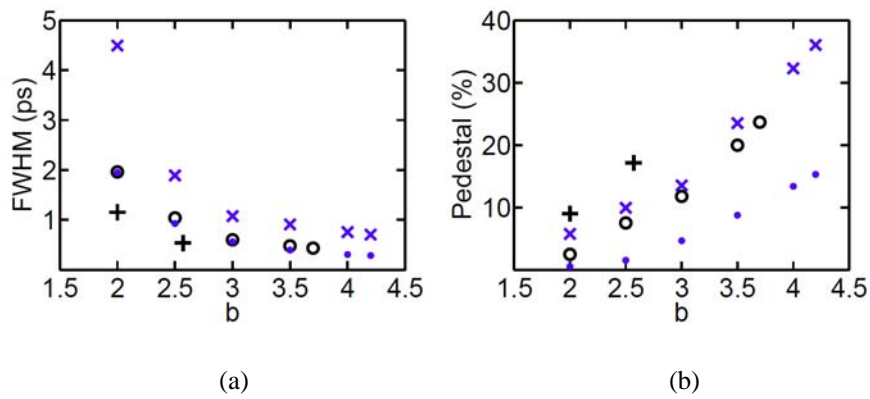
Figure 3.20: (a) FWHM (ps) and (b) pedestal (%) of the compressed pulse versus different b.

Dots: $\beta_{20} = -25$ ps^2/cm, $T_0 = 10$ ps, $\alpha_{20} = -0.005$THz^2; circles: $\beta_{20} = -25$ ps^2/cm, $T_0 = 10$ ps, $\alpha_{20} = -0.01$THz^2; crosses: $\beta_{20} = -25$ ps^2/cm, $T_0 = 20$ ps, $\alpha_{20} = -0.005$THz^2; plus signs: $\beta_{20} = -25$ ps^2/cm, $T_0 = 5$ ps, $\alpha_{20} = -0.04$ THz^2.

(a)	(b)
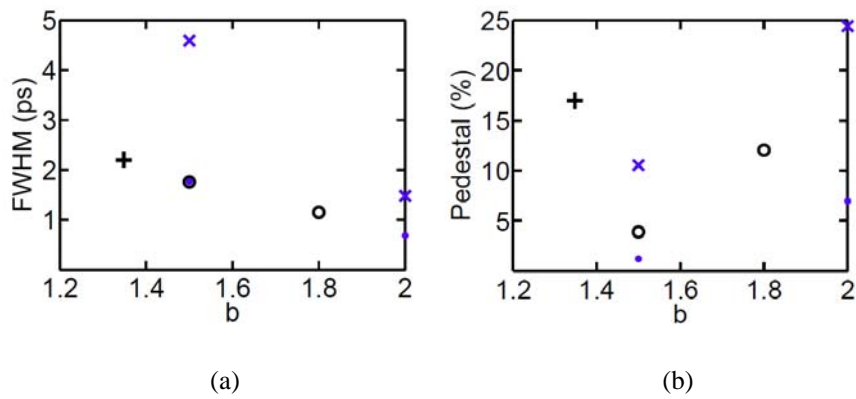
Figure 3.21: (a) FWHM (ps) and (b) pedestal (%) of the compressed pulse versus different b.

Dots: $\beta_{20} = -100$ ps^2/cm, $T_0 = 10$ ps, $\alpha_{20} = -0.005$THz^2; circles: $\beta_{20} = -25$ ps^2/cm, $T_0 = 10$ ps, $\alpha_{20} = -0.01$THz^2; crosses: $\beta_{20} = -100$ ps^2/cm, $T_0 = 20$ ps, $\alpha_{20} = -0.005$THz^2; plus signs: $\beta_{20} = -100$ ps^2/cm, $T_0 = 5$ ps, $\alpha_{20} = -0.04$ THz^2.

such as dots, circles and crosses. If same ε, such as circles and plus signs, the pedestal is determined by the value of *M*.

3.7 Summary

In Chapter 2 we have demonstrated the nonlinear Fiber Bragg Grating with exponentially decreasing dispersion allows for almost chirp-free and pedestal-free pulse compression in short length, leading to a novel all-fiber compression device. Our earlier studies are based on the NLS approximation. In this Chapter, we have looked into the effect of higher order dispersions, and use the generalized nonlinear coupled mode equations to have a full study of the proposed compressor. It turns out that, while the second order dispersion is exponentially decreasing, the relative importance of different higher order dispersions keeps unchanged in the whole compression process. Therefore, we define a figure of merit *M*, which is the ratio of the second order dispersion length and third order dispersion length to measure the effect of higher order dispersions. The value of *M* is proportional to the value of $\left|\beta_{20}\right|$ and *b*, but inversely proportional to the initial pulse width parameter. For optimum pulse compression, *M* should be as small as possible. From a realistic point of view, the exponential decreasing dispersion profile is well approximated by a number of gratings with constant dispersions. However, the solution to the NLS type equation with exponentially decreasing dispersion is chirped. Therefore, we suggest a compact compression scheme which consists of a pre-chirper (linear grating or linear fiber) and a NFBG. The proposed scheme can effectively compress both hyperbolic secant and Gaussian shaped pulse profiles. The initially Gaussian shaped pulse has evolved into hyperbolic secant shaped pulse. We have also studied the minimum pulse width that can be achieved by the NFBG with exponentially decreasing dispersion,

and 500 fs (FWHM) with around 5% pedestal can be obtained.

The short compressor requires high input intensity, making these compressors very useful for high-power YAG-type systems. Using high-n_2 fiber will lower the required intensity, making this compressor useful for many other laser systems. Chalcogenide fibers have measured values of n_2 that are ~100 larger than silica at 1.55 μm [78] and fabrication of Bragg gratings in chalcogenide glass fiber using the transverse holographic method has been reported in [78].

Although the nonlinear Fiber Bragg grating is a good candidate for the self-similar pulse compression, structures other than FBGs, such as deep-etched gratings with large Δn or other types of photonic crystals, where the structure's parameters may easily be controlled, may also be used.

Chapter 4

Robust Pulse Compression in Cubic-Quintic Nonlinear Media

In this chapter, we consider the evolution of nonlinear optical pulses in the cubic-quintic (CQ) nonlinear media wherein the pulse propagation is governed by the generalized nonlinear Schrödinger equation with exponentially varying dispersion, cubic and quintic nonlinearities, and gain/loss. Section 4.2 discusses the theoretical model and the origin of the fifth order (quintic) nonlinearity. In Section 4.3, we find the chirped bright soliton solutions in the anomalous and normal dispersion regimes using the self-similar analysis. We then determine the relation among the dispersion length, cubic nonlinear and quintic nonlinear length. From the stability analysis, we show that the solitary wave solution in the anomalous dispersion regime is stable whereas the solitary wave solution in the normal dispersion regime is unstable. Numerical simulation results show that competing cubic-quintic nonlinearities stabilize the chirped soliton pulse propagation against perturbations in the initial soliton pulse parameters. We characterize the quality of the compressed pulse by calculating the generated pedestal energy and compression factor when the initial pulse is perturbed from the soliton solutions. We also presented the chirped self-similar Townes soliton of

the pure quintic NLS equation with exponentially varying dispersion in Section 4.4, and we study the possibility of rapid compression of Townes solitons by the collapse phenomenon in the exponentially decreasing dispersion. We also found that the collapse could be postponed if the dispersion increases exponentially. Finally, we conclude in Section 4.5.

4.1 Introduction

Contrary to the conventional pulse compression techniques discussed in Chapter 4, a new technique has been proposed based on the filamentation and plasma generation in the high intensity region [79–82]. When the intensity of the incident field is high enough in the range of 10^{13} to 10^{14} W/cm^2, or the intensity reaches the value where the Kerr nonlinearity saturates, the important physical effects like self-focusing, plasma de-focusing etc., come into play. When a pulse with power exceeding the critical power for self-focusing, P_{cr}, propagates in gases, it supports a narrow coherent structure known as filaments. The filament is generated after the dynamical balance of the two counteracting physical effects namely focusing due to Kerr effect and defocusing due to plasma generated by multiphoton ionization. The filament has been observed in gases as air [83], in solids as silica glasses [84] and in liquids [85].

  Pulse propagation in the presence of competing nonlinearities has received much attention lately because competition between nonlinearities of different orders could lead to strong stabilization of pulse propagation [86]. Higher order nonlinearities must be considered if the optical pulse intensity is high or the nonlinear coefficients of the materials are large, for instance, in semiconductor doped glasses [86, 87]. One example of the effect of competing nonlinearities are the stabilization of vortices and vortex tori in cubic-quintic nonlinear media [88–

91]. In the constant dispersion case, the bright and dark solitons have been extensively investigated in the cubic-quintic nonlinear media [92, 93]. The bright and dark quasi solitons for the cubic-quintic nonlinearity have also been studied [94]. In recent years, a number of experiments reported the measurement of the cubic-quintic nonlinearity [95−99]. In this chapter, we investigate pedestal-free pulse compression of the chirped soliton pulse under the influence of cubic and quintic nonlinearities. Numerical results reveal that competing cubic-quintic nonlinearities can stabilize the pulse propagation and will lead to more robust pulse compression. As a special case, we also discuss chirped Townes solitons in pure quintic media, i.e. power law nonlinearity, and study the possibility of rapid pulse compression by wave collapse and exponentially decreasing dispersion. We note that the pure quintic nonlinearity aptly models the Tonks-Girardeau (TG) regime in Bose-Einstein condensation (BEC) [100, 101].

4.2 Theoretical Model

The cubic-quintic nonlinearity arises from a nonlinear correction to the refractive index of a medium in the form $\delta n = n_2 I + n_4 I^2 + ...$, where I is the light intensity and the coefficients n_2, n_4 determine the nonlinear response of the medium. The coefficients n_2 and n_4 are related to the third order $\chi^{(3)}$ and fifth order susceptibility $\chi^{(5)}$ through $n_2 = 3\chi^{(3)}/(8n_0)$ and $n_4 = 5\chi^{(5)}/(16n_0)$, where n_0 is the linear refractive index [102]. The nonlinear correction to the refractive index can also be investigated using other forms of nonlinearity of the medium: (i) the closed saturated form: $\delta n = n_2 I (1 + I/I_s)^{-1}$, where I_s is the saturation intensity [103]. For weak fields, $I/I_s \ll 1$, it yields the usual self-focusing Kerr response, $\delta n = n_2 I$. When the intensity increases, it is necessary to take higher order

nonlinearities into account; (ii) the exponential form: $\delta n = n_2 I_s \left[1 - \exp\left(-I / I_s \right) \right]$;

(iii) the form: $\delta n = n_2 I \left(2 + I / I_s \right) / \left(1 + I / I_s \right)$ [104]. In all three cases, expansion

of these three functions in powers of I and retaining second order terms yields a

cubic-quintic NLS equation in which the nonlinear coefficients are determined by

the choice of the form of the model function and the value of I_s. However, in

practice, there might not be functional relation between the coefficients n_2 and

n_4. For example, in semiconductor double-doped optical fibers [92, 105] the

doping of the silica glass with two appropriate semiconductor particles leads (in a

regime far from saturation) to the cubic-quintic form of the refractive index with

an effectively increased value of n_4 and a decreased one of n_2 (not related by any

expansion procedure). In other materials the value of n_2 and n_4 may also depend

on the doping or on the direction of light propagation. So, in a certain sense the

cubic-quintic description is more general. It can be adopted to any given material

and is preferable when considering real situations.

   Pulse propagation in a medium with cubic-quintic nonlinearities is governed by

the generalized cubic-quintic NLS (CQNLS) equation

$$i\frac{\partial E}{\partial z} - \frac{\beta(z)}{2}\frac{\partial^2 E}{\partial t^2} + \gamma(z)|E|^2 E - \delta(z)|E|^4 E - i\frac{g(z)}{2}E = 0, \tag{4.1}$$

where $E(z,t)$ is the slowly varying envelope of the axial electrical field, t is the

retarded time, z is the propagating distance, $\beta(z)$ is the group velocity dispersion

and $g(z)$ is the distributed gain or loss function. The cubic and quintic nonlinear

parameters are given by $\gamma = 2\pi n_2 / \left(\lambda_0 A_{eff} \right)$ and $\delta = -2\pi n_4 / \left(\lambda_0 A_{eff}^{\;2} \right)$, where λ_0 is

the central wavelength and A_{eff} is the effective area of the fiber. All the physical

parameters $\beta(z)$, $\gamma(z)$, $\delta(z)$ and $g(z)$ are functions of the propagation distance z.

We now investigate the chirped soliton solution of the CQNLS equation by self-similar analysis. We assume the complex function $E(z,t)$ in the form,

$$E(z,t) = Q(z,t)\exp\left[i\Phi(z,t)\right],$$ (4.2)

where Q and Φ are the amplitude and phase of the envelope function A respectively. In order to study the generation of chirped solitons of Eq. (4.1), we assume a quadratic phase given by

$$\Phi(z,t) = \alpha_1(z) + \frac{\alpha_2(z)}{2}(t-T_c)^2,$$ (4.3)

where $\alpha_1(z)$ and $\alpha_2(z)$ are functions of z and T_c is the center of the pulse. We assume that the amplitude depends on the scaling variable θ which is a combination of variables $(t-T_c)$ and some function $\Gamma(z)$ of the variable z. Since the self-similar solutions possess scaling structure, we represent the amplitude $Q(z,t)$ as

$$Q(z,t) = \frac{1}{\sqrt{\Gamma(z)}}R(\theta)\exp\left[\frac{G(z)}{2}\right].$$ (4.4)

The scaling variable θ and the function $G(z)$ are given by

$$\theta = \frac{t-T_c}{\Gamma(z)}, \quad G(z) = \int_0^z g(z')dz'.$$ (4.5)

Here $\Gamma(z)$ and $R(\theta)$ are some functions which have to be determined. We also assumed that $\Gamma(0) = 1$ without loss of generality. Substituting Eqs. (4.2) to (4.4) into Eq. (4.1), the quadratic phase coefficient $\alpha_2(z)$ and the function $\Gamma(z)$ are

found to be

$$\alpha_2(z) = \frac{\alpha_{20}}{1 - \alpha_{20}D(z)}, \Gamma(z) = 1 - \alpha_{20}D(z), \tag{4.6}$$

where $\alpha_{20} = \alpha_2(0) \neq 0$ because the phase is assumed to be a quadratic function of the variable $(t - T_c)$ and the cumulative dispersion function $D(z)$ is given by

$$D(z) = \int_0^z \beta(z')dz'. \tag{4.7}$$

In addition to the above conditions, we also find

$$\frac{d^2R}{d\theta^2} + \frac{2\Gamma^2}{\beta}\frac{d\alpha_1}{dz}R - \frac{2\Gamma\gamma}{\beta}\exp[G(z)]R^3 + \frac{2\delta}{\beta}\exp[2G(z)]R^5 = 0. \tag{4.8}$$

Note that the coefficients in Eq. (4.8) are functions of the variable z but the function $R(\theta)$ depends only on the scaling variable θ. Therefore, Eq. (4.8) possesses nontrivial solutions $[R(\theta) \neq 0]$ if and only if the coefficients in Eq. (4.8) are constants, i.e.

$$-\frac{2\Gamma^2(z)}{\beta(z)}\frac{d\alpha_1}{dz} = \lambda_1, \tag{4.9}$$

$$\frac{\Gamma(z)\gamma(z)}{\beta(z)}\exp[G(z)] = \lambda_2, \tag{4.10}$$

$$\frac{\delta(z)}{\beta(z)}\exp[2G(z)] = \lambda_3, \tag{4.11}$$

where λ_1, λ_2 and λ_3 are constants. Equations (4.9), (4.10), and (4.11) yield

$$\lambda_1 = -\frac{2}{\beta_0}\frac{d\alpha_1}{dz}\bigg|_{z=0}, \ \lambda_2 = \frac{\gamma_0}{\beta_0}, \ \lambda_3 = \frac{\delta_0}{\beta_0}, \tag{4.12}$$

because $\Gamma(0) = 1$ and $G(0) = 0$. The parameters $\beta_0 = \beta(0)$, $\gamma_0 = \gamma(0)$ and $\delta_0 = \delta(0)$. Thus for the nontrivial case, Eq. (4.8) can be written as

$$\frac{d^2 R}{d\theta^2} - \lambda_1 R + 2\lambda_2 R^3 + 2\lambda_3 R^5 = 0. \tag{4.13}$$

The solution of Eq. (4.9) is

$$\alpha_1(z) = \alpha_{10} - \frac{\lambda_1}{2} \int_0^z \frac{\beta(z')}{\left[1 - \alpha_{20} D(z')\right]^2} dz', \tag{4.14}$$

where α_{10} is an integration constant. Now we proceed to find the distributed gain function using Eqs. (4.9) and (4.10)

$$g(z) = \frac{1}{\eta(z)} \frac{d\eta}{dz} - \frac{\alpha_{20}\beta(z)}{\Gamma(z)}, \tag{4.15}$$

where we define the function $\zeta(z)$ as

$$\eta(z) = \frac{\gamma(z)}{\delta(z)}, \tag{4.16}$$

From Eqs. (4.10) and (4.11), the condition for the variation of the quintic nonlinear parameter is

$$\delta(z) = \frac{\gamma^2(z)\Gamma^2(z)}{\beta(z)} \frac{\lambda_3}{\lambda_2^2}. \tag{4.17}$$

Eqs. (4.6), (4.7), and (4.12)–(4.17) are the required conditions for the existence of self-similar solutions in Eqs. (4.2)–(4.5) of the generalized CQNLS equation with distributed coefficients, i.e. Eq. (4.1). We observed that for the self-similar solutions of Eq. (4.1), only two of the four parameters $\beta(z), \gamma(z), \delta(z)$ and $g(z)$ in Eq. (4.1) are free parameters. For example, if $\beta(z)$ and $\gamma(z)$ are chosen to be the free parameters, then $g(z)$ and $\delta(z)$ will be determined from Eqs. (4.15) and (4.17) respectively.

Different physical situations lead to different choices of the two free parameters. For example consider both the cubic and quintic nonlinear coefficients do not

114

vary with distance, i.e. both $\gamma(z)$ and $\delta(z)$ are constant. A self-similar solution to Eq. (4.1) exists if the dispersion and gain/loss vary in the form $\beta(z) = \beta_0 / (1 + \alpha_{20}\beta_0 z)^2$ and $g(z) = \alpha_{20}\beta_0 / (1 + \alpha_{20}\beta_0 z)$. If the cubic nonlinear parameter $\gamma(z)$ is constant and there is no gain/loss [$g(z) = 0$], then the dispersion and the quintic nonlinearity must vary exponentially, i.e. $\beta(z) = \beta_0 \exp(-\alpha_{20}\beta_0 z)$ and $\delta(z) = \delta_0 \exp(-\alpha_{20}\beta_0 z)$. In this case, the function $\Gamma(z) = \exp(-\alpha_{20}\beta_0 z)$. Thus from Eq. (4.5), the pulse width will vary exponentially as the dispersion $\beta(z)$. Since we are interested in pedestal-free compression of optical pulses, we will focus on the soliton solutions to the CQNLS equation with exponentially varying dispersion in Section 4.3. Another special case is pure quintic nonlinearity with no gain/loss, i.e. $\gamma(z) = g(z) = 0$. From Eq. (4.11), the quintic nonlinearity $\delta(z)$ is then directly proportional to the dispersion $\beta(z)$ which can take any functional form. We will study this special case in Section 4.4.

4.3   Chirped Self-Similar Bright Solitons in the Anomalous and Normal Dispersion Regimes

In this section, we assume that cubic nonlinear parameter $\gamma(z)$ is constant and there is no gain or loss i.e. $g(z) = 0$. The dispersion and the quintic nonlinearity therefore vary exponentially as $\beta(z) = \beta_0 \exp(-\alpha_{20}\beta_0 z)$ and $\delta(z) = \delta_0 \exp(-\alpha_{20}\beta_0 z)$. From Section 4.2, the phase and amplitude of the self-similar solutions of the generalized CQNLS equation with distributed coefficients are given by Eqs. (4.3) and (4.4). We determine the amplitude of the bright

115

solitary wave by integrating Eq. (4.13) and obtain

$$E(z,t) = \frac{1}{T_0\left[1-\alpha_{20}D(z)\right]} \left\{ \frac{\mp 2\rho_1}{\sqrt{1+\dfrac{8\rho_1^2}{3\rho_2 T_0^2\left[1-\alpha_{20}D(z)\right]^2}}\cosh\left(2\dfrac{t-T_c}{T_0\left[1-\alpha_{20}D(z)\right]}\right)\pm 1} \right\}^{1/2} \exp(i\Phi),$$

(4.18)

where $\rho_1(z) = \beta(z)/\gamma(z)$ and $\rho_2(z) = \beta(z)/\delta(z)$. The integration constant λ_1 is chosen to be $1/T_0^2$, where T_0 is the initial pulse width. The upper signs in Eq. (4.18) correspond to the soliton in the anomalous dispersion regime while the lower signs correspond to that in the normal dispersion regime. In the anomalous dispersion regime, the following physical conditions, $\beta < 0, \quad \gamma > 0, \quad \delta > 0$ (competing cubic-quintic nonlinearity) or $\beta < 0, \quad \gamma > 0, \quad \delta < 0$ (cooperating cubic-quintic nonlinearities) should be maintained for the existence of soliton. Similarly, $\beta > 0, \quad \gamma > 0, \quad \delta > 0$ (competing cubic-quintic nonlinearity) has to be valid for the soliton in the normal dispersion regime. Equation (4.18) is a linearly chirped self-similar bright solitary pulse since it propagates in a self-similar manner in a fiber medium under the influence of cubic-quintic nonlinearity. In a semiconductor double-doped optical fiber, self-similar solitons in both normal and anomalous dispersion regimes are possible depending on the doping materials, the operating frequency, and the optical pulse intensities [93].

4.3.1 Length Scales

Unlike the conventional soliton in Kerr media, where the dispersion and nonlinear lengths are proportional to each other, we found that the dispersion, cubic and quintic nonlinear lengths for the self-similar solitons in a CQ medium follow a harmonic relationship

116

$$\frac{2\,\text{sgn}(\delta)}{3L_{n4}(z)} - \frac{\text{sgn}(\gamma)}{L_{n2}(z)} - \frac{\text{sgn}(\beta)}{L_D(z)} = 0, \tag{4.19}$$

where the dispersion [$L_D(z)$], cubic [$L_{n2}(z)$] and quintic [$L_{n4}(z)$] nonlinear

lengths are given by

$$L_D(z) = \frac{T_0^2 \Gamma^2(z)}{|\beta(z)|}, \quad L_{n2}(z) = \frac{1}{|\gamma(z)|P_0(z)}, \quad L_{n4}(z) = \frac{1}{|\delta(z)|P_0^2(z)}. \tag{4.20}$$

Here $P_0 = |E_{max}|^2$ is the peak power of the chirped soliton, where E_{max} is the

maximum amplitude [which is given in Eq. (4.23)]. Note that all the three length

scales vary with distance because the coefficients of the CQNLS equation depend

on distance. We note that when the quintic nonlinearity is switched off i.e.

$L_{n4} \to \infty$, Eq. (4.19) is reduced to the well-known condition $L_D = L_{n2}$ for soliton

formation in Kerr media. In this case, the linearly chirped bright soliton in Eq.

(4.18) will be reduced to the the chirped soliton solution for Kerr nonlinearity [26,

27].

From Eq. (4.18), the energy of the chirped bright soliton is calculated as

$$W = \int_{-\infty}^{\infty} |E|^2 dt = -\frac{2\rho_1(z)}{T_0\Gamma\sqrt{1-b^2}} \ln\frac{1+\sqrt{1-b^2}}{b}, \quad (b < 1) \tag{4.21}$$

$$W = \int_{-\infty}^{\infty} |E|^2 dt = \mp\frac{2\rho_1(z)}{T_0\Gamma\sqrt{b^2-1}}\left[\frac{\pi}{2} \mp \sin^{-1}(1/b)\right], \quad (b > 1) \tag{4.22}$$

where $b = \sqrt{1 + 8\lambda_3/(3\lambda_2^2 T_0^2)}$ is a constant. In terms of length scales, the

parameter b can also be written as $b = \sqrt{1 + \frac{4L_{n2}(z)}{L_D(z)^2}\left[\text{sgn}(\beta\cdot\gamma)L_D(z) + L_{n2}(z)\right]}$.

Equation (4.21) represents the energy of the soliton in the anomalous dispersion

regime when $b < 1$. The upper sign in Eq. (4.22) corresponds to the soliton energy

in the anomalous dispersion regime when $b > 1$. The lower sign corresponds to the soliton energy in the normal dispersion regime for all values of $b > 0$. The condition $b > 1 \ (< 1)$ corresponds to $\delta_0 / \beta_0 > 0 (< 0)$. For optical fibers, the cubic nonlinear coefficient $\gamma > 0$. Thus in the anomalous dispersion regime, the condition $b > 1$ means $\delta < 0$ representing cooperating cubic-quintic nonlinearities, whereby the effect of dispersion is balanced by the cubic and quintic nonlinearities. The other condition $b < 1$ means $\delta > 0$ representing the competing cubic-quintic nonlinearities, wherein the effect of cubic nonlinearity is balanced by that of dispersion and quintic nonlinearity. The condition $b = 1$ is not of interest because it corresponds to $L_D(z) = L_{n2}(z)$ which is possible only if $L_{n4} \to \infty$, i.e. $\delta = 0$. In the normal dispersion regime, normally $b > 1$ because $\mathrm{sgn}(\gamma) > 0$. Thus, in the anomalous dispersion regime, the parameter b determines whether the nonlinearities are cooperating or competing.

We find that the soliton solution in the anomalous regime will approach the chirped soliton solution reported in [26, 27] when the coefficient of the quintic nonlinearity approaches zero $(\delta \to 0)$. However, the energy of Eq. (4.22) goes to infinity when $\delta \to 0 \ (\lambda_3 \to 0)$. Thus, the quintic nonlinearity is crucial to the formation of chirped solitons in the normal dispersion regime. Similarly, the peak intensity and FWHM are given by

$$\left(E^2\right)_{\max} = \mp \frac{1}{T_0^2 \Gamma^2} \frac{2\rho_1(z)}{b \pm 1}, \tag{4.23}$$

$$\Delta t = T_0 \Gamma \ln\left[2 \pm y + \sqrt{(2 \pm y)^2 - 1}\right], \tag{4.24}$$

where $y = 1/b$. The upper signs in Eqs. (4.23) and (4.24) correspond to the peak intensity and the pulse width of soliton in the anomalous dispersion regime while

the lower signs correspond to that in the normal dispersion regime.

Note that the Eq. (4.24) represents the FWHM of the chirped soliton pulse after the compression process. Further from the same relation, as we know the initial and final width of the pulse, one can easily determine the pulse compression factor with the following relation

$$\frac{T_0}{\Delta t} = \left\{ \Gamma \ln \left[2 + y + \sqrt{\left(2 \pm y\right)^2 - 1} \right] \right\}^{-1}. \tag{4.25}$$

4.3.2   Stability of the Chirped Soliton

Strictly speaking, the localized solution given in Eq. (4.18) is not a soliton, but rather a solitary wave. It is therefore crucial to determine the stability of the solution. Ideally, analytical techniques such as the Vakhitov-Kolokolv (VK) criterion should be used to determine the stability of the solitary waves [106]. The VK criterion has been well established for the constant coefficient NLS-type equations (for both cubic and cubic and quintic nonlinearities). However, mathematically the VK criterion is applicable to the ground states of NLS-type equations only. Thus, the VK criterion cannot be applied to analyze the stability of the chirped soliton given in Eq. (4.18). As a result, we have to resort to using numerical simulation to determine the stability of the chirped solitons. From extensive numerical simulations, we find that the chirped soliton in the anomalous dispersion regime is stable whereas that in the normal dispersion regime is unstable (for details see Section 4.3.3). Therefore, hereafter, we focus on pulse compression in the anomalous dispersion regime only.

Before we leave this subsection, we would like to illustrate the relationship between the three length scales discussed in Section 4.3.1. We consider the case in which the cubic nonlinearity $\gamma = $ constant and gain or loss $g\left(z\right) = 0$. Thus the

dispersion and the quintic nonlinearity parameters are given by

$$\beta(z) = \beta_0 \exp(-\sigma z), \quad \delta(z) = \delta_0 \exp(-\sigma z), \tag{4.26}$$

where $\beta_0 < 0, \delta_0 > 0$ and $\sigma = \alpha_{20}\beta_0 > 0$ for dispersion decreasing fibers. As an example of pulse compression, we consider a semiconductor-doped (chalcogenideAS$_2$Se$_3$) fiber of length L = 400 m. The effective mode area of the fiber is assumed to be 10 μm^2. The cubic and quintic nonlinear coefficients are assumed to be $\gamma_0 = 0.2362$ /W/m and $\delta_0 = 0.4724$ /W^2/m, respectively. The initial GVD β_0 is chosen to be -0.5 ps^2/m. The other parameters chosen are $T_0 =$ 5 ps, $\sigma = 0.005$/m, $\alpha_{20} = -0.01$ THz^2 and $g = 0$. Figure 4.1(a) plots the variation of dispersion, cubic and quintic nonlinearly length for a soliton solution. From Fig. 4.1(a), in the beginning of compression, the cubic nonlinear length and the dispersion length dominate. As the pulse propagates and compresses, its peak intensity increases, hence the quintic nonlinear length decreases and becomes comparable to the dispersion length and the cubic nonlinear length. Figure 4.1(b) shows the compression of the bright soliton under the influence of the competing cubic-quintic nonlinearities. The compression factor of the above fiber is found to be 7.39. We also numerically integrated Eq. (4.1) using the exact soliton solution as the initial condition. The numerical results agree very well with the analytic solution as illustrated in Fig. 4.1(b).

4.3.3 Perturbations in the Input Peak Power and Chirp

Since Eq. (4.1) is not integrable, for optical compression application it is necessary to study the effects of perturbations on evolution of the solitary wave solution given in Eq. (4.18). In the following, we investigate the effect of perturbations of the initial peak power and initial chirp on the pulse evolution.
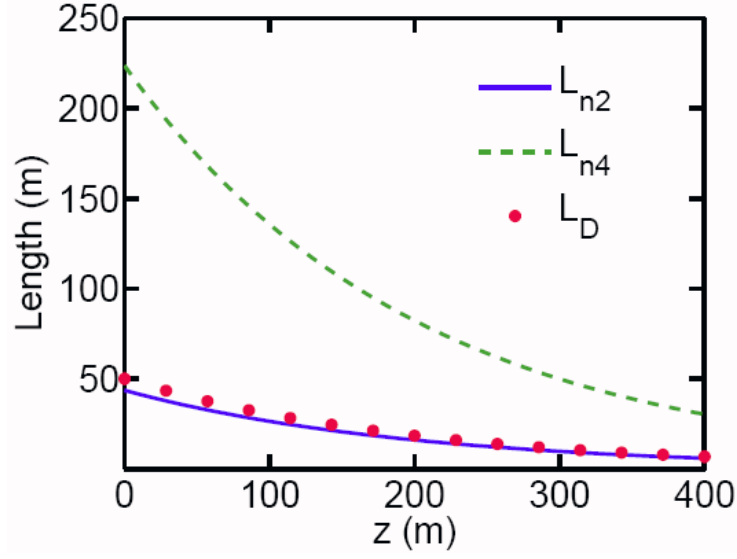
(a)
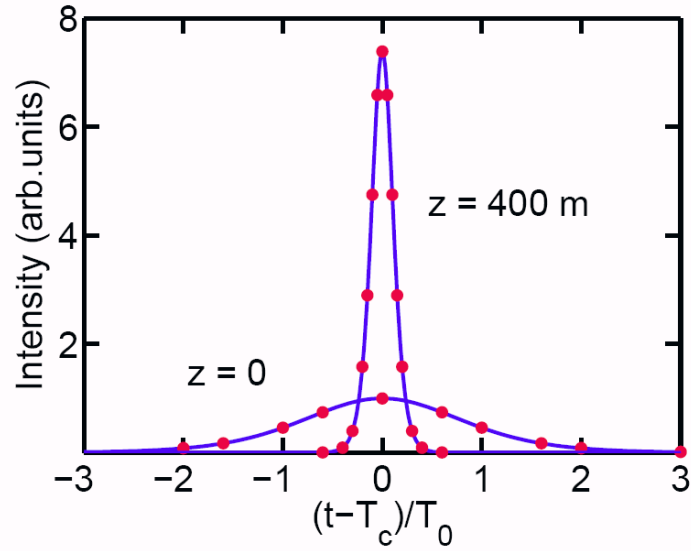
(b)

Figure 4.1: (a) Variation of the dispersion length (dots), cubic nonlinear length (solid curve) and quintic nonlinear length (dashed curve) for a chirped soliton in a cubic-quintic nonlinear medium. The physical parameters are: $T_0 = 5$ ps, $\alpha_{20} = -0.01$ THz^2, $\beta_0 = -0.5$ ps^2/m, $\sigma = 0.005$ /m, $\gamma_0 = 0.2362$ /W/m, $\delta_0 = 0.4724$ /W^2/m, $g = 0$ and $z = 400$ m. (b) Compression of a chirped bright soliton pulse. The dots and solid curve represent analytical and numerical results respectively.

First, we consider variations in the initial peak power and initial chirp and study the corresponding changes in peak power and chirp. We determined the quality of the compressed pulse by monitoring the pedestal generated and the compression factor when the initial pulse is perturbed. Figure 4.2 shows the deviations in peak power and chirp coefficient at $L = 400$ m from the analytic solution when the input peak power deviates from the ideal peak power from -20% to $+20\%$ but the pulse width of the solitary pulse remained unchanged. The choice of fiber and pulse parameters is the same as that in Fig. 4.1. The dots represent results for competing cubic-quintic nonlinearities, circles represent the results for cooperating cubic-quintic nonlinearity, and crosses represent the results for pure cubic nonlinearity.

Figure 4.2(a) shows that the deviation of the peak power from the ideal solution is smallest for the case of competing cubic-quintic nonlinearities and largest for cooperating cubic-quintic nonlinearities. Here it should be emphasized that the larger deviation in the latter case is owing to the beam collapse which occurs in the case of cooperating cubic-quintic nonlinearities. In Fig. 4.2(a), the deviation in peak power under different perturbations of initial peak power has been calculated with the following expression $(P_{\text{perturbed}} - P_{\text{ideal}}) / P_{\text{ideal}} \times 100\%$. From Fig. 4.2(b), the same observation holds for the deviations of the chirp parameter, but the variations in the chirp parameter is more sensitive to the perturbation. Here, the chirp of the perturbed solitary pulse is measured by carrying out a polynomial fit of the phase. From the polynomial fitting, the chirp remains close to the quadratic chirp since the chirp contributed by all higher order terms are very small. Based on the numerical results, the soliton solutions in competing cubic quintic nonlinearities are more robust to perturbations. The amount of pedestal

122

generated during pulse compression is an important parameter characterizing the quality of the compressed pulses. The pedestal energy is defined as the relative difference between the total energy of the transmitted pulse and the energy of a hyperbolic-secant pulse having the same peak power and width as those of the transmitted pulse, i.e. pedestal energy(%) = ($E_{\mathrm{perturbed}} - E_{\mathrm{CQ}}$) / $E_{\mathrm{perturbed}} \times 100\%$. Here, $E_{\mathrm{perturbed}}$ is the energy of the perturbed pulse. Note that the energy of a hyperbolic-secant type pulse E_{CQ} in the CQ media is calculated using curve fitting to obtain the best fit from the data. We use the function $|E|^2 = \zeta_1 / \left[\zeta_2 \cosh\left(2\chi / \zeta_3\right) + 1 \right]$ to fit the intensity of the hyperbolic secant type pulse, where the values of the parameters ζ_1, ζ_2 and ζ_3 are determined by the curve fitting. Figure 4.2(c) shows the amount of pedestal generated for the corresponding perturbation in initial peak power. The results show that competing cubic-quintic nonlinearities generate only small amount of pedestal energy comparing to cooperating cubic-quintic nonlinearities and pure cubic nonlinearity. However, the amounts of pedestal generated in all three cases are very small. Even in the worst case in which the initial peak power is only 80% of the ideal value for cooperating nonlinearities, the pedestal energy is only 1.6%. Figure 4.2(d) shows the compression factor for the corresponding perturbation in the peak power for all the three cases. As expected, the compression factor is the highest for cooperating cubic-quintic nonlinearities and the lowest for the competing case. Thus the pulse compressor using competing nonlinearities are more robust to perturbation of the input pulse parameters at the expense of the compression factor.

Figures 4.3(a) and (b), respectively, show the deviation in peak power and the chirp when the initial chirp of the input pulse deviates from the ideal value.
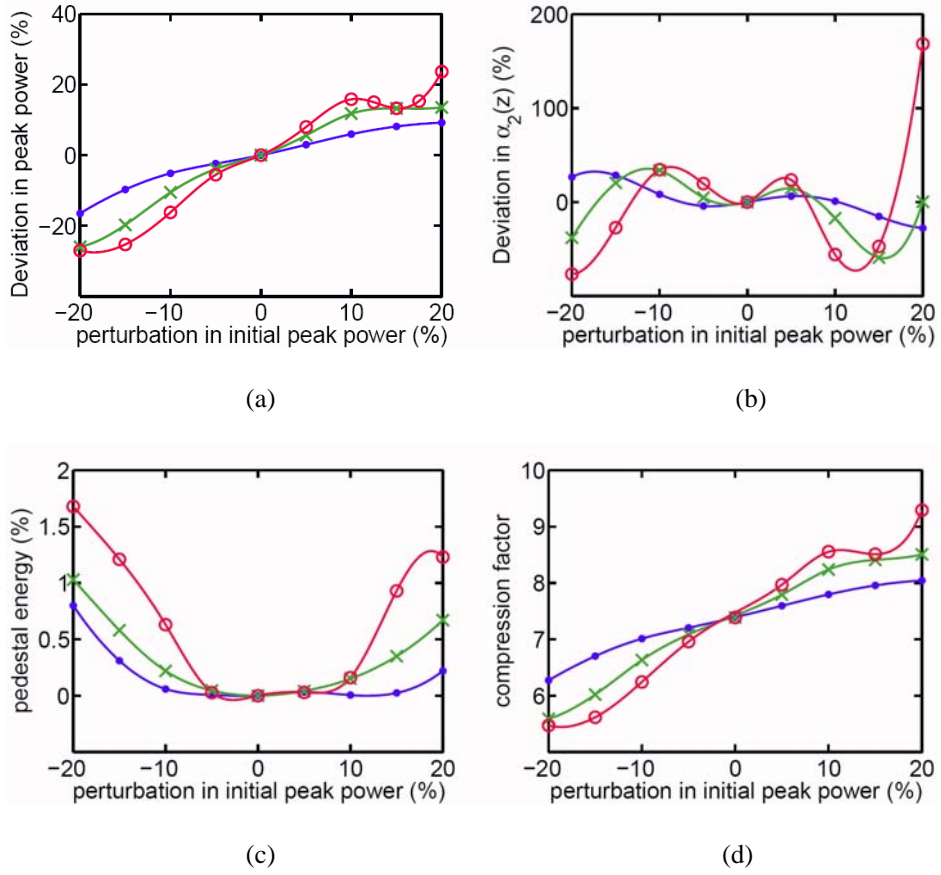
Figure 4.2: (a) Deviations of the peak power from the exact solution, (b) the chirp coefficient, (c) the pedestal energy, and (d) the compression factor at $L = 400$ m when the input peak power deviates from the ideal peak power from -20% to $+20\%$. The physical parameters are same as those in Fig 4.1. The dots represent results for competing cubic- quintic nonlinearities ($\delta_0 = 0.4724$ /W^2/m), circles represent results for cooperating cubic- quintic nonlinearities ($\delta_0 = -0.4724$ /W^2/m), and crosses represent results for pure cubic nonlinearity ($\delta_0 = 0$).

Unlike the perturbations in peak power, the deviations in peak power are small and are very similar for the three different cases. Again, the deviation of the chirp value is the smallest for competing cubic-quintic nonlinearities and the largest for cooperating case. Figures 4.3(c) and (d) show the pedestal energy and compression factor, respectively, for the corresponding perturbations in the initial chirp. The pedestal energy generated in all three cases is only a fraction of one percent. The deviations in compression factor are small and similar for all the three cases. Thus the soliton is very robust to perturbation in the initial chirp in all three cases.

We have carried out extensive numerical simulations on the perturbations of initial power and initial chirp by varying the decay rate of dispersion and changing the strength of quintic nonlinearity. In all cases we have studied, we find that the compressed pulse in the case of competing nonlinearities has the smallest deviations in peak power and chirp. The pedestal energy is also the smallest but the compression factor is also the smallest when compared to the case of pure cubic nonlinearity and cooperating cubic-quintic nonlinearities. Figure 4.4 shows the evolution of the (a) peak power, (b) chirp, (c) pedestal energy and (d) compression factor when the peak power of the initial solution is +20% larger than the ideal solution given in Eq. (4.21) for competing cubic-quintic nonlinearities and Eq. (4.22) for cooperating cubic-quintic nonlinearities. The distance traveled is 400 m. The parameter L_{D0} is the initial dispersion length as $z = 0$. The dashed curve represents the soliton solution of the CQNLS equation. The dots represent perturbation results for competing cubic-quintic nonlinearities, the circles represent that for cooperating cubic-quintic nonlinearities, and the crosses represent that for pure cubic nonlinearity. From Fig. 4.4(a), (b), (c) and

(a)
(b)
(c)
(d)
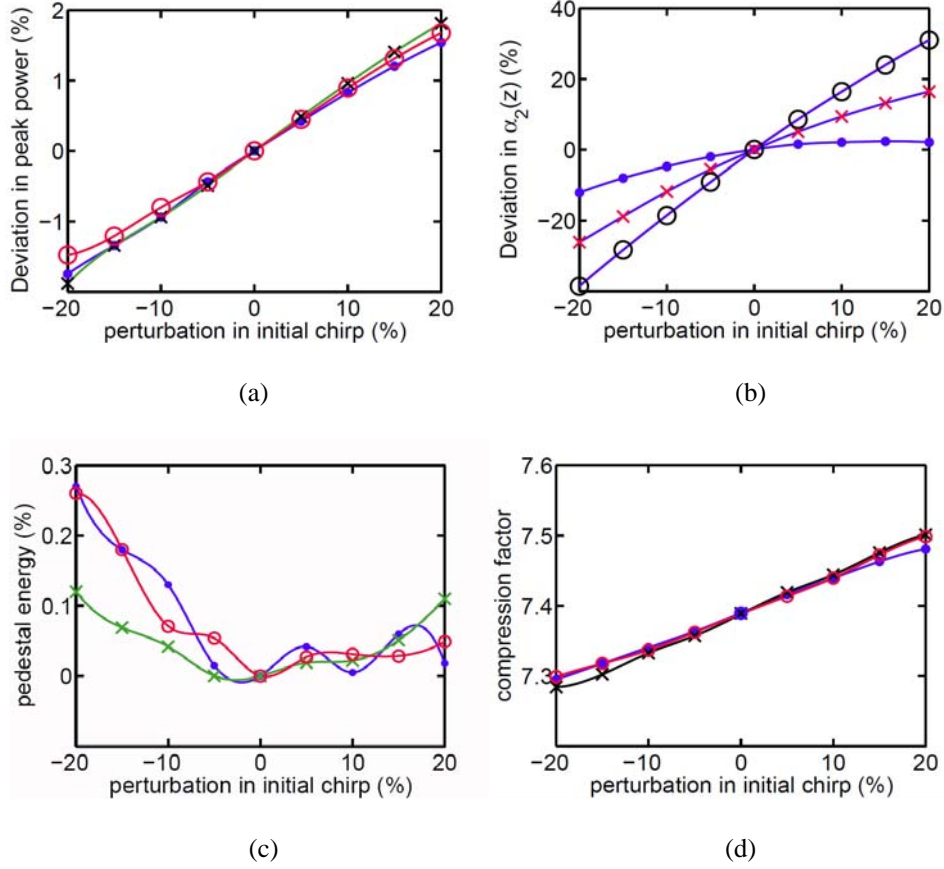
Figure 4.3: (a) Deviations of the peak power from the exact solution, (b) the chirp coefficient, (c) the pedestal energy, and (d) the compression factor at $L = 400$ m when the initial chirp deviates from the chirp value of the exact solution from -20% to $+20\%$. The physical parameters are same as those in Fig 4.2. The dots represent results for competing cubic and quintic nonlinearities ($\delta_0 = 0.4724$ /W^2/m), circles represent results for cooperating cubic and quintic nonlinearities ($\delta_0 = -0.4724$ /W^2/m), and crosses represent results for pure cubic nonlinearity ($\delta_0 = 0$).
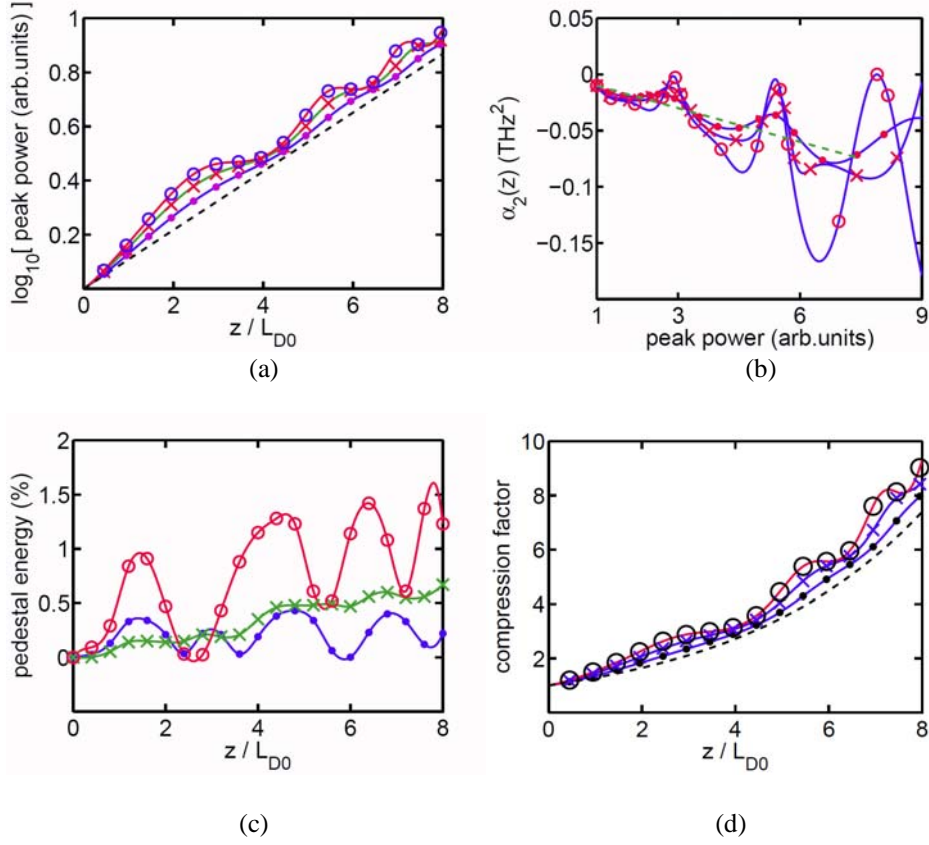
Figure 4.4: Evolution of the (a) peak power, (b) chirp, (c) pedestal energy, and (d) compression factor when the initial peak power deviates +20% from the ideal peak power when distance varies from 0 to 400 m for the same physical parameters used in Fig 4.1. The parameter L_{D0} is the initial dispersion length. The dashed curve represents results for the exact solution, dots represent results for competing cubic-quintic nonlinearities ($\delta_0 = 0.4724$ /W^2/m), circles represent results for cooperating cubic-quintic nonlinearities ($\delta_0 = -0.4724$ /W^2/m), and crosses represent results for pure cubic nonlinearity ($\delta_0 = 0$).

127

(d), the peak power, chirp, pedestal and compression factor of the solitary pulse undergo periodic oscillations during the evolution. We note that the oscillation periods are different for the three different cases. Without quintic nonlinearity and for the constant dispersion, the oscillation has a period of $8z_0$ for soliton where $z_0 \left(= \pi L_D / 2 \right)$ is the soliton period, because of the resonance of the perturbation with the soliton wavevector $2\pi / \left(8z_0 \right)$ [107].

In what follows, for the completeness of the investigation, we predict the oscillations exhibited by the peak power and pulse width during the evolution. Figure 4.5(a) represents the behavior of change in peak power $\Delta P = P_{\text{perturbed}} - P_{\text{ideal}}$ along the propagation direction when the initial peak power deviates from the peak power from -20% to $+20\%$. We have halved the dispersion decay rate and doubled the pulse propagation distance in Fig. 4.5(a) when compared to that used in Fig. 4.3 in order to observe more oscillations. For Fig. 4.5(a), the solid curve represents the competing cubic-quintic nonlinearities, the dashed curve represents the cooperating cubic-quintic nonlinearities, and the dot-dashed curve represents the pure cubic nonlinearity. From Fig. 4.5(a), the deviation ΔP is the smallest for the competing cubic-quintic nonlinearities case. Figure 4.5(b) shows that the period of oscillations decreases exponentially along the propagation direction. The solid curve represents exponential fits for the three different cases. The rate of change of the period is found to be 0.002474/m for the competing cubic-quintic nonlinearities (dots), 0.002716/m for the cooperating cubic-quintic nonlinearities (circles), and 0.002637/m for pure cubic nonlinearity (crosses). All three decay rates for the three different cases are close to the decay rate of the dispersion which is 0.0025/m. Thus, the period of oscillation decreases exponentially as the

(a)	(b)
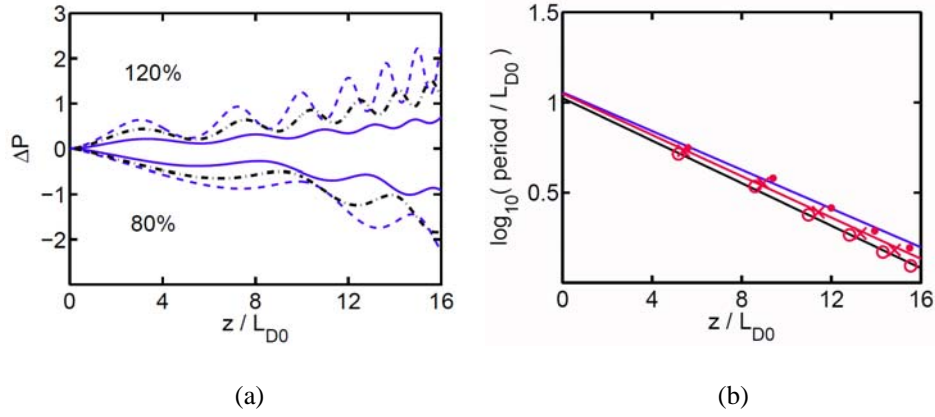
Figure 4.5: (a) Evolution of $\Delta P = P_{\text{perturbed}} - P_{\text{ideal}}$ along the propagation direction. The solid curve represents results for competing cubic-quintic nonlinearities ($\delta_0 = 0.4724$ /W^2/m), dashed curve represents results for cooperating cubic-quintic nonlinearities ($\delta_0 = -0.4724$ /W^2/m), dot-dashed curve represents results for pure cubic nonlinearity ($\delta_0 = 0$). The physical parameters are $T_0 = 5$ ps, $\alpha_{20} = -0.005$ THz^2, $\beta_0 = -0.5$ ps^2/m, $\sigma = 0.0025$ /m, $\gamma_0 = 0.2362$ /W/m, $g = 0$ and $z = 800$ m. (b) Variation of the oscillation periods along the propagation direction. The dots represent results for competing cubic-quintic nonlinearities ($\delta_0 = 0.4724$/W^2/m), circles represent results for cooperating cubic-quintic nonlinearities ($\delta_0 = -0.4724$/W^2/m), crosses represent results for pure cubic nonlinearity ($\delta_0 = 0$). The solid curve represents exponential fittings for the three different cases.

dispersion decreases along the propagation direction. The oscillations in ΔP represent a gradual adjustment towards ideal pulse shape under investigation. Figure 4.6 shows curve fitting of the evolution of ΔP for competing cubic-quintic nonlinearities with the function $f(\xi) = c_1 \exp(c_2\xi) + c_3 \exp(c_4\xi) \sin[c_5\exp(c_6\xi)]$, where $\xi = z / L_{D0}$, L_{D0} is the initial dispersion length and c_i, $i = 1,\ldots,6$ are constants. The solid curve represents the simulation results of the evolution of ΔP for competing cubic and quintic nonlinearities when the initial peak power is 20% larger than that of the ideal solution. The dashed curve represents the curve fitting results using the method of steepest descent where $c_1 = 0.0917$, $c_2 = 0.1238$, $c_3 = 0.08$, $c_4 = -0.0177$, $c_5 = -7.6532$ and $c_6 = 0.1043$. It is obvious that ΔP oscillates along a exponential function, whose increasing rate (c_2) almost equals to the decay of exponentially decreasing dispersion (0.125). The evolution of ΔP agrees with the fitting fuction very well.

Figure 4.7 shows the evolution of the (a) peak power, (b) chirp, (c) pedestal energy and (d) compression factor when the initial chirp is +20% larger than that of the ideal solution. The dashed curve represents the soliton solution of the CQNLS equation. The dots represent perturbation results for competing cubic-quintic nonlinearities, the circles represent that for cooperating cubic-quintic nonlinearities, and the crosses represent that for pure cubic nonlinearity. We observe that the peak power and the compression factor (pulse width) of the solitary pulse undergo only very small periodic oscillations. The deviations in peak power and compression factor are very small. The pedestal energy undergoes relatively larger periodic oscillations during the evolution but the magnitude of the variation is smaller than that for the perturbation in the peak
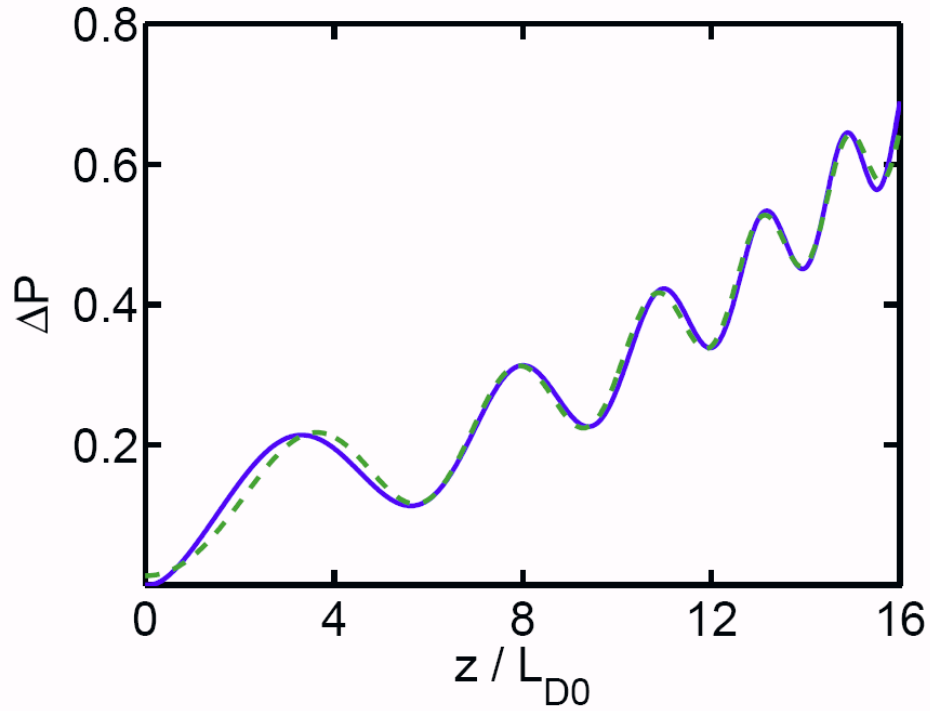
Figure 4.6: Curve fitting the evolution of ΔP for competing cubic and quintic nonlinearities by the function $f(\xi) = c_1\exp(c_2\xi) + c_3\exp(c_4\xi)\sin[c_5\exp(c_6\xi)]$, where $\xi = z/L_{D0}$ and c_i, $i=1, \ldots,$ 6 are constants. The solid curve represents the simulation results of the evolution of ΔP for competing cubic-quintic nonlinearities when the initial peak power deviates $+20\%$ from the ideal value. The dashed curve represents the fitting results using the method of steepest descent where $c_1 = 0.0917$, $c_2 = 0.1238$, $c_3 = 0.08$, $c_4 = -0.0177$, $c_5 = -7.6532$ and $c_6 = 0.1043$, and the dashed curve represents the results for the fitting function.

(a)

(b)

(c)

(d)
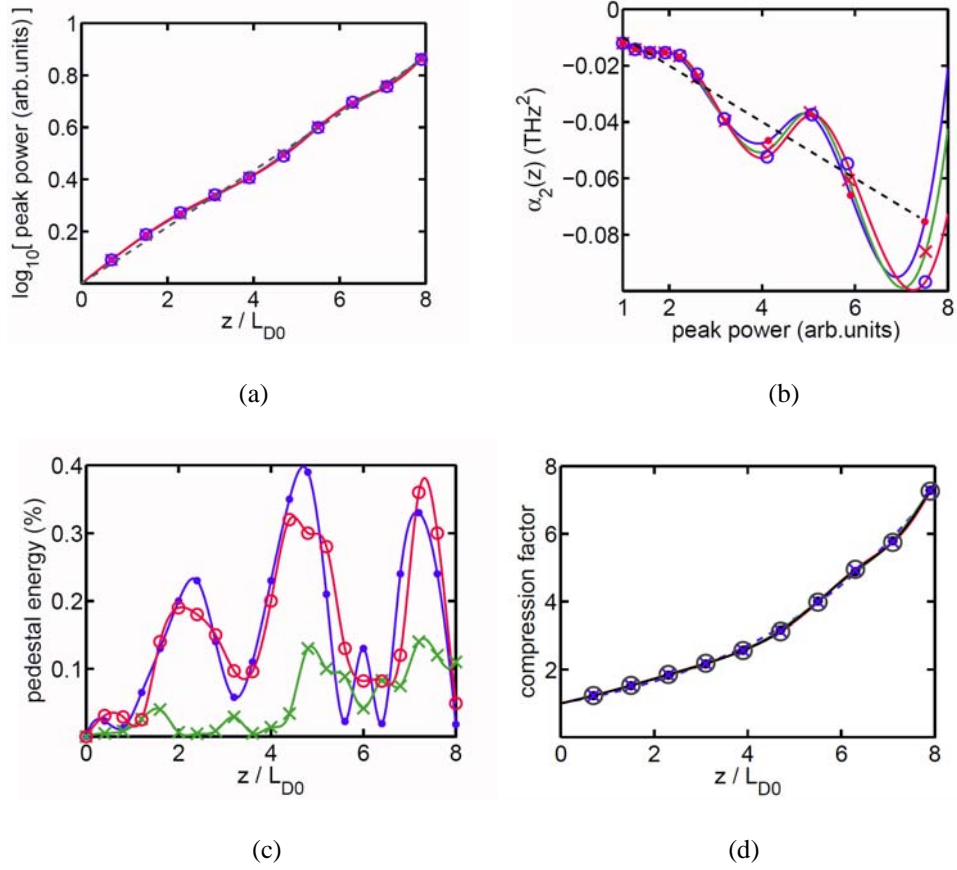
Figure 4.7: Evolution of the (a) peak power, (b) chirp, (c) pedestal energy, and (d) compression factor when the initial chirp deviates +20% from the exact chirp when the distance varies from 0 to 400 m for the same physical parameters in Fig 4.1. The dashed curve represents results for the exact solution, dots represent results for competing cubic- quintic nonlinearities ($\delta_0 = 0.4724$ /W^2/m), circles represent results for cooperating cubic- quintic nonlinearities ($\delta_0 = -0.4724$ /W^2/m), and crosses represent results for pure cubic nonlinearity ($\delta_0 = 0$).

power.

4.4   Chirped Self-Similar Townes Soliton

From the previous section, the soliton solution in the normal dispersion regime of the CQNLS equation with exponentially varying dispersion is unstable. Further, in the absence of quintic nonlinearity, the combination of cubic nonlinearity and normal dispersion, exponentially varying or not, does not support soliton solutions. However, pure quintic nonlinear medium does support soliton solution known as the quintic Townes solitons which are discovered for the two-dimensional NLS equation in nonlinear optics and describe the collapsing and dispersing of optical pulses [108]. Pulse propagation in a pure quintic NLS (QNLS) equation with distributed dispersion and distributed linear gain is given by

$$i\frac{\partial E}{\partial z} - \frac{\beta(z)}{2}\frac{\partial^2 E}{\partial t^2} - \delta(z)|E|^4 E - i\frac{g(z)}{2}E = 0. \tag{4.27}$$

Equation (4.27) describes nonlinear pulse propagation in many fields of nonlinear science, for example, in the nonlinear optics under the power law nonlinearity. It is known that physically, various materials, including semiconductors, exhibit power law nonlinearity. Spatial solitons have been investigated in media that have a power-law dependence on the intensity I^q for continuum values of q (where I being the intensity) [109−111]. However, in general, it may be difficult to find suitable nonlinear optical media which exhibit pure quintic nonlinearity because manipulation of the magnitude and the sign of nonlinearity is not easy. However, the QNLS equation aptly models the BECs especially in the TG regime. Experimental generation of such a gas had also been reported [100]. Recently, it has been shown that the magnitude as well as the sign of nonlinearity, which is

determined by the interactions between atoms in the condensate, could be manipulated by varying the external magnetic field near the Feshbach resonance [101]. Therefore, it is physically relevant to discuss the chirped Townes soliton in the BECs. The formation of soliton in BEC is similar to nonlinear optics, where the bright and dark solitons are supported by the focusing and defocusing nonlinearity, respectively, whereas in BECs, s-wave scattering interaction between atoms actually determines the soliton formation. Thus, bright and dark solitons are found in condensates with attractive and repulsive interactions. We now discuss the generation of chirped Townes soliton in the pure quintic media. The complex envelope of the chirped Townes soliton is obtained by applying the following physical condition $\beta(z) < 0$ and $\delta(z) < 0$ in Eq. (4.27).

$$E(z,t) = \frac{1}{T_0 \left[1 - \alpha_{20} D(z) \right]} \left\{ \frac{|\beta(z)|}{\sqrt{2\delta(0)\beta(0)/3/T_0^2}} \operatorname{sech} \left(\frac{2(t - T_c)}{T_0 \left[1 - \alpha_{20} D(z) \right]} \right) \right\}^{1/2} \exp(i\Phi).$$

(4.28)

The relation between the dispersion length and the quintic nonlinear length is $2L_D / 3 = L_{n4.}$ The energy and peak intensity of the chirped Townes soliton are given by

$$W = \frac{\sqrt{3}\pi |\beta(z)|}{\left[1 - \alpha_{20} D(z) \right] \sqrt{8\delta(0)\beta(0)}},$$

(4.29)

$$E_{\max}{}^2 = \frac{\sqrt{3} |\beta(z)|}{T_0 \left[1 - \alpha_{20} D(z) \right]^2 \sqrt{2\delta(0)\beta(0)}}.$$

(4.30)

We then proceed to investigate the stability of the chirped Townes soliton. For the constant coefficient case, it has been demonstrated that the Townes soliton is marginally stable in homogeneous media ($g = 0$) according to VK criterion. As has been discussed in Section 4.3.2, VK criterion does not apply to the chirped

Townes soliton in Eq. (4.28). However, unlike Section 4.3.2, it is not possible to numerically establish that a solution is marginally stable. We would try to infer the character of the solution in Eq. (4.28) by numerically studying the evolution of inputs with amplitude above and below that of the solution. First we study the evolution of analytic chirped Townes soliton. Figure 4.8 plots the evolution of analytic chirped Townes soliton solutions for constant (solid curve $\beta_0 = -0.5$ ps^2/m), exponentially increasing (dot-dashed curve $\sigma = -0.005$ /m), and exponentially decreasing (dashed curve $\sigma = 0.005$ /m) dispersions. The dots represent the results obtained by dint numerical simulation. Note that the analytical results are in good agreement with the results obtained by numerical simulation for the distance simulated.

So far, we have discussed the conventional pulse compression technique whereby we utilized the cubic nonlinearity and dispersion to achieve pulse compression. A non-conventional pulse compression technique based on the wave collapse phenomenon has been reported [112]. It is well established that the pure quintic model exhibits collapse [113]. However, the occurrence of collapse could either be arrested or postponed by physical effects like damping, nonlinearity saturation etc [114, 115]. Recently, it has been shown that the quintic damping effect, which arises from the three body interaction of an imaginary component, and cubic nonlinearity management help to arrest/suppress the occurrence of collapse [114].

Figure 4.9 shows the deviations of peak power from the exact Townes soliton when the input peak power deviates from the ideal peak power by (a) -5% and (b)$+5\%$ for constant dispersion (solid curve), exponentially decreasing dispersion (dashed curve), and exponentially increasing dispersion (dot-dashed curve). The

135

physical parameters used here are the same as those in Fig. 4.8. For constant dispersion (solid curve), the pulse disperses because the input power is less than the critical power as shown in Fig. 4.8(a). When the dispersion increases exponentially (dot-dashed curve), the self-similar effect and the wave collapse act together to broaden the pulse. Thus the pulse undergoes fast broadening. When the dispersion decreases exponentially (dashed curve), the self-similar effect and the collapse act in opposite. Thus the pulse initially compresses slightly as the self-similar effect dominates but eventually the wave collapse effect takes over. The self-similar compression in the exponentially decreasing dispersion can be used to postpone the wave dispersion in pure quintic media.

Similarly, when the dispersion is constant, the pulse undergoes collapse when the input peak power is higher than the critical power, as shown by the solid curve in Figure 4.9(b). Rapid compression is achieved by the combined action of the collapse phenomenon and self-similar pulse compression in the exponentially decreasing dispersion (dashed curve). The occurrence of collapse is postponed in the case of exponentially increasing dispersion (dot-dashed curve) since the self-similar effect in the exponentially increasing dispersion acts against the collapse. Our numerical results show that the chirped Townes soliton exhibits similar property as the Townes soliton with constant dispersion when the input peak power deviates from the ideal peak power. Thus it is likely that the chirped Townes soliton is also marginally stable.

Finally, in general it is difficult to realize a medium exhibiting pure quintic nonlinearity. It is therefore important to determine the tolerance of chirped Townes soliton of a quintic medium to the presence of a small amount of cubic nonlinearity. Figure 4.10 shows the change in peak power of the Townes soliton

in the presence of cubic nonlinearity. The parameters in Fig. 4.10 are same as those in Fig. 4.1 except $\gamma(0) = 10^{-5}$/W/m (solid curve), $\gamma(0) = 10^{-4}$/W/m (dot-dashed curve) and $\gamma(0) = 10^{-3}$/W/m (dashed curve). The dots represent results of pure quintic nonlinearity. The solid curve, dot-dashed curve and dashed curve represent the results when the ratio of cubic nonlinear length to quintic nonlinear length (L_{n2}/L_{n4}) are 12000, 1200 and 120 respectively. It is clear that the pure quintic result almost matches with cubic-quintic result only for the chosen value of cubic nonlinearity (L_{n2}/L_{n4} 12000). As the cubic nonlinearity increases, Figure 4.10 shows that the evolution of the chirped Townes soliton is very sensitive to the presence of even a small amount of cubic nonlinearity ($L_{n4}/L_{n2} < 0.1\%$). As the cubic nonlinearity increases, the chirped Townes soliton pulse becomes unstable.

4.5 Summary

By using self-similar scaling analysis, we have found the chirped bright soliton solutions in the anomalous and normal dispersion regimes of cubic-quintic nonlinear media. By means of direct numerical simulation, we show that the chirped soliton in the anomalous dispersion regime is stable whereas that in the normal dispersion regime is unstable. For these chirped solitons, the dispersion length, the cubic nonlinear length, and the quintic nonlinear length are related. If the quintic nonlinear length goes to infinity, dispersion length will equal cubic nonlinear length. We observed that by the use of exponentially decreasing dispersion, it is possible to utilize these self-similar solitons to achieve pedestal free pulse compression in cubic-quintic nonlinear media. We then studied the evolution of the chirped bright solitons when the initial peak power or the initial chirp is perturbed. We have found that the evolution of the soliton is not

significantly affected even when the perturbations in the initial parameters is ±20% of its ideal values. The solitons have better tolerance to perturbations in the initial chirp than initial peak power. We have carried out extensive numerical simulations by varying the decay rate of dispersion and changing the strength of the quintic nonlinearity. From the numerical simulations, we have observed that competition between the cubic and quintic nonlinearities stabilizes the pulse against perturbations in initial pulse parameters. Hence, one can construct a stable pedestal free optical pulse compressor by using competing cubic quintic nonlinearities.

Finally, we studied the chirped Townes soliton in pure quintic nonlinear media. As the Townes solitons with constant dispersion are marginally stable, we studied the perturbation of the chirped Townes soliton in terms of peak power. We found that we can achieve fast pulse compression by combining the wave collapse and exponentially decreasing dispersion when the perturbation is higher than the ideal one. The occurrence of collapse can also be postponed by using the exponentially increasing dispersive media. These two issues (fast and slow compression) could be implemented depending on the physical situation and requirement. Applications in terms of BEC in the TG regime have also been discussed.
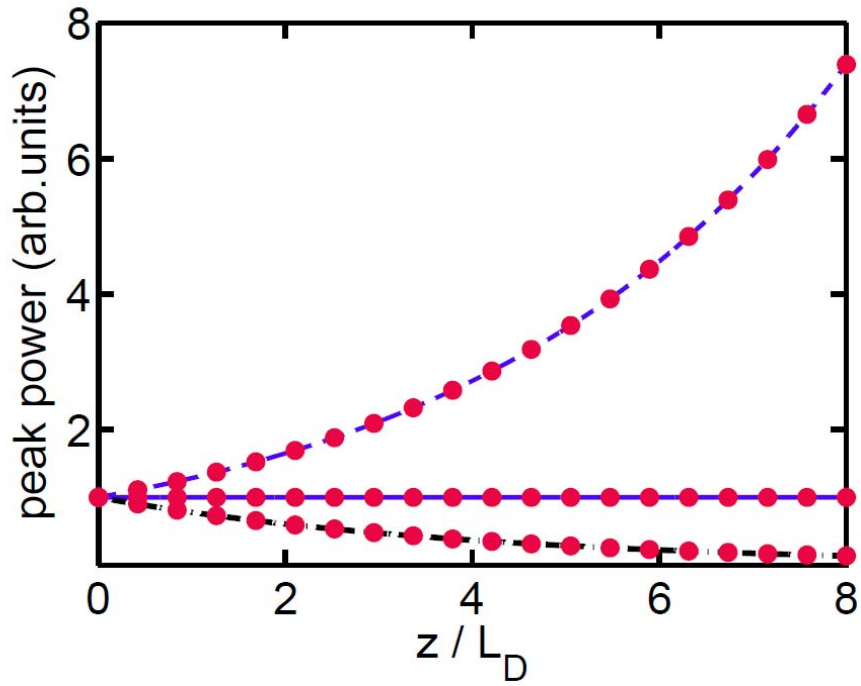
Figure 4.8: Evolution of the peak power of Townes soliton when the dispersion is constant (solid curve, $\beta_0 = -0.5$ ps^2/m), exponentially increasing (dot-dashed curve, $\sigma = -0.005$ /m) and exponentially decreasing dispersion (dashed curve, $\sigma = 0.005$ /m). The dots represent the results obtained by numerical simulation. The physical parameters are same as those in Fig. 4.1 except $\gamma = 0$.
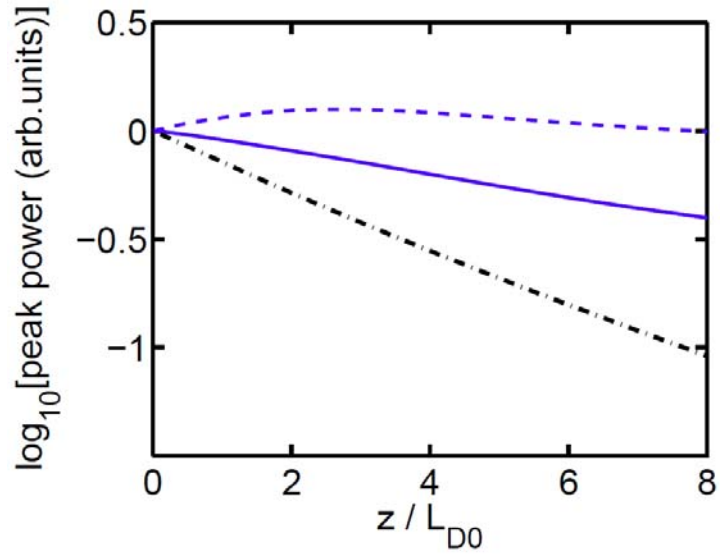
(a)
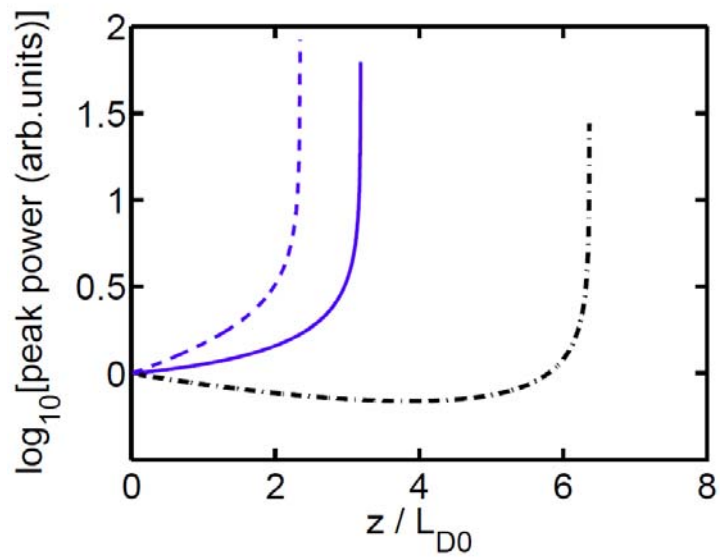
(b)

Figure 4.9: (a) The deviations of peak power from the exact Townes soliton solution when the input peak power deviates from the ideal peak power by (a) −5% and (b) +5% when the dispersion is constant (solid curve), exponentially decreasing (dashed curve), and exponentially increasing (dot-dashed curve). The physical parameters are same as those in Fig. 4.8.
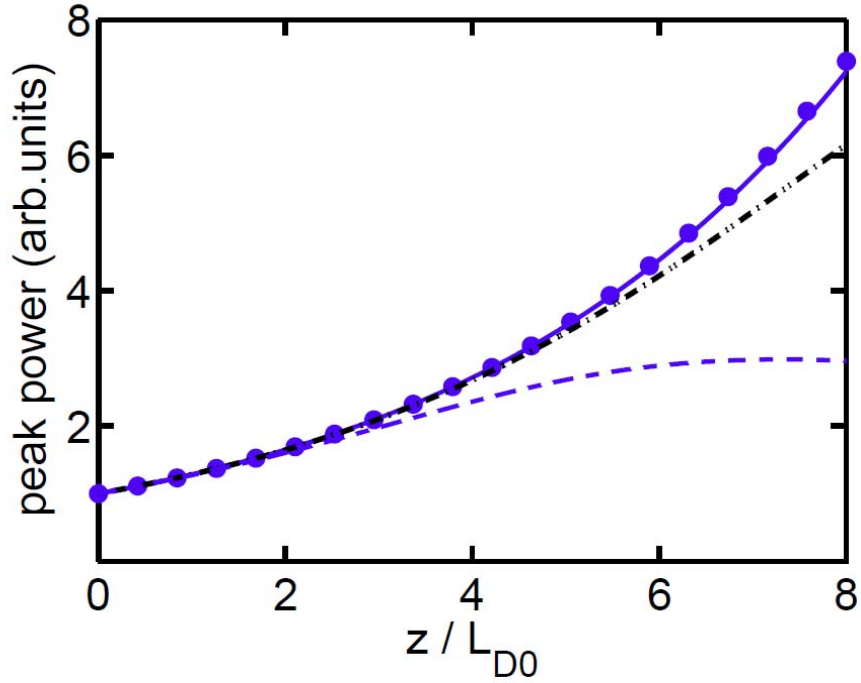
Figure 4.10: Evolution of the peak powers of chirped Townes solitons in the presence of cubic nonlinearity. The dots represent results of the pure quintic nonlinearity. The solid curve, dot-dashed curve and dashed curve represent the results when the ratio of cubic nonlinear length to quintic nonlinear length (L_{n2} / L_{n4}) are 12000, 1200 and 120, respectively. The corresponding values of cubic nonlinearity are $\gamma_0 = 10^{-5}$ /W/m, 10^{-4} /W/m and 10^{-3} /W/m, respectively. The other physical parameters are same as those in Fig. 4.1.

Chapter 5

Conclusions

Generation of short optical pulses has always been of great scientific and technological interest. There is variety of methods for temporally compressing optical pulses. These methods can be grouped into two categories: linear pulse compression and nonlinear pulse compression. Nonlinear compression, which relies on the iteration of Kerr nonlinearity and quadratic dispersion, can generate an increased bandwidth, which is an effect that linear compression is incapable of doing. There are two widely used techniques to achieve optical pulse compression; namely, higher-order soliton compression and adiabatic pulse compression. The former can have a large degree of compression, but the compressed pulses suffer from significant pedestal generation, leading to nonlinear interactions between neighboring solitons. Some techniques, such as the nonlinear intensity discrimination technique [19, 20] can reduce the pedestals, but typically energy is wasted. Adiabatic soliton compression typically utilizes a dispersion map with monotonically decreasing dispersion along the propagation direction, and is formally equivalent to distributed amplification [21]. If the dispersion varies slowly enough, the soliton self-adjusts to maintain the balance between dispersion and nonlinearity [2]. This compression scheme is attractive because it inherently maintains the transform-limited characteristics of the pulse as it compresses [2].

However, adiabatic condition must be satisfied, i.e. change must be gradual. Such compression has been demonstrated experimentally by a variety of schemes to achieve the effect of decreasing dispersion.

As Moores pointed out in [24], exact chirped soliton solutions to the NLS equation exist when we have distributed gain or exponentially varying dispersion. One of the advantages of this compression scheme is that the adiabatic condition does not need to be satisfied and rapid compression is possible. More recently, a technique known as self-similar analysis has been utilized to study linearly chirped pulses in optical fibers and fiber amplifiers [25–28]. Self-similar pulses have attracted much attention since the linear chirp facilitates efficient pulse compression. In addition, these pulses can propagate without pulse breakup, called optical wave breaking, even at high powers. However, because of the relatively small group velocity dispersion of optical fibers, this scheme requires long fiber lengths, and only a few dispersion profiles are practically feasible. Moreover, fabrication of fibers with complex dispersion profiles usually involves the splicing of several different fibers or drawing fibers with an axially varying core diameter. A more attractive solution to achieve pulse compression is by utilizing a highly dispersive nonlinear medium such as a FBG. Grating dispersion just outside the stop band is up to 6 orders of magnitude larger than that of silica fiber and can be tailored simply by changing the grating profile. Grating dispersion can exceed 100 ps^2 /cm for a fiber grating, and this feature has been used for dispersion compensation in transmission [76]. Moreover, almost any grating profiles can be manufactured using the state of-the-art grating-writing techniques. This potential suggests utilizing this huge dispersion to construct a compact optical pulse compressor.

In this thesis, we consider the attractive solution consists of pulse compression in a highly dispersive nonlinear medium such as a FBG. Using the self-similar analysis, we have theoretically investigated the linearly chirped Bragg solitary pulses near the PBG structure of FBG. The Painlevé analysis is carried out to obtain the condition for the soliton pulse propagation governed by the NLS equation with varying dispersion. Two dispersion profiles satisfying this criterion are the constant dispersion and exponentially decreasing dispersion profiles. In the exponentially varying dispersive media, we explain the existence and formation of chirped optical soliton through the variational equation for the chirp parameter. For further elucidation, we provide the phase plane diagram in terms of the normalized chirp and intensity (peak power) which clearly explains the physical process of linearly chirped soliton pulse compression in the exponentially decreasing dispersion media. In addition, we present the essential steps for driving the exact soliton solution of the variable coefficient NLS equation using the Bäcklund transformation method. Efficient Bragg soliton pulse compression can be achieved with the exponentially decreasing dispersion. The main advantages of this compression scheme are the high degree of compression and the high pulse quality. Our simulation results show that the exponentially decreasing dispersion profile is not a must, and stepwise approximation is carried out by concatenation of grating segments with different constant dispersion coefficients. The required section number is found to be associated with the compression factor and initial chirp value. Unlike conventional solitons, the solution to the NLS type equation with exponentially varying dispersion is chirped. The linear chirp is a key feature of the self-similar characteristics of the solution which allows pedestal-free pulse compression. In pulse compression,

144

typically the input pulse is unchirped although the pulse after compression is usually chirped. Thus for the proposed compression scheme, the input pulse must be pre-chirped in a prescribed manner. Therefore, a simple pre-chirper, such as a linear fiber or grating, is used to add the required chirp profile to initial chirp-free hyperbolic secant or Gaussian pulse. In particular, the initial Gaussian profile has evolved into a hyperbolic secant profile after the compression in nonlinear FBG. The comparisons between simulation of NLS type equation, pulse parameter evolution equations, and nonlinear coupled-mode equations have been given.

The NLS equation with Kerr effect has been successful in explaining a large number of nonlinear effects. However, higher order nonlinearities must be considered if the optical pulse intensity is high or the nonlinear coefficients of the materials are large, for instance, in semiconductor doped glasses. We have investigated the existence of chirped bright solitary wave solutions in the cubic-quintic nonlinear media with exponentially decreasing dispersion. From the stability analysis, we show that the solitary wave solution in the anomalous dispersion regime is stable whereas the one in the normal dispersion regime is unstable. Numerical simulation results show that competing cubic and quintic nonlinearities stabilize the chirped solitary wave propagation against perturbations of the initial pulse parameters. In addition, we studied the possibility of rapid compression of Townes solitons by the collapse phenomenon in the exponentially decreasing dispersion. We also found that the collapse could be postponed if the dispersion increases exponentially.

Until now we only carry out the theoretical study and we plan to conduct experimental research on the performance of this novel pulse compressor in the near future.

145

Appendix A: Acronyms

BA	bare approximation
BEC	Bose-Einstein Condensate
CQ	cubic-quintic
CQNLS	cubic-quintic nonlinear Schrödinger
DCF	dispersion compensating fiber
DM	dispersion managed
DDFBG	dispersion exponentially decreasing FBG
FBG	fiber Bragg grating
FFT	fast Fourier transform
FWHM	full width at half maximum intensity
GVD	group velocity dispersion
IST	inverse scattering transform
LVM	Lagrangian variational method
NFBG	nonlinear fiber Bragg grating
NLCM	nonlinear coupled-mode
NLCMEs	nonlinear coupled-mode equations
NLS	nonlinear Schrödinger
NLSE	nonlinear Schrödinger equation
ODE	ordinary differential equation
PBG	photonic bandgap
PDE	partial differential equation
QNLS	pure quintic nonlinear Schrödinger
RK	Runge-Kutta

SPM	self-phase modulation
SSFM	split-step Fourier method
SWA	stepwise approximation
VA	variational analysis
VK	Vakhitov-Kolokolov
WDM	wavelength-division multiplexed

Appendix B: Split-Step Fourier Method

The NLS equation governing the evolution of the slowly varying envelope of an optical pulse including the effect of dispersion and Kerr effect is given by

$$i\frac{\partial q}{\partial z} - \frac{\beta_2}{2}\frac{\partial^2 q}{\partial t^2} + \gamma |q|^2 q = 0, \tag{B.1}$$

where $q(z,t)$ is the slowly varying amplitude of the pulse envelope, z is the distance, t is the time, $\beta_2(z)$ is the group velocity dispersion coefficient, and γ is the nonlinear parameter. The second term and the third term on the left hand side of Eq. (B.1) represents the effect of GVD and SPM, respectively. In general, the dispersion coefficient $\beta_2(z)$ is distance dependent. Effects such as loss and higher order dispersions are not included in Eq. (B.1). We solve Eq. (B.1) as an initial value problem, i.e. given the initial shape $q(z=0,t)$, we want to find the pulse shape at $z=L$, i.e. $q(z=L,t)$.

The NLS equation is a nonlinear partial differential equation that does not generally have analytic solutions except for some specific cases in which the inverse scattering (IST) method [116] can be employed. Even though sometimes IST solves the NLS equation exactly, it is seldom used in the study of soliton propagation in optical fibers because IST is a rather complex method and it is difficult to incorporate perturbative effects in the IST formulation. Therefore, a numerical approach is often needed to understand the pulse propagation in optical fibers. Two types of numerical methods are commonly used in solving NLS-type

equations; they are finite-difference methods and pseudo-spectral methods [5]. Among the different numerical methods, SSFM, a type of pseudo-spectral method, is the most widely used. The use of FFT algorithm in the SSFM, make the SSFM faster by up to two orders of magnitude compared with most finite-difference schemes [117]. In the SSFM, the equation is split into multiple partial equations each of which contains some of the operators in the original equation. At each propagation step, the partial equations are solved in some chosen order. For example, the NLS equation can be split into the following equations,

$$i\frac{\partial q}{\partial z} - \frac{\beta_2}{2}\frac{\partial^2 q}{\partial t^2} = 0, \tag{B.2}$$

$$i\frac{\partial q}{\partial z} + \gamma |q|^2 q = 0. \tag{B.3}$$

Equation (B.2) contains the effect of GVD only, while Eq. (B.3) contains the effect of SPM only. The algorithm consists of solving Eqs. (B.2) and (B.3) alternately at each propagation step size Δz. In general, dispersion and nonlinearity act together along the length of fiber. The SSFM obtains an approximate solution by assuming that in propagating the optical field over a sufficiently small distance Δz, the dispersive and nonlinear effects can be assumed to act independently [5]. The iterative solutions of Eqs. (B.2) and (B.3) approximate that of the NLS equation. Both Eqs. (B.2) and (B.3) can be solved exactly for a given initial pulse. See Appendix C and D. The mathematical terms due to dispersion and nonlinearity are separate and decoupled in the NLS equation. It is this fact that allows the use of the SSFM for solving the NLS equation. For NLS equation given by Eq. (B.1), we write it in the form of

$$\frac{\partial q}{\partial z} = \left(\widehat{D} + \widehat{N}\right)q, \tag{B.4}$$

where $\widehat{D} = -\dfrac{i\beta_2}{2}\dfrac{\partial^2}{\partial t^2}$, and $\widehat{N} = i\gamma|A|^2$. For each propagation step, mathematically

$$q(z+\Delta z,t) \approx \left(\exp\Delta z\widehat{D}\right)\left(\exp\Delta z\widehat{N}\right)q(z,t). \tag{B.5}$$

The SSFM for solving the NLS equation is summarized in the following.

I   Transform the pulse $q(z,t)$ into the frequency domain $\tilde{q}(z,\omega)$ using a FFT algorithm, where $q(z,t)$ is the envelope of the electric field and $\tilde{q}(z,\omega)$ is the envelope of spectrum.

II   Propagate the spectral components by, $\tilde{q}(z',\omega) = \tilde{q}(z,\omega)\exp\left(i\beta_2\omega^2\Delta z/2\right)$. This is the dispersion step.

III Transform the spectrum $\tilde{q}(z',\omega)$ back to the time domain $q(z',t)$ by the inverse FFT.

IV Propagate the solution by, $q(z+\Delta z,t) = q(z',t)\exp\left(i\gamma|q(z',t)|^2\Delta z\right)$. This is the nonlinear step.

V   Repeat from STEP I to IV. Substitute $q(z,t)$ with $q(z+\Delta z,t)$ and iterate until the accumulated distance is equal to the required transmission distance.

   Apart from its simplicity, the SSFM is unconditionally stable. Numerical stability is a desirable property of numerical algorithms. If not, small errors can be magnified instead of damped leading to enormous errors.

Appendix C: Solution of Dispersion Equation

We apply Fourier transform to the following equation,

$$i\frac{\partial q}{\partial z} - \frac{\beta_2}{2}\frac{\partial^2 q}{\partial t^2} = 0, \tag{C.1}$$

$$\frac{i}{2\pi}\int_{-\infty}^{\infty}\frac{\partial \tilde{q}(z,\omega)}{\partial z}\exp(-i\omega t)d\omega - \frac{\beta_2(z)}{4\pi}\int_{-\infty}^{\infty}(-i\omega)^2\tilde{q}(z,\omega)\exp(-i\omega t)d\omega = 0, \tag{C.2}$$

where $\tilde{q}(z,\omega)$ is the spectrum of the pulse $q(z, t)$. Eq. (C.2) can be rewritten as,

$$i\frac{\partial \tilde{q}(z,\omega)}{\partial z} + \frac{\beta_2(z)\omega^2}{2}\tilde{q}(z,\omega) = 0. \tag{C.3}$$

Hence

$$\tilde{q}(L,\omega) = \tilde{q}(0,\omega)\exp\left[\frac{i\omega^2}{2}\int_0^L \beta_2(z)dz\right]. \tag{C.4}$$

Appendix D: Solution of SPM Equation

Before solving $i\dfrac{\partial q}{\partial z} + \gamma |q|^2 q = 0,$ we show that $|q|^2$ is independent of z.

$$q^*(i\frac{\partial q}{\partial z} + \gamma |q|^2 q) = 0, \tag{D.1}$$

$$\left[q^*(i\frac{\partial q}{\partial z} + \gamma |q|^2 q) \right]^* = 0. \tag{D.2}$$

Subtracting Eq. (D.1) from Eq. (D.2), we have

$$(iq^*\frac{\partial q}{\partial z} + \gamma |q|^4) - \left[-iq\left(\frac{\partial q}{\partial z}\right)^* + \gamma |q|^4 \right] = 0, \tag{D.3}$$

$$q^*\frac{\partial q}{\partial z} + q\frac{\partial q^*}{\partial z} = 0, \tag{D.4}$$

$$\frac{\partial \left(|q|^2\right)}{\partial z} = 0. \tag{D.5}$$

Hence $|q|^2$ is a constant. Eq. (D.3) can then be solved directly, we have

$$i\frac{\partial q}{\partial z} + \gamma |q|^2 q = 0, \tag{D.6}$$

$$i\int_0^L \frac{1}{q}\frac{\partial q}{\partial z} dz = -\int_0^L \gamma |q|^2 dz, \tag{D.7}$$

$$q(L,t) = q(0,t)\exp(i\gamma |q(0,t)|^2 L). \tag{D.8}$$

For $i\dfrac{\partial q}{\partial z} + \gamma |q|^2 q - \delta |q|^4 q = 0,$ similarly we have

$$q^* \left(i \frac{\partial q}{\partial z} + \gamma |q|^2 q - \delta |q|^4 q \right) = 0, \tag{D.9}$$

$$\left[q^* \left(i \frac{\partial q}{\partial z} + \gamma |q|^2 q - \delta |q|^4 q \right) \right]^* = 0. \tag{D.10}$$

Substracting Eq. (D.9) from Eq. (D.10), we have

$$\frac{\partial \left(|q|^2 \right)}{\partial z} = 0. \tag{D.11}$$

Then

$$q(L,t) = q(0,t) \exp \left(i\gamma |q(0,t)|^2 L - i\delta |q(0,t)|^4 L \right). \tag{D.12}$$

Appendix E: Errors Associated with the Split-Step Fourier Method

The SSFM was first applied in 1973 [118] to study the pulse propagation in optical fibers. Since then, this method has been used extensively for studying various nonlinear effects in optical fibers [119–127]. Although the method is relatively straightforward to implement, it requires that step sizes in z and t be selected carefully to maintain the required accuracy [128]. A few guidelines are available in [129–132] for the optimum choice of step sizes. The use of FFT in the SSFM imposes periodic boundary conditions. This is acceptable in practice if the temporal window used in simulation is much wider than the pulse width. Typically, the temporal window is chosen to be 10 to 20 times the pulse width [5]. Errors arise from the wrong choice of the numerical parameters. But, these errors can be avoided by the proper choice of step-size in z / t and spectral / temporal window. However, the primary source of error for the SSFM is due to the noncommuting operators $\widehat{D}$ and $\widehat{N}$ ($\left[\widehat{D}, \widehat{N}\right] \neq 0$). Physically, this implies that the origin of dispersive and nonlinear effects is intrinsically coupled.

To estimate the accuracy of the SSFM, we note that the exact solution of Eq. (B.1) is

$$q(z+\Delta z, t) = \exp\left[\Delta z\left(\widehat{D}+\widehat{N}\right)\right]q(z,t). \tag{E.1}$$

if $\widehat{N}$ is assumed to be z independent.

For two noncommuting operators $\widehat{D}(\Delta z)$ and $\widehat{N}(\Delta z)$, the expansion of $\exp\left(\Delta z\widehat{D}\right)\exp\left(\Delta z\widehat{N}\right)$ can be obtained using the Baker-Hausdorff theorem [133],

$$\exp\left(\Delta z\widehat{D}\right)\exp\left(\Delta z\widehat{N}\right) = \exp\left[\Delta z\left(\widehat{D}+\widehat{N}+\frac{1}{2}\left[\widehat{D},\widehat{N}\right]+\frac{1}{12}\left[\widehat{D}-\widehat{N},\left[\widehat{D},\widehat{N}\right]\right]+...\right)\right].$$

(E.2)

A comparison of Eq. (E.1) and (E.2) shows that the SSFM with $\exp\left(\Delta z\widehat{D}\right)\exp\left(\Delta z\widehat{N}\right)$ is only first order accurate. A second order accurate result can be obtained by symmetrizing the algorithm such as using $\exp\left(\frac{\Delta z}{2}\widehat{D}\right)\exp\left(\Delta z\widehat{N}\right)\exp\left(\frac{\Delta z}{2}\widehat{D}\right)$ instead of $\exp\left(\Delta z\widehat{D}\right)\exp\left(\Delta z\widehat{N}\right)$. We will show that the symmetrized algorithm is second order accurate in the following.

The exact solution $q(z+\Delta z,t)$ of Eq. (B.1), can be obtained by using Taylor series expansion of $q(z,t)$ at z,

$$q(z+\Delta z,t) = q + \Delta z q_z + \frac{\Delta z^2}{2!}q_{zz} + \frac{\Delta z^3}{3!}q_{zzz} + ...,$$

(E.3)

where q_z represents $\partial q/\partial z$ at z, q_{zz} represents $\partial^2 q/\partial z^2$ at z, and so on. Using Eq. (B.1) and set $\beta_2(z)=-1$ and $\gamma=1$, we have

$$q_z = i\left(\frac{1}{2}q_{tt}+|q|^2 q\right),$$

$$q_{zz} = -\left(\frac{1}{4}q_{tttt}+2|q|^2 q_{tt}+2|q_t|^2 q+q_t^2 q^*+|q|^4 q\right),$$

$$q_{zzz} = -i\left[\frac{1}{8}q_{tttttt} + \frac{5}{2}q^* q_{tt}^2 + 3q^* q_t q_{ttt} + 7|q_t|^2 q_{tt} + \frac{5}{2}q_t^2 q_{tt}^*\right.$$

$$+2q|q_{tt}|^2 + 3qq_t^* q_{ttt} + qq_t q_{ttt}^* + |q|^6 q + 5|q|^2 q^* q_t^2 + \frac{11}{2}|q|^4 q_{tt} \qquad \text{(E.4)}$$

$$\left.+\frac{3}{2}|q|^2 q_{tttt} + 12|q|^2 q|q_t|^2 + 2q^3\left(q_t^*\right)^2 + |q|^2 q^2 q_{tt}^* + \frac{1}{4}q^2 q_{tttt}^*\right],$$

where q_t represents $\partial q/\partial t$ at z, q_{tt} represents $\partial^2 q/\partial t^2$, etc, and q^* is the complex conjugate of $q(z,t)$.

Evaluation of the numerical algorithm $\exp\left(\frac{\Delta z}{2}\widehat{D}\right)\exp\left(\Delta z\widehat{N}\right)\exp\left(\frac{\Delta z}{2}\widehat{D}\right)$, up to $(\Delta z)^3$ gives

$$\exp\left(\frac{\Delta z}{2}\widehat{D}\right)q = \exp\left[i\left(\frac{\Delta z}{4}\right)\frac{\partial^2}{\partial t^2}\right]q,$$

$$= q + i\frac{\Delta z}{4}q_{tt} - \frac{(\Delta z)^2}{32}q_{tttt} - i\frac{(\Delta z)^3}{384}q_{tttttt} + ...$$

$$\exp\left(\Delta z\widehat{N}\right)\exp\left(\frac{\Delta z}{2}\widehat{D}\right) = q + i\Delta z\left(|q|^2 q + \frac{1}{4}q_{tt}\right) - (\Delta z)^2\left(\frac{1}{32}q_{tttt} + \frac{1}{2}q_{tt}|q|^2 - \frac{1}{4}q_t^* q^2 + \frac{1}{2}|q|^4 q\right) +$$

$$i(\Delta z)^3\left(-\frac{1}{384}q_{tttttt} - \frac{1}{32}q^2 q_{tttt}^* + \frac{1}{8}q|q_t|^2 - \frac{1}{16}|q|^2 q_{tttt} - \frac{1}{16}q^* q_{tt}^2 +\right.$$

$$\left.\frac{1}{4}q^2|q|^2 q_{tt}^* - \frac{3}{8}|q|^4 q_{tt} - \frac{1}{6}|q|^6 q\right) + ...$$

$$\exp\left(\frac{\Delta z}{2}\widehat{D}\right)\exp\left(\Delta z\widehat{N}\right)\exp\left(\frac{\Delta z}{2}\widehat{D}\right) = q + i\Delta z\left(|q|^2 q + \frac{1}{2}q_{tt}\right) - (\Delta z)^2\left(\frac{1}{8}q_{tttt} + |q|^2 q_{tt} + |q_t|^2 q\right.$$

$$\left.+\frac{1}{2}q_t^2 q^* + \frac{1}{2}|q|^4 q\right) - i(\Delta z)^3\left[\frac{1}{48}q_{tttttt} + \frac{1}{4}q|q_t|^2 + \frac{1}{4}|q|^2 q_{tttt} + \frac{3}{8}q^* q_{tt}^2 + \frac{3}{4}|q|^4 q_{tt} + \frac{1}{6}|q|^6 q\right.$$

$$\left.+\frac{1}{4}q_t^2 q_{tt}^* + |q_t|^2 q_{tt} + \frac{1}{2}q^* q_t q_{ttt} + \frac{1}{2}qq_t^* q_{ttt} + \frac{3}{4}|q|^2 q^* q_t^2 + \frac{3}{2}|q|^2 q|q_t|^2 + \frac{1}{4}q^3\left(q_t^*\right)^2\right] + ...$$

$$\text{(E.5)}$$

From Eq. (E.5), the coefficients of the Δz and $(\Delta z)^2$ terms are the same as that of the true solution, the deviation is proportional to $(\Delta z)^3$. Therefore, the accuracy of the symmetric SSFM is second-order accurate. The difference between the exact solution and numerical solution at $(\Delta z)^3$ is

$$\Delta q = q_{exact} - q_{app} = -i\left[q^* q_{tt}^{\ 2}/24 + |q_t|^2 q_{tt}/6 + q_t^{\ 2} q_{tt}^*/6 + q|q_{tt}|^2/12 + qq_t q_{ttt}^*/6 \right.$$

$$\left. + |q|^2 q^* q_t^{\ 2}/12 + |q|^4 q_{tt}/6 + |q|^2 q|q_t|^2/2 + q^3\left(q_t^*\right)^2/12 + |q|^2 q^2 q_{tt}^*/6 + q^2 q_{ttt}^*/24 \right](\Delta z)^3$$

(E.6)

In Fig E.1, we plot the magnitude of the coefficient before $(\Delta z)^3$ in Eq. (E.11) for a fundamental soliton solution of Eq. (B.1); $q(z,t) = \mathrm{sech}(t)\exp(iz/2)$. The maximum difference is about 0.1667 at $t = 0$. Figure E.1 is obtained by using Maple.

The FFT and inverse FFT are the most computational intensive parts of the SSFM. For each step in the second order algorithm, four FFTs are required; two for the forward transform and two for the backward transform. It therefore appears that $4n$ FFTs are required for distance $z = n\Delta z$. In practice, the SSFM can be made to run much faster by noting

$$q(z = n\Delta z, t) = \left[\exp\left(\frac{\Delta z}{2}\widehat{D}\right)\exp\left(\Delta z\widehat{N}\right)\exp\left(\frac{\Delta z}{2}\widehat{D}\right) \right]^n q(0,t),$$
(E.7)

$$= \exp\left(-\frac{\Delta z}{2}\widehat{D}\right)\left[\exp\left(\Delta z\widehat{D}\right)\exp\left(\Delta z\widehat{N}\right) \right]^n \exp\left(\frac{\Delta z}{2}\widehat{D}\right)q(0,t),$$
(E.8)

or

$$= \exp\left(-\frac{\Delta z}{2}\widehat{N}\right)\left[\exp\left(\Delta z\widehat{N}\right)\exp\left(\Delta z\widehat{D}\right) \right]^n \exp\left(\frac{\Delta z}{2}\widehat{N}\right)q(0,t).$$
(E.9)

Therefore, except for the first and last steps, all intermediate steps can be carried over the whole segment length Δz. As a result, the required number of FFTs can be reduced roughly by a factor of 2 and the numerical code has been speed up by the same factor.
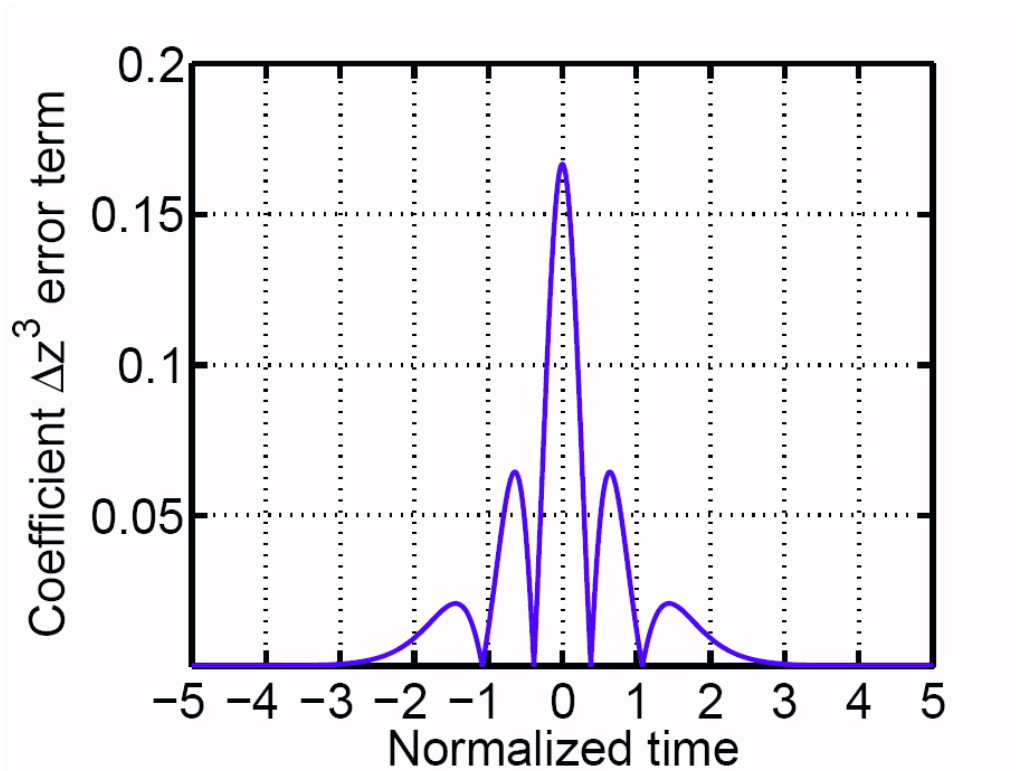
Figure E.1: The coefficient leading order $(\Delta z)^3$ error term in a symmetrized split-step Fourier algorithm. The simple soliton solution $q(z, t) = \text{sech}(t)\exp(iz/2)$ is used.

Appendix F: Modified SSFM for Exponentially Varying Dispersion

Here, we discuss the modified SSFM for the NLS-type equation with exponentially varying dispersion. Consider the NLS-type equation given by

$$i\frac{\partial E}{\partial z} - \frac{\beta_2(z)}{2}\frac{\partial^2 E}{\partial t^2} + \gamma |E|^2 E = 0. \tag{F.1}$$

Let us introduce the normalized distance ξ, the normalized amplitude U and the normalized time τ given by

$$\xi = \frac{z}{L_N}, U = \frac{E}{A_0}, \tau = \frac{t}{T_0}, \tag{F.2}$$

where $L_N = \dfrac{1}{\gamma_g A_0^2}$, A_0 is the initial amplitude, and T_0 is the initial pulse width parameter.

Then, we have

$$i\frac{\partial U}{\partial \xi} - \frac{\beta_2(\xi L_N) L_N}{2T_0^2}\frac{\partial^2 U}{\partial \tau^2} + |U|^2 U = 0. \tag{F.3}$$

Split (F.3) into

$$i\frac{\partial U}{\partial \xi} - \frac{\beta_2(\xi L_N) L_N}{2T_0^2}\frac{\partial^2 U}{\partial \tau^2} = 0, \tag{F.4a}$$

$$i\frac{\partial U}{\partial \xi} + |U|^2 U = 0. \tag{F.4b}$$

For dispersion step (F.4a), it is readily solved by using the Fourier-transform method. If $\tilde{U}(z,\omega)$ is the Fourier transform of $U(z,\tau)$, such that it satisfies an ordinary differential equation

$$i\frac{\partial \tilde{U}}{\partial z} = -\frac{1}{2}\beta_2(z)\omega^2\tilde{U}. \tag{F.5}$$

Considering the exponentially decreasing dispersion $\beta_2(z) = \beta_{20}\exp(-\sigma z)$, the solution of Eq. (F.5) is given by

$$\tilde{U}(\xi+\Delta\xi,\omega) = \tilde{U}(\xi,\omega)\exp\left[i\omega^2\exp(-\sigma\xi L_N)\beta_{20}\frac{1-\exp(-\sigma\Delta\xi L_N)}{2\sigma}\right]. \tag{F.6}$$

For nonlinear step (F.4b), the solution is given by

$$U(\xi+\Delta\xi,\tau) = U(\xi,\tau)\exp\left(i|U|^2\Delta\xi\right). \tag{F.7}$$

We propose two schemes to simulate exponentially decreasing dispersion profile. $\widehat{D}$ stands for the dispersion step in Eq. (F.6), while $\widehat{N}$ stands for the nonlinear step in Eq. (F.7).

1st scheme: $\widehat{N}^{-1}\left(\dfrac{\Delta\xi}{2}\right)\left[\widehat{N}(\Delta\xi)\widehat{D}(\Delta\xi)\right]^n\widehat{N}\left(\dfrac{\Delta\xi}{2}\right)$.

2nd scheme: $\displaystyle\int_0^{\frac{\Delta\xi}{2}}\widehat{D}\widehat{N}\int_{\frac{\Delta\xi}{2}}^{\frac{3\Delta\xi}{2}}\widehat{D}\widehat{N}\int_{\frac{3\Delta\xi}{2}}^{\frac{5\Delta\xi}{2}}\widehat{D}\widehat{N}......\int_{\frac{(2k-3)\Delta\xi}{2}}^{\frac{(2k-1)\Delta\xi}{2}}\widehat{D}\widehat{N}\int_{\frac{(2k-1)\Delta\xi}{2}}^{k\Delta\xi}\widehat{D}\widehat{N}$.

The first scheme has same expression for all the dispersion steps, while the second scheme has to consider the dispersion step at different position. Therefore, the first one is easier to implement.

Appendix G: Numerical Solutions to the NLCM Equations on a finite Interval

In our studies of pulse compression in nonlinear FBG, we need to study the dynamics of geometries of finite extent, and it can be solved by the numerical approach [53] which uses the characteristics of the equations and integrates forward in time by using an implicit fourth-order Runge-Kutta formula.

The particular set of coupled-mode equations that we consider is

$$
\begin{aligned}
i\frac{\partial u}{\partial z} + i\beta_1 \frac{\partial u}{\partial t} + \delta u + \kappa v + \gamma\left(|u|^2 + 2|v|^2\right)u &= 0 \\
-i\frac{\partial v}{\partial z} + i\beta_1 \frac{\partial v}{\partial t} + \delta v + \kappa u + \gamma\left(|v|^2 + 2|u|^2\right)v &= 0,
\end{aligned}
\tag{G.1}
$$

where z and t are spacelike and timelike coordinates, β_1 is the group delay per unit length, u, v denotes the envelope functions of the forward- and backward-traveling modes that determine the electric field inside the system, δ is the frequency detuning from the Bragg frequency, κ is the coupling coefficient, and γ is the nonlinear coefficient. As illustrated in Figure G.1, the system has length L and is driven by radiation coming in at $z = 0$. The incoming radiation is given by $A(t)$. With this notation the boundary conditions now attain the well-known form

$$
\begin{aligned}
u(0,t) &= A(t), \\
v(L,t) &= 0.
\end{aligned}
\tag{G.2}
$$

Figure G.1: Schematic of our geometry. The incoming radiation is denoted by A(*t*), while the reflected and transmitted radiation is designated by *R*(*t*) and *T*(*t*), respectively. *L* is the length. (After Ref. [53], © 1991 OSA.)

In addition, we assume that the system initially contains no energy, so that

$$u(z,0) = 0,$$
$$v(z,0) = 0. \tag{G.3}$$

In practice it is often useful for Eqs. (G.1)–(G.3) to be solved in a rotated frame [53]. Equations (G.1)–(G.3) constitute a well-posed hyperbolic initial-value problem [53]. We want to calculate the envelope functions $u(z,t)$ and $v(z,t)$, which correspond to the transmitted and reflected radiations. The amplitudes of the reflected and transmitted radiation, indicated schematically in Fig. G.1, are given by $R(t) = v(0,t)$ and $T(t) = u(L,t)$, respectively.

Equations (G.1) have the important property that their characteristics [53] are straight lines. By applying the coordinate transformations

$$\zeta = \frac{z}{2} + \frac{t}{2\beta_1}, \tau = -\frac{z}{2} + \frac{t}{2\beta_1}, \tag{G.4}$$

we obtain the equations

$$\frac{\partial u}{\partial \zeta} = i\left[\delta u + \kappa v + \gamma\left(|u|^2 + 2|v|^2\right)u\right], \tag{G.5a}$$

$$\frac{\partial v}{\partial \tau} = i\left[\delta v + \kappa u + \gamma\left(|v|^2 + 2|u|^2\right)v\right], \tag{G.5b}$$

162

so that the integration directions coincide with the characteristics. Both equations (G.5) look like ordinary differential equations (ODEs). But, they are coupled through their right-hand sides. As a result, if the envelope functions are known at a given point in space and time, say (ζ_0, τ_0), one can apply some numerical method to Eq. (G.5a), to calculate $u(\zeta_0 + \delta\zeta, \tau_0)$, and to Eq. (G.5b), to find $v(\zeta_0, \tau_0 + \delta\tau)$. By suitably combining the results of several such integrations one can, starting at $t = 0$, find the envelope functions at all later times. In order to have better explaination of the process, we refer to Fig. G.2, which shows the integration domain in the new coordinates ζ and τ. The front of the system corresponds to $\zeta - \tau = 0$, whereas the back corresponds to $\zeta - \tau = L$. As indicated in Fig. G.2 by the dotted lines, time is constant along the straight lines for which $\zeta + \tau = C$. Equations (G.5) show that u is integrated to the right in Fig. G.2, or toward the back of the system, while v is integrated upward, or toward the front. More details of the method can be found in [53]. Figure G.3 shows the resulting transmitted amplitude, for a calculation with $N = 28$, in which $\kappa = 5.0$, $\delta = 4.5$, $L = 1.0$, and $\gamma = 0.1$. In the rotating frame the incoming radiation has an amplitude $A(t) = A(0) = 2.0$. The driving force is not applied instantaneously, and it increases smoothly for $0 < t < 2$ from $A(0) = 0$ to $A(2) = A_0$, as described in [53]. $A(t) = A_0$ for $t \geq 2$. Figure G.3 shows that it takes more than a single time unit for the transmission signal to reach an appreciable value because it requires more than one time unit in order to travel the length of the structure. After a short transient regime, the system shown in Fig. G. 3 exhibits self-pulsing but with a decreasing amplitude. Such behavior for these systems is quite common and is discussed in more detail in [134].

163
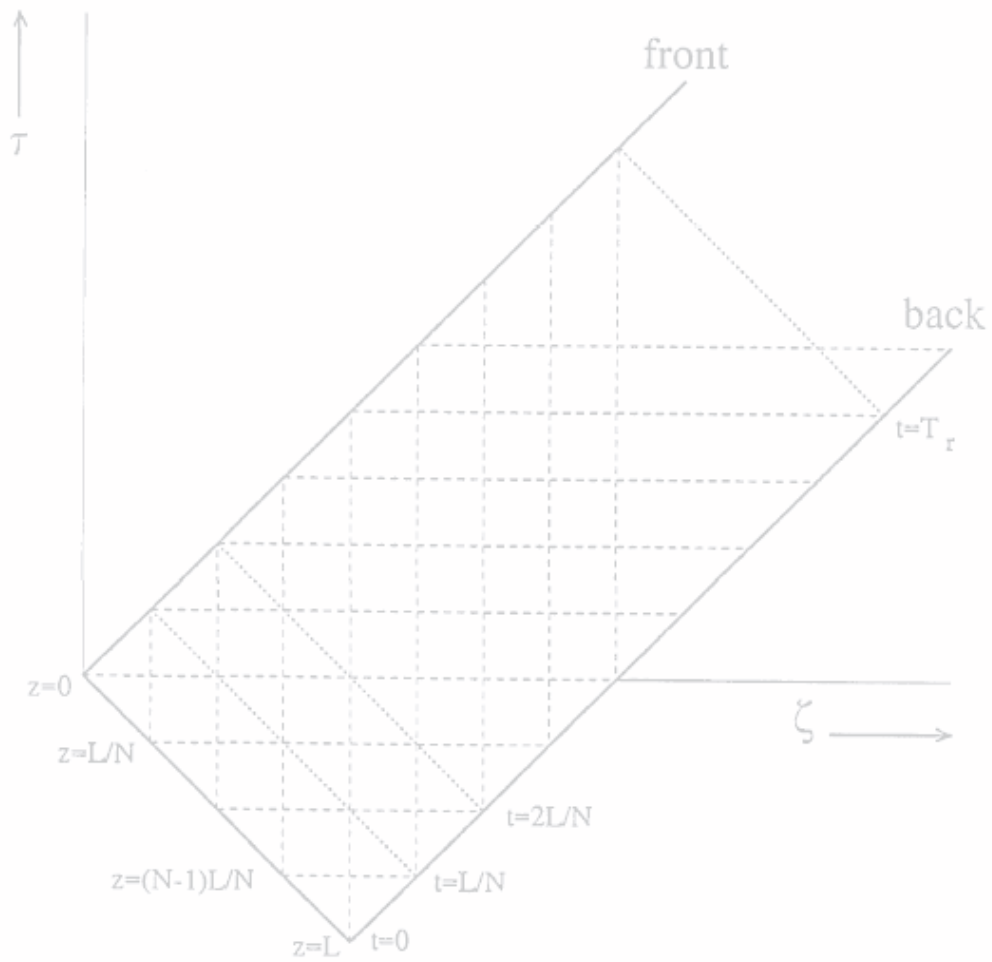
Figure G.2: Integration domain in the coordinates ζ and τ. The boundaries of this domain are given by thick solid lines. The dotted lines indicate points of equal time. In a finite-difference scheme the integration takes place along the dashed lines. The parameter T_r designates a single roundtrip time. (After Ref. [53], © 1991 OSA.)
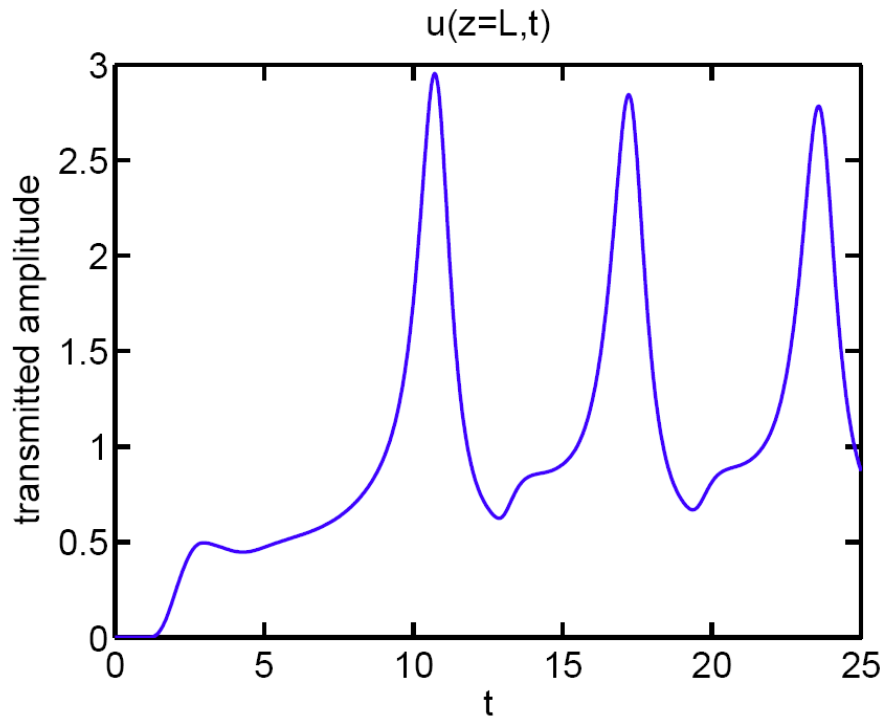
Figure G.3: Numerical results for a calculation in which our method is applied to Eqs. (G.1). Shown is the magnitude of the transmitted radiation $|u(L, t)|$ as a function of time. The parameters are $\kappa = 5.0$, $\delta = 4.5$, $\gamma = 0.1$, $L = 1.0$; in the rotating frame a constant incoming signal of $A(t) = A_0 = 2.0$. This driving signal is taken to increase smoothly from $A(0) = 0$ to $A(2) = A_0$ in order to avoid shocks. $A(t) = A_0$ for $t >= 2$.

Appendix H: Painlevé Analysis

We now apply the well established Painlevé analysis to Eq. (2.1) to derive the parametric condition on $\beta_2(z)$ for which the NLSE [Eq. (2.1)] is completely integrable [135]. To proceed further with the Painlevé analysis, we introduce a new set of variables $a(=E)$ and $b(=E^*)$. By Eq. (3.1), a and b can be written as

$$ia_z - \frac{\beta_2(z)}{2}a_{tt} + \gamma_g a^2 b = 0, \tag{H.1}$$

$$-ib_z - \frac{\beta_2(z)}{2}b_{tt} + \gamma_g b^2 a = 0. \tag{H.2}$$

Generalized Laurent series expansion of a and b are,

$$a = \sum_{r=0}^{\infty} a_r \varphi^{r+u}, \qquad b = \sum_{r=0}^{\infty} b_r \varphi^{r+\delta}, \tag{H.3}$$

with $a_0, b_0 \neq 0$, where u and δ are negative integers, a_r and b_r are set of expansion coefficients which are analytic in the neighborhood of the non-characteristic singular manifold $\varphi(z,t) = 0$. Looking at the leading order, $a \approx a_0 \varphi^u$ and $b \approx b_0 \varphi^\delta$ are substituted in Eq. (H.1) and upon balancing dominant terms, the results obtained are: $u = \delta = -1$ and $a_0 b_0 = \varphi_t^2 \beta(z)/\gamma_g$.

Substituting the full Laurent series (H.3) in Eq. (H.1) and considering the leading order terms the resonances are found to be, $r = -1, 0, 3, 4$. The resonance at $r = -1$ represents the arbitrariness of the singularity manifold and $r = 0$ corresponds to the fact that either a_0 or b_0 is arbitrary. Collecting and balancing the coefficients of the different powers of φ show that a sufficient number of arbitrary functions exists only for the following parametric condition on $\beta_2(z)$

$$\frac{d^2\beta_2(z)}{dz^2}\beta_2(z) - \left[\frac{d\beta_2(z)}{dz}\right]^2 = 0. \tag{H.4}$$

On solving this equation, we have

$$\beta_2(z) = \beta_{20}\exp(-\sigma z). \tag{H.5}$$

Constant dispersion is also another solution of Eq. (H.4) which is not our interesting case.

Appendix I: Bäcklund Transformation

The Lax pair associated with Eq. (2.21)

$$\frac{\partial E}{\partial T} = U_1 E \,,$$

$$E = (E_1 \quad E_2)^T$$

where

$$U_1 = \begin{pmatrix} -i\lambda & \mu q \\ \mu q^* & i\lambda \end{pmatrix} \tag{I.1}$$

where $\mu = \sqrt{-\gamma / \beta_{20}}$, $q = E \exp(-i\alpha_{20}T^2 / 2)$ and λ is the variable spectral parameter given by

$$\lambda = \sigma(z) + i\chi(z); \; \lambda_z = \alpha_{20}\beta_{20}\lambda / 2; \; \lambda_T = 0; \tag{I.2}$$

$$\lambda = \lambda_0 \left(\exp \alpha_{20}\beta_{20}z / 2 \right); \; \sigma(z) = \lambda_{0R} \exp\left(\alpha_{20}\beta_{20}z / 2\right); \; \chi(z) = \lambda_{0I} \exp\left(\alpha_{20}\beta_{20}z / 2\right). \tag{I.3}$$

Here $\lambda_{0R} = \mathrm{Re}(\lambda_0)$ and $\lambda_{0I} = \mathrm{Im}(\lambda_0)$, are respectively, the real and imaginary parts of the hidden isospectral parameter λ. Space evolution of eigenfunction E is given by

$$\frac{\partial E}{\partial z} = V_1 E$$

$$V_1 = \beta_{20} \left(\frac{1}{2}\alpha_{20}\lambda T - \lambda^2 + \frac{1}{2}\mu^2 |q|^2 \right) R_1 + \mu\beta_{20} \left(\frac{1}{2}\alpha_{20}T - \lambda \right) R_2 - \frac{i\mu\beta_{20}}{2} R_3,$$

with

168

$$R_1 = \begin{pmatrix} -i & 0 \\ 0 & i \end{pmatrix}, \quad R_2 = \begin{pmatrix} 0 & q \\ -q^* & 0 \end{pmatrix}, \quad R_3 = \begin{pmatrix} 0 & q_T \\ q_T^* & 0 \end{pmatrix}, \tag{I.4}$$

Equation (2.21) can be obtained from the compatibility condition

$$U_{1z} - V_{1T} + [U_1, V_1] = 0. \tag{I.5}$$

We derive the Bäcklund transformation from the time evolution equation of the eigenfunction. In order to construct the Bäcklund transformation, let us write down equation in terms of the Riccati equation. For this purpose, we introduce a new variable (or pseudopotential)

$$\Gamma = \frac{E_1}{E_2} \tag{I.6}$$

The above equation yields,

$$\Gamma_T = -2i\lambda\Gamma + \mu q + \mu q^* \Gamma^2 \tag{I.7}$$

Now transformation of variables $\Gamma \to \Gamma'$, $\lambda \to \lambda'$, $q \to q'$ which keep the form of the above equation invariant are sought. The simplest transformation can be tried by setting $\Gamma' = \Gamma$, $\lambda' = \lambda^*$ and looking for q' in the form

$$q - q' = \frac{2i(\lambda - \lambda^*)\Gamma}{\mu\left(1 + |\Gamma|^2\right)}. \tag{I.8}$$

The above equation defines the Bäcklund transformation of Eq. (2.21) with $q = E \exp(-i\alpha_{20}T^2 / 2)$. Here the primed quantities refer to N-soliton solution and the unprimed quantities refer to $(N-1)$ soliton solution.

Bibliography

[1] Takeshi Kamiya and Masahiro Tsuchiya, "Progress in Ultrafast Photonics,"*AAPPS Bulletin* **16**, 23 (2006).

[2] B. J. Eggleton, G. Lenz, and N. M. Litchinitser, "Optical pulse compression schemes that use Nonlinear Bragg Gratings," *Fiber and Integrated Optics* **19**, 383 (2000).

[3] Hans W. Mocker and R. J. Collins, "Mode competition and self-locking effects in a Q-switched Ruby laser," *Appl. Phys. Lett.* **7**, 270 (1965).

[4] A. J. DeMaria, D. A. Stetser, and H. Heynau, "Self mode-locking of lasers with saturable absorbers," *Appl. Phys. Lett.* **8**, 174 (1966).

[5] G. P. Agrawal, Nonlinear fiber optics, Academic Press (2001).

[6] G. P. Agrawal, Applications of Nonlinear Fiber Optics, Academic Press (2001).

[7] J. A. Giordmaine, M. A. Duguay, and J. W. Hansen, "Compression of optical pulses," *IEEE J. Quantum Electron.* **QE-4**, 252 (1968).

[8] E. B. Treacy, "Optical pulse compression with diffraction gratings," *IEEE J. Quantum Electron*. **5**, 454 (1969).

[9] R. A. Fisher, P. L. Kelley, and T. K. Gustafson, "Subpicosecond pulse generation using the optical Kerr effect," *Appl. Phys. Lett*. **14**, 140 (1969).

[10] W. J. Tomlinson, R. H. Stolen, and C. V. Shank, "Compression of optical pulses by self-phase modulation in fibers," *J. Opt. Soc. Am. B* **1**, 139 (1984).

[11] R. L. Fork, C. H. B. Cruz, P. C. Becker, and C. V. Shank, "Compression of optical pulses to six femtoseconds by using cubic phase compensation," *Opt. Lett.* **12**, 483 (1987).

[12] T. Nakashima, M. Nakazawa, K. Nishi, and H. Kubota, "Effect of stimulated Raman scattering on pulse-compression characteristics," *Opt. Lett.* **12**, 404 (1987).

[13] A. M. Weiner, J. P. Heritage, and R. H. Stolen, "Self-phase modulation and optical pulse compression influenced by stimulated Raman scattering in fibers," *J. Opt. Soc. Am. B* **5**, 364 (1988).

[14] S. L. Gomes, A. S. Gouveia-Neto, and J. R. Taylor, "Soliton Raman fibre-ring oscillators," *Opt. Quantum Electron.* **20**, 165 (1988).

[15] M. Kuckartz, R. Schulz, and H. Harde, "Operation of a fiber-grating compressor in the Raman regime," *J. Opt. Soc. Am. B* **5**, 1353 (1988).

[16] A. P. Vertikov, P. V. Mamyshev, and A. M .Prokhorov, " Increase of degree of fibre-grating pulse compression by parametric suppression of stimulated Raman scattering," *Sov. Lightwave Commun.* **1**, 363 (1991).

[17] L. F. Mollenauer, R. H. Stolen, and J. P. Gordon, "Experimental observation of picosecond pulse narrowing and solitons in optical fibers," *Phys. Rev. Lett.* **45**, 1095 (1980).

[18] R. H. Stolen, L. F. Mollenauer, and W. J. Tomlinson, "Observation of pulse restoration at the soliton period in optical fibers," *Opt. Lett.* **8**, 186 (1983).

[19] R. H. Stolen, J. Botineau, and A. Ashkin, "Intensity discrimination of optical pulses with birefringent fibers," *Opt. Lett.* **7**, 512 (1982).

[20] Laurent Chusseau and Eric Delevaque, "250-fs optical pulse generation by simultaneous soliton compression and shaping in a nonlinear optical loop mirror including a weak attenuation," *Opt. Lett.* **19**, 734 (1994).

[21] S. V. Chernikov and P. V. Mamyshev, "Femtosecond soliton propogation in fibers with slowly decreasing dispersion," *J. Opt. Soc. Am. B* **8**, 1633 (1991).

[22] P. V. Mamyshev, S. V. Chernikov, and E. M. Dianov, "Generation of fundamental soliton trains for high-bit-rate optical fiber communication lines," *IEEE J. Quantum Electron.* **27**, 2347 (1991).

[23] S. V. Chernikov, J. R. Taylor, and R. Kashyap, "Experimental demonstration of steplike dispersion profiling in optical fibre for soliton pulse generation and compression," *Electron. Lett.* **30**, 433 (1994).

[24] John D. Moores, "Nonlinear compression of chirped solitary waves with and without phase modulation," *Opt. Lett.* **21**, 555 (1996).

[25] M. E. Fermann, V. I. Kruglow, B. C. Thomsen, J. M. Dudley, and J. D. Harvey, "Self-similar propagation and amplification of parabolic pulses in optical fibers," *Phys. Rev. Lett.* **84**, 6010 (2000).

[26] V. I. Kruglov, A. C. Peacock, and J. D. Harvey, "Exact self-similar Solutions of generalized nonlinear Schrödinger equation with distributed coefficients," *Phys. Rev. Lett.* **90**, 113902 (2003).

[27] V. I. Kruglov, A. C. Peacock, and J. D. Harvey, "Exact solutions of the generalized nonlinear Schrödinger equation with distributed coefficients," *Phys. Rev. E* **71**, 056619 (2005).

[28] C. Billet, J. M. Dudley, N. Joly, and J. C. Knight, "Intermediate asymptotic evolution and photonic bandgap fiber compression of optical similaritons around 1550 nm," *Opt. Express* **13**, 3236 (2005).

[29] D. Anderson, M. Desaix, M. Karlsson, M. Lisak, and M. L. Quiroga-Teixeiro, "Wave-breaking-free pulses in nonlinear-optical fibers," *J. Opt. Soc. Am B* **10**, 1185 (1993).

[30] D. Méchin, S. H. Im, V. I. Kruglov, and J. D. Harvey, "Experimental demonstration of similariton pulse compression in a comblike dispersion-

decreasing fiber amplifier," *Opt. Lett.* **31**, 2106 (2006).

[31] D. Y. Smith, "Dispersion theory, sum rules and their application to the analysis of optical data," in Handbook of Optical Constants of Solids, (E. P. Palik, Ed.), Chapter 3. Academic Press, New York (1985).

[32] D. P. Hand and P. S. J. Russell, "Photoinduced refractive index changes in germanosilicate optical fibers," *Opt. Lett.* **15**, 102 (1990).

[33] J. L. Archambault, L. Reekie, and P. S. J. Russell, "High reflectivity and narrow bandwidth fibre gratings written by single excimer pulse," *Electron. Lett.* **29**, 28 (1993).

[34] J. L. Archambault, L. Reekie, and P. S. J. Russell, "100% reflectivity Bragg reflectors produced in optical fibres by single excimer laser pulses," *Electron. Lett.* **29**, 453 (1993).

[35] P. J. Lemaire, R. M. Atkins, V. Mizrahi, and W. A. Reed, "High pressure loading as a technique for achieving ultrahigh UV photosensitivity and thermal sensitivity in doped optical fibers," *Electron. Lett.* **29**, 1191 (1993).

[36] R. Kashyap, Fiber Bragg gratings, 1st ed. New York: Academic Press (1999).

[37] J. Lauzon, S. Thibault, J. Martin, and F. Ouellette, "Implementation and characterization of fiber Bragg gratings linearly chirped by temperature gradient," O*pt. Lett.* **19**, 2027 (1994).

[38] B. Malo, S. Theriault, D. C. Johnson, F. Bilodeau, J. Albert, and K. O. Hill "Apodized in-fiber Bragg grating reflectors photo-imprinted using a phase mask," *Electron. Lett.* **31**, 223 (1995).

[39] T. A. Strasser, P. J. Chandonnet, J. DeMarko, C. E. Soccolich, J. R. Pedrazzani, D. J. DiGiovanni, M. J. Andrejco, and D. S Shenk, "UV-induced fiber grating OADM devices for efficient bandwidth utilization,"

Proc. of Optical Fiber Communication Conference, **PD8**, 360 (1996).

[40] J. E. Sipe, B. J. Eggleton, and T. A. Strasser, "Dispersion characteristics of nonuniform Bragg gratings: Implications for WDM systems," *Opt. Commun.* **152**, 269 (1998).

[41] K. O. Hill, B. Malo, F. Bilodeau, D. C. Johnson, and J. Albert, "Bragg gratings fabricated in monomode photosensitive optical fiber by exposure through a phase mask," *Appl. Phys. Lett.* **62**, 1035 (1993).

[42] J. Martin and F. Ouellette, "Novel writing techniques of long in-fiber gratings," *Electron. Lett.* **30**, 811 (1993).

[43] L. Dong, M. J. Cole, A. D. Ellis, R. I. Laming, and T. Widdowson, "40 Gbit/s 1.55 μm RZ transmission over 109 km of non-dispersion shifted fiber with long continuously chirped fibre gratings," *Electron. Lett.* **33**, 1563 (1997).

[44] B. J. Eggleton, T. Stephens, P. A. Krug, G. Dhosi, Z. Brodzeli, and F. Ouellette, "Dispersion compensation using a fiber grating in transmission," *Electron. Lett.* **32**, 1610 (1996).

[45] B. J. Eggleton, R. E. Slusher, C. M. de Sterke, Peter A. Krug, and J. E. Sipe, "Bragg grating solitons," *Phys. Rev. Lett.* **76**,1627 (1996).

[46] B. J. Eggleton, C. M. d. Sterke, and R. E. Slusher, "Bragg solitons in the nonlinear Schröedinger limit: experiment and theory," *J. Opt. Soc. Am. B.* **16**, 587 (1999).

[47] P. A. Krug, T. Stephens, G. Dhosi, G. Yoffe, F. Ouellette, and P. Hill, "Dispersion compensation over 270 km at 10 Gbit/s using an offset-core chirped fiber Bragg grating," *Electron. Lett.* **31**, 1091 (1995).

[48] W. H. Loh, Ro. I. Laming, N. Robinson, A. Cavaciuti, F. Vaninetti, C. J.

Anderson, M. N. Zervas, and M. J. Cole, "Dispersion compensation over distances in excess of 500km for 10Gb/s systems using chirped fiber gratings," *IEEE Photonics Technol. Lett.* **8**, 944 (1996).

[49] P. S. J. Russell, "Bloch Wave Analysis of Dispersion and Pulse ropagation in Pure Distributed Feedback Structures," *J. Mod. Opt*. **38**, 1599 (1991).

[50] G. Lenz and B. J. Eggleton, "Adiabatic Bragg soliton compression in nonuniform grating structures," *J. Opt. Soc. Am. B* **15**, 2979 (1998).

[51] C. M. de Sterke and J. E. Sipe, "Gap solitons," *Prog. Opt*. **33**, 203 (1994).

[52] K. Senthilnathan and K. Porsezian, "Adiabatic Bragg soliton compression," *Opt. Commun.* **227**, 275 (2003).

[53] C. M. de Sterke, Kenneth R. Jackson, and B. D. Robert, "Nonlinear coupled-mode equations on a finite interval: a numerical procedure," *J. Opt. Soc. Am. B* **8**, 403 (1990).

[54] E. N. Tsoy and C. M. de Sterke, "Propagation of nonlinear pulses in chirped fiber gratings," *Phys. Rev. E* **62**, 2882 (2000).

[55] E. N. Tsoy and C. M. de Sterke, "Soliton dynamics in nonuniform fiber Bragg gratings," *J. Opt. Soc. Am. B* **18**, 1 (2001).

[56] Amir Rosenthal and Moshe Horowitz, "Analysis and design of nonlinear fiber Bragg gratings and their application for optical compression of reflected pulses," *Opt. Lett.* **31**, 1334 (2006).

[57] Amir Rosenthal and Moshe Horowitz, "Bragg-soliton formation and pulse compression in one-dimensional periodic structure," *Phys. Rev. E* **74**, 066611 (2006).

[58] G. I. Barenblatt, Scaling, Self-Similarity, and Intermediate Asymptotics, Cambridge University Press, Cambridge (1996).

[59] B. A. Malomed, "Variational methods in nonlinear fiber optics and related fields," *Prog. Opt.* **43,** 69 (2002).

[60] K. Nakkeeran and P. K. A. Wai, "Generalized projection operator method to derive the pulse parameters equations for the nonlinear Schrödinger equation," *Opt. Commun.* **244**, 377 (2005).

[61] P. Tchofo Dinda, A. B. Moubissi, and K. Nakkeeran, "Collective variable theory for optical solitons in fibers," *Phys. Rev. E* **64**, 016608 (2001).

[62] P. K. A. Wai and K. Nakkeeran, "On the uniqueness of Gaussian ansatz parameters equations: generalized projection operator method," *Phys. Lett. A* **332**, 239 (2004).

[63] M. J. Ablowitz and P. A. Clarkson, Solitons, Nonlinear Evolution Equations and Inverse Scattering, Cambridge University Press (1991).

[64] P. A. Clarkson, "Painlevé analysis of the damped, driven nonlinear Schrödinger equation," *Proc. Royal Soc. Edinburgh* **109A**, 109 (1988).

[65] S. Kumar and A. Hasegawa, "Quasi-soliton propagation in dispersion-managed optical fibers," *Opt. Lett.* **22**, 372 (1997).

[66] Y. Kodama, S. Kumar, and A. Maruta, "Chirped nonlinear pulse propagation in a dispersion-compensated system," *Opt. Lett.* **22**, 1689 (1997).

[67] M. L. Quiroga-Teixeiro, D. Anderson, P. A. Anderkson, A. Berntson, and M. Lisak, "Efficient soliton compression by fast adiabatic amplification," *J. Opt. Soc. Am. B* **13**, 687 (1996).

[68] K. Nakkeeran, **"**An exact soliton solution for an averaged dispersion-managed fibre system equation," *J. Phys. A: Mathematical and General* **34**, 5111 (2001).

[69] R. Ganapathy, V. C. Kuriakose, and K. Porsezian, "Soliton propagation in a birefringent optical fiber with loss and frequency chirping," *Opt. Commun.* **194**, 299 (2001).

[70] C. C. Mak, K. W. Chow, and K. Nakkeeran, "Soliton Pulse Propagation in Averaged Dispersion-managed Optical Fiber System," *J. Phys. Soc. Jpn.* **74**, 1449 (2005).

[71] V. N. Serkin and A. Hasegawa, "Exactly integrable nonlinear Schrödinger equation models with varying dispersion, nonlinearity and gain: Application for soliton dispersion managements," *IEEE J. Sel. Top. Quantum Electron.* **8**, 418 (2002).

[72] J. M. Dudley, C. Finot, D. J. Richardson, G, Millot, "Self Similarity in Ultrafast Nonlinear Optics," *Nature Physics* **3**, 597 (2007).

[73] A. Hasegawa, S. Kumar, and Y. Kodama, "Reduction of collision-induced time jitters in dispersion-managed soliton transmission systems," *Opt. Lett.* **21**, 39 (1996).

[74] Wen-hua Cao and P. K. A. Wai, "Picosecond soliton transmission by use of concatenated gain-distributed nonlinear amplifying fiber loop mirrors," *Appl. Optics* **44**, 7611(2005).

[75] D. Grischkowsky and A. C. Balant, "Optical pulse compression based on enhanced frequency chirping," *Appl. Phys. Lett.* **41**, 1 (1982).

[76] M. Litchinitser, B. J. Eggleton, and D. B. Patterson, "Fiber Bragg gratings for dispersion compensation in transmission: theoretical model and design criteria for nearly ideal pulse compression," *J. Lightwave Techno*l. **15**, 1303 (1997).

[77] G. Lenz, B. J. Eggleton and N. Litchinitser, "Pulse compression using fiber

grating as highly dispersive nonlinear elements," *J. Opt. Soc. Am. B* **15**, 715 (1998).

[78] M. Asobe, "Nonlinear optical properties of chalcogenide glass fibers and their application to all-optical switching," *Opt. Fiber Technol*. **3**, 142 (1997).

[79] A. Mysyrowicz, A. Couairon, and U. Keller, "Self-compression of optical laser pulses by filamentation," *New Journal of Physics* **10**, 025023 (2008).

[80] L. Bergé, S. Skupin, R. Nuter, J. Kasparian, and J. P. Wolf, "Ultrashort filaments of light in weakly ionized, optically transparent media,"*Rep. Prog. Phys.* **70**, 1633 (2007).

[81] M. Nurhuda, A. Suda, and K. Midorikawa, "Plasma-induced spectral broadening of high-energy ultrashort laser pulses in a helium-filled multiple-pass cell,"*J. Opt. Soc. Am. B* **23**, 1946 (2006).

[82] A. Couairon, "Dynamics of femtosecond filamentation from saturation of self-focusing laser pulses," *Phys. Rev. A* **68**, 015801 (2003).

[83] A. Braun G. Korn, X. Liu, D. Du, J. Squier, and G. Mourou, "Self-channeling of high-peak-power femtosecond laser pulses in air," *Opt. Lett.* **20**, 73 (1995).

[84] S. Tzortzakis, L. Sudrie, M. Franco, B. Prade, and A. Mysyrowicz, "Self-Guided Propagation of Ultrashort IR Laser Pulses in Fused Silica," *Phys. Rev. Lett.* **87**, 213902 (2001).

[85] A. Dubietis, G. Tamosauskas, I. Diomin, and A. Varanavicius, "Optical image encryption by random shifting in fractional Fourier domains," *Opt. Lett.* **28**, 269 (2003).

[86] Y. S. Kivshar and G. P. Agrawal, Optical Solitons: From fibers to photonic crystals, Academic Press, San Diego (2003).

[87] N. N. Akhmediev and A. Ankiewicz, Solitons: Nonlinear pulses and beams Chapman and Hall, London (1997).

[88] D. Mihalache, D. Mazilu, I. Towers, B. A. Malomed, and F. Lederer, "Stable spatiotemporal spinning solitons in a bimodal cubic-quintic medium," *Phys. Rev. E* **67**, 056608 (2003).

[89] I. Towers, A. V. Buryak, R. A. Sammut, B. A. Malomed, L.-C.Crasovan, and D. Mihalache, "Stability of spinning ring solitons of the cubic-quintic nonlinear Schrödinger equation," *Phys. Lett. A* **288**, 292 (2001).

[90] B. A. Malomed, L.-C. Crasovan, and D. Mihalache, "Stability of vortex solitons in the cubic-quintic model," *Physica D* **161**, 187 (2002).

[91] D. Mihalache, D. Mazilu, L.-C. Crasovan, I. Towers, A. V. Buryak, B. A. Malomed, L. Torner, J. P. Torres, and F. Lederer, "Stable Spinning Optical Solitons in Three Dimensions," *Phys. Rev. Lett.* **88**, 073902 (2002).

[92] J. Herrmann, "Bistable bright solitons in dispersive media with a linear and quadratic intensity-dependent refractive index change," *Opt. Commun.* **87**, 161 (1992).

[93] D. Pushkarov and S. Tanev, "Bright and dark solitary wave propagation and bistability in the anomalous dispersion region of optical waveguides with third- and fifth-order nonlinearities," *Opt. Commun.*, **124**, 354 (1996).

[94] R. Hao, L. Li, Z. Li, R. Yang, and G. Zhou, "A new way to exact quasi-soliton solutions and soliton interaction for the cubic-quintic nonlinear Schrödinger equation with variable coefficients," *Opt. Commun.* **245**, 383 (2005).

[95] F. Smektala, C. Quemard, V. Couderc, and A. Barthélémy, "Non-linear optical properties of chalcogenide glasses measured by Z-scan", *J. Non-*

Cryst. Solids **274**, 232, (2000).

[96] C. Zhan, D. Zhang, D.Zhu, D. Wang, Y. Li, D. Li, Z. Lu, L. Zhao, and Y. Nie, **"**Third- and fifth-order optical nonlinearities in a new stilbazolium derivative," *J. Opt. Soc. Am. B* **19**, 369, (2002).

[97] G. Boudebs, S. Cherukulappurath, H. Leblond, J. Troles, F. Smektala, and F. Sanchez, "Experimental and theoretical study of higher-order nonlinearities in chalcogenide glasses," *Opt. Commun.* **219**, 427, (2003).

[98] K. Ogusu, J. Yamasaki, S. Maeda, M.Kitao, and M. Minakata, "Linear and nonlinear optical properties of Ag-As-Se chalcogenide glasses for all-optical switching," *Opt. Lett.* **29**, 265, (2004).

[99] F. Sanchez, G. Boudebs, S. Cherukulappurath, H. Leblond, J. Troles, and F. Smektala, "Two- and three-photon nonlinear absorption in As_2Se_3 chalcogenide glass: theory and experiment," *J. Nonlinear Opt. Phys. Mater*. **13**, 7, (2004).

[100] B. Paredes, A. Videra, V. Murg, O. Mandel, S. Frlling, I. Cirac, G. V. Shlyapnikov, T. W. Wnsch, and I. Bloch, "Tonks–Girardeau gas of ultracold atoms in an optical lattice," *Nature* **249**, 277 (2004).

[101] S. L. Cornish, N. R. Claussen, J. L. Roberts, E. A. Cornell, and C. E. Wieman, "Stable 85Rb Bose-Einstein Condensates with Widely Tunable Interactions," *Phys. Rev. Lett*. **85**, 1795 (2000).

[102] Stoyan Tanew and Dimitar I. Pushkarov, "Solitary wave propagation and bistability in the normal dispersion regime of highly nonlinear optical fibers and waveguides," *Opt. Commun.* **141**, 322 (1997).

[103] S. Gatz and J. Herrmann, "Soliton propagation in materials with saturable nonlinearity," *J. Opt. Soc. Am. B* **8**, 2296 (1991).

[104] W. Krolikowski, X. Yang, B. Luther-Davies, and J. Breslin, **"**Dark soliton steering in a saturable nonlinear medium," *Opt. Commun*. **105,** 219 (1994).

[105] C. De Angelis, "Self-trapped propagation in the nonlinear cubic–quintic Schrödinger equation: a variational approach," *IEEE J. Quantum Electron*. **30,** 818 (1994).

[106] L. Berge, "Wave collapse in physics: principles and applications to light and plasma waves," *Phys. Rep.* **303**, 259 (1998).

[107] J. P. Gordon, "Dispersive perturbations of solitons of the nonlinear Schrödinger equation," *J. Opt. Soc. Am. B* **9**, 91 (1992).

[108] R. Y. Chiao, E. Garmire, and C. H. Townes, "Self-Trapping of Optical Beams," *Phys. Rev. Lett.* **13**, 479 (1964).

[109] A. W. Snyder and D. J. Mitchell, "Spatial solitons of the power-law nonlinearity," *Opt. Lett.* **18**, 101 (1993).

[110] Jian-Guo Ma, " An analytical solution of nonlinear waves propagating in power-law nonlinear dielectric waveguides," Microwave and Optical Technoly Letters **19**, 54 (1998).

[111] S. Gangopadhyay and S. N. Sarkar, "Variation analysis of spatial solitons of power-law nonlinearity," Fiber and Integrated Optics **20**, 191 (2001).

[112] Sergei K. Turitsyn, "Wave collapse and optical-pulse compression," *Phys. Rev. A* **47**, R27 (1993).

[113] C. Sulem and C. Sulem, The Nonlinear Schrödinger Equation: Self-Focusing and Wave Collapse, Springer, Berlin (2000).

[114] Yu. B. Gaididei, J. Schjodt-Eriksen, and P. L. Christiansen, "Collapse arresting in an inhomogeneous quintic nonlinear Schrödinger model," *Phys. Rev. E* **60**, 4877 (1999).

[115] G. L. Alfimov, V. V. Konotop, and P. Pacciani, "Stationary localized modes of the quintic nonlinear Schrödinger equation with a periodic potential," *Phys. Rev. A* **75**, 023624 (2007).

[116] V. E. Zakaharov and A. B. Shabat, "Exact theory of two-dimensional self-focusing and one-dimensional self-modulation of waves in nonlinear media," *Sov. Phys. JETP* **34**, 62 (1972).

[117] T. R. Taha and M. J. Ablowitz, "Analytical and Numerical Aspects of Certain Nonlinear Evolution Equations Part II: Numerical Nonlinear Schrödinger Equation," *J. Comput. Phys.* **55**, 203 (1984).

[118] A. Hasegawa and F. Tappert, "Transmission of stationary nonlinear optical pulses in dispersive dielectric fibers. I. Anomalous dispersion," *Appl. Phys. Lett.* **23,** 142 (1973).

[119] G. P. Agrawal and M. J. Potasek, "Nonlinear pulse distortion in single-mode optical fibers at the zero-dispersion wavelength," *Phys. Rev. A* **33**, 1765 (1986).

[120] P. K. A. Wai, C. R. Menyuk, Y. C. Lee, and H. H. Chen, "Nonlinear pulse propagation in the neighborhood of the zero-dispersion wavelength of monomode optical fibers," *Opt. Lett.* **11**, 464 (1986).

[121] G. P. Agrawal, "Optical pulse propagation in doped fiber amplifiers," *Phys. Rev. A* **44**, 7493 (1991).

[122] M. Margalit and M. Orenstein, "Simulation of passively mode lock lasers, using natural boundary conditions: multi pulse evolution and ordering," *Opt. Commun.* **124**, 475 (1996).

[123] J. R. Costa, C. R. Paiva, and A. M. Barbosa, "Modified split-step Fourier method for the numerical simulation of soliton amplification in erbium-

doped fibers with forward-propagating noise," *IEEE J. Quantum Electron.* **37**, 145 (2001).

[124] B. R. Washburn, S. E. Ralph, and R. S. Windeler, "Ultrashort pulse propagation in air-silica microstructure fiber," *Opt. Express* **10**, 575 (2002).

[125] J. M. Dudley and S. Coen, "Numerical simulations and coherence properties of supercontinuum generation in photonic crystal and tapered optical fibers," *IEEE J. Sel. Topics Quantum Electron.* **8**, 651 (2002).

[126] G. Genty, M. Lehtonen, H. Ludigsen, J. Broeng, and M. Kaivola, "Spectral broadening of femtosecond pulses into continuum radiation in microstrured fiber," *Opt. Express* **10**, 1083 (2002).

[127] T. Hori, N. Nishizawa, T. Goto, and M. Yoshida, "Experimental and numerical analysis of widely broadened supercontinuum generation in highly nonlinear dispersion-shifted fiber with a femtosecond pulse," *J. Opt. Soc. Am. B* **21**, 1969 (2004).

[128] O. V. Sinkin, R. Holzlöhner, J. Zweck, and C. R. Menyuk, "Optimization of the Split-Step Fourier Method in Modeling Optical-Fiber Communications Systems," *J. Lightwave Technol.* **21**, 61 (2003).

[129] J. Van Roey, J. van der Donk, and P. E. Lagasse, "Beam-propagation method: analysis and assessment," *J. Opt. Soc. Am.* **71**, 803 (1981).

[130] L. Thylen, "The Beam Propagation Method: An analysis of Its Applicability," *Opt. Quantum Electron.* **15**, 433 (1983).

[131] J. Saijonmaa and D. Yevick, "Beam-propagation analysis of loss in bent optical waveguides and fibers," *J. Opt. Soc. Am.* **73**, 1785 (1983).

[132] D. Yevick and B. Hermansson, "New fast Fourier transform and finite element approaches to the calculation of multiple-stripe-geometry laser

modes," *J. Appl. Phys.* **59**, 1769 (1986).

[133] G. H. Weiss and A. A. Maradudin, "The Baker-Hausdorff formula and a problem in crystal physics," *J. Math. Phys.* **3**, 771 (1962).

[134] C. M. de Sterke and J. E. Sipe, "Switching behavior of finite periodic nonlinear media," *Phys. Rev. A* **42**, 2558 (1990).

[135] E. N. Tsoy and C. M. de Sterke, "Propagation of nonlinear pulses in chirped fiber gratings," *Phys. Rev. E* **62**, 2882 (2000).